

Direct Entropy Measurements in Mesoscopic Systems:

From proof of concept to the Kondo regime

by

Timothy James Child

B.Sc., Imperial College London, 2014
PGCE, QTS, University College London, 2017

A THESIS SUBMITTED IN PARTIAL FULFILLMENT OF
THE REQUIREMENTS FOR THE DEGREE OF

DOCTOR OF PHILOSOPHY

in

THE FACULTY OF GRADUATE AND POSTDOCTORAL STUDIES

(Physics)

THE UNIVERSITY OF BRITISH COLUMBIA

(Vancouver)

March 2024

© Timothy James Child 2024

The following individuals certify that they have read, and recommend to the Faculty of Graduate and Postdoctoral Studies for acceptance, the thesis entitled:

Direct Entropy Measurements in Mesoscopic Systems: From proof of concept to the Kondo regime

submitted by **Timothy James Child** in partial fulfillment of the requirements for the degree of **Doctor of Philosophy in Physics**.

Examining Committee:

Joshua Folk, Professor, Physics and Astronomy, UBC

Supervisor

Andrew Potter, Assistant Professor, Physics and Astronomy, UBC

Supervisory Committee Member

Joerg Rottler, Professor, Physics and Astronomy, UBC

University Examiner

Ed Grant, Professor, Chemistry, UBC

University Examiner

David Goldhaber-Gordon, Professor, Physics, Stanford University

External Examiner

Additional Supervisory Committee Members:

Alannah Hallas, Assistant Professor, Physics and Astronomy, UBC

Supervisory Committee Member

Mark Halpern, Professor, Physics and Astronomy, UBC

Supervisory Committee Member

Abstract

Direct measurements of entropy in mesoscopic systems offer a promising pathway to explore a wide range of exotic quantum phenomena, especially those that prove challenging to investigate through conventional transport metrics. While entropy evaluations have traditionally depended on bulk properties like heat capacity – readily measurable in macroscopic systems – these approaches become ineffective at a mesoscopic scale where such properties are vanishingly small. For mesoscopic systems, a fundamentally different approach is required. This thesis introduces a novel entropy measurement protocol, founded on a Maxwell relation, that is universal for arbitrary mesoscopic circuits. It is developed, tested, and applied to systems of increasing complexity within two-dimensional electron gases (2DEGs) hosted in GaAs/AlGaAs heterostructures.

The central focus of the research is the development and validation of a universal entropy measurement protocol tailored for mesoscopic systems. This method is first demonstrated on a quantum dot weakly coupled to a thermal reservoir, affirming its effectiveness and showcasing the capability to continually assess entropy change throughout a charge transition – a marked advancement over the foundational approach that inspired this work. The protocol is next applied to a double quantum dot system, illustrating its aptitude to measure non-local entropy via capacitive coupling. The protocol’s universality is highlighted through measurements of a quantum dot hybridized with an electron reservoir, where density-matrix numerical renormalization group simulations align with experimental results up to intermediate coupling strengths. A notable divergence between theory and experiment emerges for stronger couplings, particularly where Kondo correlations are anticipated (in the mixed valence regime), raising intriguing

Abstract

ing questions yet to be answered. Lastly, preliminary measurements from a newly configured device that facilitates operation in the Kondo regime are discussed. The findings suggest spin suppression in the system, potentially marking the first observation of the entropic effect of a persistent Kondo-correlated singlet state.

This research establishes a fundamentally new technique with wide applicability, reaching beyond GaAs/AlGaAs 2DEGs to include other 2D mesoscopic systems such as layered graphene structures. As the field of quantum entropy measurement advances, this work sets a robust platform for future studies targeting a myriad of exotic quantum systems.

Lay Summary

In this thesis, a new way to measure entropy in very small, or “mesoscopic”, two-dimensional systems of electrons is introduced and tested. Traditional methods fall short in these tiny settings, so the work here offers a broadly applicable alternative. The new approach proves effective in different scenarios, revealing not only localized changes in entropy but also those that occur between coupled systems. The study focuses on systems formed in unique electronic structures called two-dimensional electron gases (2DEGs), and it uses quantum dots (akin to artificial atoms) among other nano-scale circuitry to probe their entropy. The method not only works for simple setups but also holds promise for exploring more complex systems that are expected to host enigmatic quantum phenomena. The technique could have wide applications, including in other materials like layered graphene. The work presented here sets the stage for future research into a wide range of exotic quantum states.

Preface

This thesis encapsulates the research I have undertaken during my doctoral studies in the Quantum Devices group, led by Joshua Folk, at the University of British Columbia. While I served as the primary researcher for the majority of the research presented herein, a precise breakdown of the collaborative contributions to the work follows.

Throughout the entire process, countless discussions with Joshua Folk, my supervisor, and Silvia Lüscher, a research associate, have contributed to all experiment concepts, device designs, and analysis interpretation.

The GaAs/AlGaAs heterostructures used for all presented measurements were provided to us by Mike Manfra's group at the University of Purdue. Specifically, Saeed Fallahi, Geoffrey Gardner, and Mike Manfra were involved in the fabrication of the heterostructures. The mesas and ohmic contacts were fabricated by Christian Olsen at the University of Copenhagen.

The fabrication of specific devices – defined by the gates deposited atop the heterostructures – was carried out by myself, both with and without assistance from others, in the cleanroom facilities of the Stewart Blusson Quantum Matter Institute at UBC. While I have fabricated and measured numerous devices throughout my time here – in many cases, a primarily solo effort – a large portion of the measurements presented in this thesis (Chapters 4, 5, 6) were obtained in one particularly fortunate round of fabrication and measurements that were carried out in collaboration with Owen Sheekey. Owen Sheekey was an undergraduate student at the time, and while I taught him many aspects of the design, fabrication, measurement, and analysis processes, he was a very capable student who contributed significantly in return.

Preface

Throughout the research presented here, many discussions with our theory collaborators – Yigal Meir, Eran Sela, and Andrew Mitchell – have contributed to our mutual understanding of the measurements and results presented. Discussions with Eran Sela, building on the prior work of Nik Hartman, inspired the theoretical framework of the measurement protocol presented here (primarily discussed in Section 3.1 and Chapter 4). Yigal Meir produced the theory calculations of the double quantum dot system entropy that we fit to data in Chapter 5. Yaakov Kleorin, under the supervision of Yigal Meir, produced the density-matrix numerical renormalization group (DM-NRG) simulations that we compare our measurements to in Chapter 6.

Chapter 4 describes the technical details of the entropy measurement protocol applied to a single weakly coupled quantum dot system. A version of this chapter has been published as [Child T, Sheekey O, Lüscher S, Fallahi S, Gardner GC, Manfra M, Folk J. A Robust Protocol for Entropy Measurement in Mesoscopic Circuits. *Entropy*. 2022;24(3):417]. I led the investigation from inception to publication. I was responsible for the majority of the device design, with fabrication carried out in collaboration with Owen Sheekey (the same device is used in Chapters 5 and 6). Measurement and analysis were carried out with the assistance of Owen Sheekey. Text preparation for the published work was carried out by myself, with review and editing assistance of Owen Sheekey, Silvia Lüscher, and Joshua Folk. Some modified text from this publication is also present in Chapter 8 (the conclusion).

Chapter 5 describes measurements of a double quantum dot system. The work presented is not published. However, the experiments described are part of ongoing work that will likely result in a future publication. I worked closely with Owen Sheekey throughout this experiment. Contributions to measurement and analysis were roughly equally split between me and Owen Sheekey for the work pertaining to this chapter (in comparison to Chapters 4 and 6, which I led). While this experiment formed the basis of Owen Sheekey’s undergraduate thesis work, the text presented in this thesis is entirely my own. One figure is an adaptation of Owen Sheekey’s, used

Preface

with permission.

Chapter 6 describes measurements of a quantum dot strongly coupled to a reservoir. A version of this chapter has been published as [Child T, Sheekey O, Lüscher S, Fallahi S, Gardner GC, Manfra M, et al. Entropy Measurement of a Strongly Coupled Quantum Dot. *Physical Review Letters*. 2022;129(22):227702]. I led the investigation from inception to publication. I was responsible for the majority of measurement and analysis, with assistance from Owen Sheekey. As previously mentioned, Yaakov Kleedorin produced the DM-NRG simulations. Text preparation for the published work was carried out by myself, with review and editing assistance of Owen Sheekey, Silvia Lüscher, and Joshua Folk.

Chapter 7 describes measurements of a small quantum dot directly tunnel coupled to a big quantum dot. I was the primary researcher for these measurements. The device was designed and fabricated in collaboration with Johann Drayne, a fellow graduate student. While the measurements presented here were solely obtained by myself, it is worth noting that they were taken at the end of an experiment (that had a different focus, not discussed in the thesis) that Johann Drayne contributed to significantly.

Table of Contents

Abstract	iii
Lay Summary	v
Preface	vi
Table of Contents	ix
List of Tables	xii
List of Figures	xiii
Acknowledgements	xxvii
Dedication	xxix
1 Introduction	1
1.1 Context	1
1.2 Motivation	2
1.3 Outline	4
2 Mesoscopic Devices	6
2.1 2DEG Heterostructures	6
2.2 Quantum Point Contacts (QPCs)	9
2.3 Quantum Dots	11
2.4 Charge Sensors	14
2.5 Determining Electron Temperature	15
2.6 Additional Measurement Procedures	17

Table of Contents

2.7 Summary 19

3 Background 22

3.1 Entropy 22

3.1.1 Entropy in mesoscopics 23

3.1.2 Conventional entropy measurement applied to meso-
scopics 25

3.1.3 Few-electron entropy-related measurements 28

3.1.4 Theoretical background of novel measurement tech-
nique 31

3.2 Kondo Effect 33

3.2.1 Overview of the Kondo effect 34

3.2.2 Kondo effect in mesoscopics 36

3.3 Numerical Renormalization Group (NRG) Calculations 42

4 Proof of concept measurement (Single Isolated QD) 45

4.1 Introduction 45

4.2 Device Design and Layout 46

4.3 Measurement Protocol 50

4.4 Common Problems 58

4.5 Conclusion 60

5 Non-local entropy measurements in a double QD system 61

5.1 Introduction 61

5.2 Device Design 66

5.3 Methods 69

5.4 Results 72

5.5 Discussion 77

5.6 Conclusion 81

6 Entropy measurements in the mixed valence regime 83

6.1 Introduction 83

6.2 Methods 84

6.3 Analysis 88

Table of Contents

6.4	Results	92
6.5	Discussion	95
7	Preliminary entropy measurements in the Kondo regime	97
7.1	Introduction	97
7.2	Device Design	98
7.3	Methods	101
7.4	Results	106
7.5	Discussion	109
8	Conclusion	112
8.1	Summary	112
8.2	Extensions of discussed measurements	113
8.3	Looking Forward	115
 Appendix		
A	NRG data and fitting	144
B	Measurement setup	177

List of Tables

- 3.1 A few examples of the probability of QD state and corresponding QD entropy for $0 \leq \langle N \rangle \leq 1$. $|0\rangle$ represents the unoccupied state while $|\uparrow\rangle$ and $|\downarrow\rangle$ represent the QD occupied with a spin up or down electron respectively. Entropy is calculated using the Gibbs formula (Eq. 3.2) with exact values shown where non-zero probabilities are equal (i.e. Eq. 3.1 applies). 23

- 5.1 Summary of the Initial and Final states of the double dot system corresponding to Figs. 5.6**b-i**, including the total entropy change of the system for each case. 72

List of Figures

- 1.1 Images depicting the scale of mesoscopic measurements. (a) A photograph of a device on a Si wafer sample holder, mounted on the “cold-finger” of the cryostat. The cold-finger is 25.7 mm in diameter. (b) A photograph taken through a wire-bonder microscope of the top-right corner of the GaAs/AlGaAs heterostructure with a device (middle) wire-bonded to the gold contacts of the Si wafer sample holder. The full heterostructure chip (not fully in the image) measures 5×5 mm. (c) A microscope image of a single device, where it is mostly the outer gates and bond pads that are visible. The device bond pads form a 1×1 mm square around a 2DEG mesa in which the mesoscopic circuit is formed. (d) A scanning electron micrograph (SEM) of the full device including the relatively large ($10 \times 10 \mu\text{m}$) heating reservoirs. The bright features are the metal gates deposited atop the dark heterostructure surface. (e) An SEM image focused on the smallest features of the device. A 200×200 nm quantum dot that would typically contain < 5 electrons is indicated. 3
- 2.1 (a) Three-dimensional schematic of a heterostructure (not to scale) showing the location of the 2DEG in blue along with the electron mobility μ_e and density n of the 2DEGs used in this thesis. (b) Layer compositions and thicknesses of the heterostructures. (c) Conduction band diagram indicating the location of uniform doping (orange circles) and δ -doping along with the triangular well that hosts the 2DEG. 7

List of Figures

- 2.2 (a) A top-down schematic of a quantum point contact formed in the 2DEG (blue) between two gates (gold) with negative potential applied. The white region around the gates indicates the depletion of the 2DEG in proximity (and under) the gates. Crossed squares represent ohmic contacts through which the conductance of the QPC (dashed line) can be measured using an external voltage source and current amplifier. (b) A typical measurement of the quantized conductance plateaus of a quantum point contact at low temperature, including “pinch off” at -830 mV. The gate voltage is applied to both gates. 10
- 2.3 (a) A schematic of a quantum dot (dashed red circle) formed in the 2DEG (blue) between 4 gates (gold). Crossed squares indicate Ohmic contacts through which the conductance of the QD can be measured by applying an external bias and measuring the resulting current. (b and c) Coulomb blockade energy diagrams of a QD with coupling strength Γ_L and Γ_R to the 2DEG leads. The chemical potential of the leads is μ_S and μ_D where $eV_{SD} = \mu_S - \mu_D$. The lines marked with crosses indicate the occupied energy levels in the QD, where the spacing between them is the charging energy E_C of the QD. In panel b the QD is insulating as the chemical potentials of the leads fall between energy levels of the QD preventing any first-order tunnelling processes. In panel c the QD is conducting due to the energy level of the QD falling between μ_S and μ_D such that first-order tunnelling processes can occur. (d) The conductance through a QD as plunger gate (top middle gate in panel a) voltages is swept. 12

List of Figures

2.4 (a) A schematic of a charge sensor QPC in close proximity to a QD. The vertical gate in the middle forms both, the charge sensor QPC in conjunction with the left gate, and the QD with the remaining gates on the right. The QD has only one lead through which electrons can enter or leave (dashed arrow). (b) Current through the charge sensor QPC with fixed bias as the plunger gate of the QD is swept over a wide range such that the QD is unoccupied at the left, and contains 4 electrons at the far right. Each sawtooth step indicates a change in the occupation of the QD. (c) A much narrower and higher resolution scan showing the change in plunger gate voltage from the first sawtooth in panel **b** at -138 mV showing the thermally broadened Fermi distributed charge transition of the QD at 100 mK. The vertical arrow represents the sensitivity of the charge sensor to the addition of one electron to the QD. 14

2.5 (a) Fits of Eq. 2.1 to charge sensor current measurements of the addition of an electron to a QD in a weakly coupled regime at $T = 100$ and 200 mK. Each dataset represents the average of many repeated measurements, and are offset from each other for clarity. Note that the x-axis represents fine-tuned gate potentials applied in addition to a coarse potential that is not shown. (b) The extracted Θ parameters from fits to charge transition measurements over a range of cryostat temperatures from 8 mK to 300 mK. A linear fit of the Θ s for $T > 85$ mK is shown, extrapolated back to $T = 0$ 16

List of Figures

2.6 Three-dimensional schematic (not to scale) of a device with a charge sensor, two quantum dots, and an “accumulation gate” in one of the QDs. Where most gates typically have negative enough potential to deplete the 2DEG underneath them (white regions), the accumulation gate is typically held close to 0 V and so is largely invisible to the 2DEG (black outline depicts where the 2DEG *would* deplete with a negative bias applied). 20

3.1 Schematic of a 2nd order tunnelling process illustrating a spin flip of the unpaired electron in the QD. Each panel depicts a QD coupled to two leads where the E_C separated energy levels of the QD straddle the Fermi energy of the leads. Crosses represent that all lower energy levels of the QD are filled with no net spin, leaving a single energy level below the Fermi energy that can be filled by a single spin up or down electron. (a) Initially, the QD has a net spin-up. (b) An intermediate state in which a spin-down electron has tunnelled into the QD from the left lead. Within a short time, a spin-up electron on the QD tunnels to the right lead. (c) The final state of the system after a single 2nd order tunnelling process where the QD now has a net spin-down. 37

3.2 (a) A schematic of a QD with an “accumulation” sweep gate in grey to distinguish it from the regular gates in gold. Crossed boxes represent ohmic contacts. (b) Conductance through the QD vs. sweep gate voltage measured with close to zero bias (1 uV) for electron temperatures ranging 30 to 300 mK. QD occupation for each Coulomb valley is indicated. Notably, conductance increases with decreasing temperature for the Coulomb valley where $N = 3$ due to the Kondo effect while the conductance where $N = 2$ falls with decreasing temperature as expected in the Coulomb valley. 39

List of Figures

4.1	(main panel) False-coloured scanning electron micrograph (SEM) of the key parts of the entropy sensor. Electrostatic gates (gold) define the circuit in a 2D electron gas (2DEG). The thermal electron reservoir (red) can be rapidly heated by driving current through quantum point contacts (QPCs) far away. (inset) Current through the charge sensor, I_{CS} , for a wide sweep of the coarse plunger gate, V_P , demonstrating the alignment of the $0 \rightarrow 1$ transition at the steepest part of the trace to maximize sensitivity.	48
4.2	(a) SEM micrograph of the full measurement device showing the large (10 μm square) chambers used for electron thermalization, QPCs 1 and 2 through which Joule heating current I_H flowed, and QPCs 3 and 4 through which heat diffused but no net current flowed. The dashed rectangle in the upper left is the region shown in Fig. 4.1a, including QD and charge sensor. (b) Crosses: broadening of the charge transition (Θ , left axis), converted to electron temperature (T_e , right axis), increases above the sample temperature, $T_s = 100$ mK, due to I_H driven through QPCs 1 and 2. Solid line: quadratic fit to $ I_H < 1$ nA data, with deviations seen at higher $ I_H $. (c) Extension of panel b to higher I_H and for a range of different sample temperatures. Sub-linear behaviour at very large I_H reflects electron-phonon cooling at higher temperatures.	52
4.3	Electron temperature vs I_H , with an extended I_H range compared to Fig. 4.2b, to emphasise the non-quadratic response for larger $ I_H $. The solid line represents the same quadratic fit ($I_H < 1$ nA).	53

List of Figures

- 4.4 A step-by-step inspection of the analysis procedure that goes into an eventual calculation of ΔS . The fine-tuning plunger gate, V_D , is used to lower the energy of the QD level such that one electron enters from the thermal reservoir. (top) Schematic illustration of $I_H(t)$ through one complete 80 ms cycle. (a–d) Charge sensor current through the 80 ms cycle, calculated with respect to the unheated sections, at four locations on the $0 \rightarrow 1$ transition: $V_D = -0.5, -0.1, 0.1, 0.5$ mV. Data shown here are averaged over 1200 square wave cycles. Blue (red) indicates times at which the thermal reservoir is unheated (heated). The relaxation time of the measurement (~ 3 ms) is visible in panels **b** and **c**. (e) Charge sensor current separated into averages over the 4 parts of the square heating wave, where heating is applied with an alternating current direction ($I_H = 3, -3$ nA), with zero bias applied in between ($I_H = 0$). Fits to the average “cold” and “hot” data are shown in grey. (f) The difference in charge sensor current between the “cold” and “hot” traces. (g) $\Delta S(V_D)$ obtained by integration of ΔI_{CS} using Eq. 4.1. ΔT is 28.1 mK, equivalent to 0.011 mV when converted to effective gate voltage, determined from the difference in thermal broadening of heated and unheated I_{CS} 56

List of Figures

- 4.5 (a) False-colour scanning electron micrograph similar to the entropy measuring circuit from Ref. [8] where the thermal electron reservoir was heated by I_H through a single QPC (top), with no additional confinement of the heated channel. (b) Using the circuit in panel a, ΔI_{CS} measurements over the $0 \rightarrow 1$ transition for 0, 100 and 200 mT of magnetic field applied perpendicular to the plane of the 2DEG. Then, 100 and 200 mT data are offset by 0.05 and 0.1 nA respectively. Illustrates the effect of unthermalized electrons from the heater QPC reaching the QD, for 0 and 100 mT data. Fits to theory for weakly coupled transitions (solid grey) emphasize the deviation of data from theory on the $N = 0$ side of the transition. (c) Four segments of I_H square wave averaged separately, analogous to Fig. 4.4e and made using the circuit in Fig. 4.2a, but without proper balancing to keep the chemical potential of the reservoir at ground. The result is a shift of $I_H = +5$ nA with respect to -5 nA data. Inset: zoom-in to the $V_D = -0.4 \rightarrow -0.1$ mV range of the main panel, showing both lateral and vertical offsets ± 5 nA data. 59
- 5.1 Measured entropy change ΔS from the addition of the first electron to a weakly coupled QD where an additional contribution varies as a function of the potential applied to one of the nearby gates. The dotted line marks $k_B \ln(2)$, the expected entropy change in the absence of additional contributions. Each value of ΔS corresponds to entropy change extracted from a 1D measurement over the $N = 0 \rightarrow 1$ charge transition of the QD. 62
- 5.2 Fictitious example of an impurity's effect on measured entropy change of a QD. (a) The absolute entropy of the impurity that depends on the QD occupation. (b) The total entropy change that would be measured for the addition of the first electron to the QD for a range of V_G values. 64

List of Figures

- 5.3 False-coloured scanning electron micrographs (SEMs) of the device, with **(a)** showing the heater reservoirs, and **(b)** showing where the two QDs form. The green region represents the charge sensor. Red represents the thermal electron reservoir that is heated and cooled rapidly during entropy measurement. Blue represents an area of 2DEG that remains cold and must be decoupled from QD2 in order to ensure QD2 remains in thermal equilibrium with the thermal reservoir. Note that the gate labelled V_{D1} is varied only close to 0 V, and as a result, is largely transparent to the 2DEG (in comparison to the other gates that typically form opaque barriers in the 2DEG). The two greyed-out gates in the blue region are unused and kept grounded. For more detail of connected circuitry, see Figs. 4.1 and 4.2 that depict the same device. . 67

List of Figures

- 5.4 Charge stability plots of the double dot system. All panels show charge sensor current differentiated in the y -direction in order to emphasise the charge transitions of both QDs (QD2 transitions – the more horizontal lines – are hard to see otherwise). In all panels, lines represent where the occupation of QD1 increases from left to right, and QD2 from bottom to top. **(a)** Various charge states of the two QDs (N_{QD1}, N_{QD2}) over a relatively wide range of gate space. The rectangle at $(-550, 110)$ depicts the region measured in the lower panels. **(b and c)** Fine scans over the region indicated in panel **a** where the applied gate voltages represent fine-tuned control in addition to fixed gate voltages chosen near the inter-dot charge degeneracy point. Panel **c** is measured with a virtual x -axis gate that holds the QD2 occupation constant (hence, the horizontal QD2 transition lines). The diagonal line between triple points (blue colour) is where the two QDs are charge degenerate. Note that the blue line does not represent an inherently different effect of the charge transition on the charge sensor current; it is merely a consequence of the differentiation axis, which conveniently serves to highlight the region of interest. 71
- 5.5 Charge stability diagram with possible double dot states overlaid at key positions. $|\uparrow, \downarrow\rangle$ represents a state in which QD1 is occupied with a spin-up electron, and QD2 is occupied with a spin-down electron, for example. The data is the same as that of Fig. 5.4**c**. 73

List of Figures

5.6 (a) Charge sensor signal, $\Delta I_{CS} \propto dN/dT$, as a function of a virtual gate controlling the QD1 energy, and a plunger gate that primarily affects the QD2 energy, where both represent fine-tune additions to coarse gate values set close to inter-dot charge degeneracy. Occupations of the two QDs are displayed for various regions of the graph with notation (N_{QD1}, N_{QD2}) . For simplicity, a virtual gate is not used for QD2, hence the slope in the QD1 transition at the top and bottom of panel **a**. (b–e) Line cuts from **a** taken at $V_{P2} = 0.8, -0.5, -2$ and -3 mV respectively, that when integrated result in the entropy changes ΔS shown in panels (f–i). (j) The total entropy change of the system calculated from the measurement shown in panel **a**. All but panel **j** have x-axes that correspond to the energy of QD1, where the occupation increases from left to right at the near vertical feature in panel **a**, similar to that of Fig. 5.4). Similarly the y-axis of panels **a** and **j** primarily correspond to the energy of QD2, where occupation increases from bottom to top at the faint horizontal features in panel **a**. Table 5.1 summarizes the expected mixed states and entropy changes of the system at the key points depicted in panels **b–i**. 74

5.7 (a) Charge stability diagram of the double dot system in a regime where both dots are very weakly coupled to the reservoir. The apparently noisy region in the middle indicates that we are detecting discrete charge transitions between the QDs (rather than a time average). (b) charge sensor current of a much slower 1D scan at $V_{P2} = 0$ mV that includes 100s of discrete charge jumps back and forth between the two QDs. (c and d) Close-up of the data shown in panel **b** where V_{D1} is effectively static over the range of measurement shown, hence, a time-axis is displayed. 78

List of Figures

- 5.8 Schematics of the double dot system depicting charge transfer between the two QDs. QD1 and QD2 are coupled to the reservoir (that has chemical potential μ) with coupling strengths Γ_{QD1} and Γ_{QD2} respectively. **(a and b)** Schematics with QD1 or QD2 occupied, respectively, where the occupation of either QD shifts the energy levels of the other QD to higher energy as a result of the inter-dot Coulomb interaction U . **(c)** The intermediate step that facilitates the transfer of an electron from one QD to the other. 80
- 6.1 **(a)** Scanning electron micrograph of the device. Electrostatic gates (gold) define the circuit. Squares represent ohmic contacts to the 2DEG. The thermal electron reservoir (red) was alternated between base and elevated temperatures. **(b)** Current through the charge sensor, I_{CS} , for the $0 \rightarrow 1$ charge transition in a weakly coupled regime, separated into the unheated (100mK) and heated (130mK) parts of the interlaced measurement [146], showing the single electron step height I_e . **(c and d)** Change in I_{CS} from 100 to 130 mK, for weak (panel **c**) and strong (panel **d**) coupling between QD and reservoir. Panel **c** includes a fit to weakly-coupled theory. 85
- 6.2 Change of S in the QD across the $N = 0 \rightarrow 1$ transition, obtained by integrating $\Delta I_{CS}(V_D)$ (Fig. 6.1c) following Eq. 3.12. Dot occupation across the transition is shown in grey. Data obtained in the weakly coupled limit, $V_T = -350$ mV corresponding to $\Gamma/k_B T \sim 1 \times 10^{-4}$. $\Delta S_{0 \rightarrow 1} = (0.99 \pm 0.02)k_B \ln(2)$ is the net change ΔS across the complete transition. Inset: comparison of ΔS_{fit} , $\Delta S_{0 \rightarrow 1}$, and ΔS_{max} (see text) for V_T covering approximately $10^{-5} < \Gamma/k_B T < 10^{-1}$ 87

List of Figures

6.3	<p>(a) Markers illustrate a single measurement across the charge transition, which takes 30 seconds to complete. No peak in ΔI_{CS} can be seen in this raw data. After averaging 400 of such scans together (solid line), however, a small peak in ΔI_{CS} is seen at $\Delta V_D = 0$. (b) Raw ΔI_{CS} data (greyscale) for 400 scans as in panel a. Averaged together, they yield the solid line in panel a.</p>	89
6.4	<p>Variation of lever arm α, and charge step I_e measured independently over the full range of V_T explored in this experiment. Dashed line: extrapolation of α into the strongly-coupled regime where it cannot be measured directly</p>	92
6.5	<p>Evolution of $S(\epsilon)$ from the weak (black) to strong (red) coupling regimes, comparing data (a) to NRG calculations (c). Measurements of occupation across the charge transition are fit to NRG (b), leaving no free fit parameters for the $S(\epsilon_0)$ calculation. Panel b inset: Coupling strength of the QD to the reservoir, $\Gamma/k_B T$, extracted from fits, across the full range of V_T. Values $\Gamma/k_B T \ll 1$ cannot be measured directly and are extrapolated (dashed line).</p>	93
6.6	<p>The lineshape of ΔI_{CS}, here plotted vs occupation instead of V_D, shows no dependence on V_{CS} within experimental noise, though of course the magnitude of I_{CS} and ΔI_{CS} scales linearly with V_{CS}. The case of $\Gamma/k_B T = 24$ is shown here. In particular, ΔI_{CS} remains peaked at $N \sim 0.5$, in contrast to the NRG calculation (solid line) in which the shifted peak reflects the screening of spin entropy in the mixed valence regime due to the formation of the Kondo singlet</p>	96

List of Figures

7.1	Scanning electron micrographs (SEMs) of the measured device. (a) The full device with the typical two-chamber heating reservoirs discussed in Chapter 4. (b) Two SD–BD devices that are close to identical in design. Measurements discussed in this chapter were taken using the right side QDs, also shown in panel d . (c) A close-up of the small dot only. Gates around the QDs are labelled, where V_C primarily controls the SD–BD coupling, V_{SDP} is the SD plunger, V_{CSS} and V_{CSQ} form the charge sensor QPC, V_N controls both SD–reservoir and SD–BD coupling, V_{BD} forms the big dot, and V_{BDP} acts as the BD plunger.	99
7.2	Charge stability diagrams with varying SD–BD coupling. The data represents charge sensor current differentiated in the horizontal axis. SD charge transitions occur at the more vertical features, and BD transitions at the faint more horizontal features. Occupations of the two QDs are shown as (N_{SD}, N_{BD}) . While the precise occupation of the SD is known, for the BD, only its relative occupation is known. (a) Weak coupling. (b) and (c) Increasingly strong coupling. Note that the SD–BD charge transitions broaden with increased coupling, while the SD–reservoir and BD–reservoir transitions remain thermally broadened due to the SD–reservoir coupling remaining weak.	102
7.3	Differential charge sensor current charge stability plots with varying SD–BD coupling using the virtual SDP' gate for the x-axis, where the primary V_{SDP} values are shown in the axes. (a) Weak coupling data, taken without using a virtual gate, as a reference for the effect of virtual gating in all other panels. (b) Weak coupling (same as a except for the virtual gate). (c) and d) Medium and strong coupling, respectively.	105

List of Figures

7.4 Summary of entropy measurements with weak (left) and strong (right) SD–BD coupling. (**a** and **b**) Peak and final entropy changes (in arbitrary units) over the SD transition, corresponding to vertical sweeps in the charge stability diagram below. Note that the axes of the charge stability diagrams are swapped in comparison to previous figures. (**c** and **d**) Full entropy measurements as a function of SD energy averaged over the regions indicated by vertical dashed lines in panel **a** and **b**. Arbitrary units are used for entropy change due to the lack of sufficient calibration measurements. The dashed lines in all but **d** indicate $\frac{\ln(2)}{\ln(3)} \cdot \Delta S_{\text{peak}}$. For **d**, the dashed line is the same as that in panel **c** (i.e. assuming the calibration factors are the same and the arbitrary values are comparable, however, this may not be the case). 107

B.1 Photo of the BF-XLD system showing the lower temperature plates and coldfinger. The gold plated copper plate that is in line with the bottom of the top outer vacuum can (OVC) is the 4 K plate. Below that, there is the Still plate, 0.1 K (not usually referenced), and finally, the mixing chamber (MC) plate. The 50 K plate is hidden from view by the top OVC. The coldfinger is the copper piece extending below the MC plate, designed such that a mounted sample is positioned in the center of the magnet (not shown) when the system is in operation. 180

Acknowledgements

I am grateful to numerous individuals whose collective contributions have not only shaped my academic achievements during my PhD journey but also enriched my overall experience. I would like to extend my thanks to:

- Dr. Joshua Folk for excellent supervision throughout my PhD, being available at a moment's notice for countless insightful meetings, facilitating an environment of learning and exploration, and allowing me to remain blissfully unaware of all the administrative efforts that are required to fund and run cutting edge scientific experiments.
- Dr. Silvia Lüscher for teaching me a wealth of information about nanofabrication, assisting with many experiments and analyses, and taking care of a whole manner of lab-related tasks throughout my time here.
- Dr. Nik Hartman, the post-doc with whom my time was unfortunately brief but impactful. He got me started on my research and exemplified a team spirit that I have strived to continue.
- Christian Olsen, the senior PhD student who served as the group's tech guru for the majority of my tenure. His behind-the-scenes efforts were easily overlooked, but having inherited this role in my final years, I now have a deeper appreciation for the work that entailed.
- Our theory collaborators from disparate parts of the world, Dr. Yigal Meir, Dr. Eran Sela, and Dr. Andrew Mitchell, for their patience and skill in bridging the language gap between theoretical and experimental perspectives during our many early morning/late night video calls.

Acknowledgements

- Dr. Yaakov Kleeorin, whose NRG calculations were indispensable to my research. Although our interactions were limited, I spent hundreds of hours working with these calculations, attesting to their crucial role in my work.
- Owen Sheekey, a welcome addition to the entropy team during the year we collaborated. His companionship made long fabrication and measurement days more enjoyable, and provided a much-appreciated opportunity for idea exchange after several years of relatively solo work.
- Johann Drayne, another very welcome addition to the entropy team for my final year and a half here. We worked hard, we had lots of things go wrong, but his zest for life made the whole process a positive one. Concluding my PhD in such a collaborative way has imbued my overall experience with a more positive hue.
- Klauss Ensslin and Thomas Ihn's group at ETH Zurich, as well as Frederic Pierre's group at Université Paris-Saclay, for hosting outstanding Quantropy conferences over the past two years. The sense of camaraderie among all participants has been truly invigorating. I thoroughly enjoyed spending time with everyone there, and wish them all the best in their future endeavours.

Finally, I would like to thank my parents, whom I have seen and spoken to far too little since being buried in PhD work over the last half a decade, but who have supported me nonetheless. I am looking forward to a renewed family connection going forward.

Dedication

To Alexandra Tully: the girlfriend I was excited to move halfway across the world with to come here to UBC, the fiancée who made the whole PhD experience an enjoyable one, and my wife with whom I am eager to begin the next chapter of life.

Chapter 1

Introduction

1.1 Context

Entropy has been an integral part of scientific inquiry for over a century, with its applications spanning numerous disciplines such as chemistry, cosmology, information theory, materials science, and more. The concept was first introduced by Rudolf Clausius in the mid-19th century as a means to understand the behaviour of energy in thermodynamic systems [1]. Since then, entropy has permeated into diverse areas of science, proving itself as a versatile and useful tool. In chemistry, the concept of entropy is crucial for understanding the spontaneous direction of chemical reactions, as governed by the second law of thermodynamics [2]. In cosmology, entropy plays a pivotal role in characterizing the evolution of the universe and its large-scale structures [3]. In information theory, the concept of entropy, as introduced by Claude Shannon, serves as a measure of information content and uncertainty in communication systems [4]. And, in materials science, entropy is used to explain the stability and behaviour of complex materials, such as spinel high-entropy oxides [5].

In physics, entropy is most easily understood differently depending on the scale of the system. For macroscopic systems, it is often useful to think of entropy as a measure of a system's thermal energy per unit temperature that is unavailable for doing useful work [6] – a quantity that is usually deduced indirectly via the heat capacity of the system. On the other hand, for very small systems that consist of only a handful of particles, entropy is more easily understood in terms of the number of microstates available to the system [7] – a quantity that is directly related to the number of quantum states accessible by the system. In such systems, particularly those

1.2. Motivation

consisting of only a handful of particles, the heat capacity is vanishingly small; thus, a different approach to measuring entropy is required. In 2018, just prior to the start of my PhD, a first attempt at a microscopic entropy measurement demonstrated the potential to take advantage of a Maxwell relation to detect the minuscule entropy changes associated with a system containing only a single electron [8]. Although an interesting demonstration, the procedure employed in Ref. [8] lacked the generality to be applied to systems of significant scientific value. This thesis will cover the details of developing and testing a novel technique – based on this early demonstration – that generalizes the approach to measuring entropy in extremely small systems.

1.2 Motivation

A lecture given by Richard Feynmann in 1959 titled “There’s plenty of room at the bottom” [9], although not widely recognized until many years later, serves as a useful indication that physicists at the time were increasingly beginning to turn their efforts toward exploring the largely untouched microscopic world. This coincides with the growth of the field of mesoscopes; a sub-discipline of condensed matter physics that covers systems of an intermediate scale, between the microscopic (atoms and molecules) and macroscopic. Although there are not hard limits to what constitutes a mesoscopic system, typically the sizes range from nanometers to micrometers (Fig. 1.1 depicts the scale). In contrast to many macroscopic systems, which to a good approximation can be described by classical mechanics, describing systems on a mesoscopic scale often benefits from the application of quantum mechanics. The unique blend of quantum mechanics and our ability to manipulate these systems has allowed for the observation and control of many striking quantum phenomena, offering a myriad of possibilities for both fundamental research and practical applications.

While researchers have made significant strides in the fabrication and control of mesoscopic devices, the methods for measuring these systems remain comparatively constrained. Traditionally, measurements have largely

1.2. Motivation

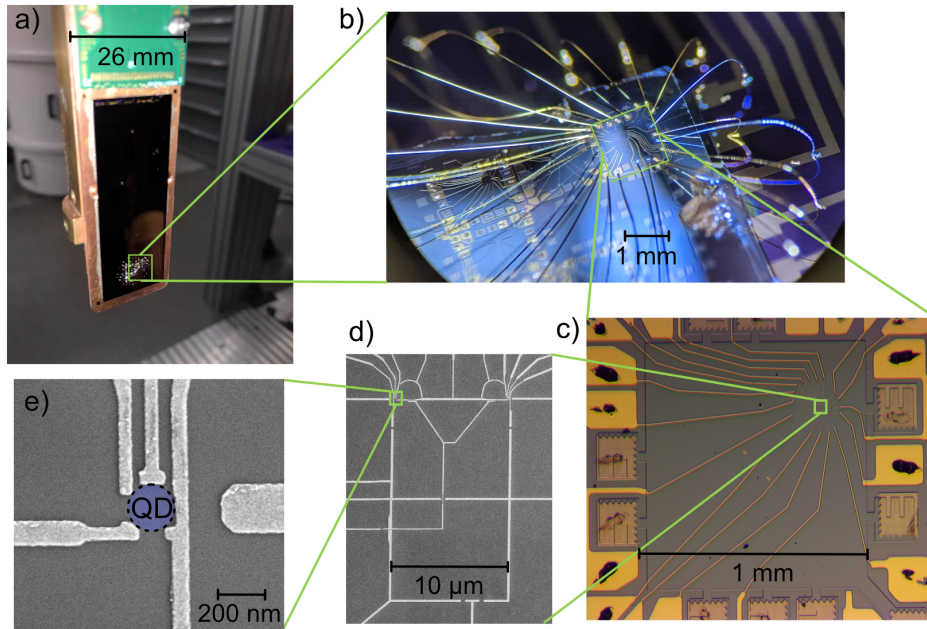


Figure 1.1: Images depicting the scale of mesoscopic measurements. **(a)** A photograph of a device on a Si wafer sample holder, mounted on the “cold-finger” of the cryostat. The cold-finger is 25.7 mm in diameter. **(b)** A photograph taken through a wire-bonder microscope of the top-right corner of the GaAs/AlGaAs heterostructure with a device (middle) wire-bonded to the gold contacts of the Si wafer sample holder. The full heterostructure chip (not fully in the image) measures 5×5 mm. **(c)** A microscope image of a single device, where it is mostly the outer gates and bond pads that are visible. The device bond pads form a 1×1 mm square around a 2DEG mesa in which the mesoscopic circuit is formed. **(d)** A scanning electron micrograph (SEM) of the full device including the relatively large ($10 \times 10 \mu\text{m}$) heating reservoirs. The bright features are the metal gates deposited atop the dark heterostructure surface. **(e)** An SEM image focused on the smallest features of the device. A 200×200 nm quantum dot that would typically contain < 5 electrons is indicated.

1.3. Outline

been limited to monitoring the transport of electrons through the system under various conditions – essentially, conductance measurements.

In this thesis, we discuss a novel technique for measuring mesoscopic systems by leveraging a Maxwell relation to directly probe entropy. Because the entropy of a mesoscopic system is directly related to the number of quantum microstates of the system, direct entropy measurement is particularly interesting as it can serve as a probe for the formation of exotic states in strongly correlated systems (due to the exotic quantum states directly affecting the number of microstates of the system). For instance, entropy has been proposed as a significant indicator of isolated non-abelian quasiparticles, such as Majorana zero modes in a superconductor [10], [11] or excitations of a fractional quantum Hall state [12]–[14], distinguishing them from more mundane abelian analogs.

1.3 Outline

Entropy is a crucial topic in this thesis, however, the development of our new measurement technique was an experimental endeavour that relied heavily upon the properties of mesoscopic devices. To the lay the groundwork, Chapter 2 first introduces the general features of these devices along with some more specific descriptions of measurement procedures. Subsequently, Chapter 3 focuses on entropy – delving into the scientific background, detailing alternative methods for entropy measurements in mesoscopic system, the theoretical framework of our work, and key concepts like the Kondo effect and the Numerical Renormalization Group (NRG) method.

The empirical work begins in Chapter 4, presenting a proof-of-concept measurement on a simple quantum dot to validate our new technique. Chapter 5 extends the new approach to a more complex system – a double quantum dot – highlighting the capability to measure the entropy of non-local systems. Then, in Chapter 6, the universality of the method is demonstrated through measurements of a quantum dot in a non-trivial regime where Kondo correlations are anticipated, with results compared to NRG calculations. Finally, Chapter 7 discusses promising preliminary measure-

1.3. Outline

ments that indicate the observation of a Kondo singlet via the entropy of the system. Chapter 8 synthesizes the key findings and provides insights into future directions for enhancing and applying the entropy measurement techniques developed in this work.

Chapter 2

Mesoscopic Devices

A prerequisite to the direct entropy measurements of nanoscale systems is the design and fabrication of the devices with which our experiments are performed. Our devices are comprised of quantum dots (QDs) and quantum point contacts (QPCs) that are formed in the two-dimensional electron gas (2DEG) located at the heterojunction interface of a GaAs/AlGaAs heterostructure. A description of these device components follows.

2.1 2DEG Heterostructures

A heterostructure is a layered structure that contains one or more interface(s) between differing semiconductors, called heterojunctions. Heterostructures are extensively used in modern electronic devices, such as transistors and diodes, and can be crafted using a variety of semiconductor materials. With certain configurations of semiconductors at the heterojunctions, heterostructures can lead to a fascinating physical phenomenon: a strongly confined two-dimensional electron gas (2DEG). Such a device was first fabricated in 1978 [15] and allowed researchers to clearly observe non-classical behaviour that arises from the strong confinement – an idea first postulated in 1957 [16].

Direct bandgap semiconductors gallium arsenide (GaAs) and aluminum gallium arsenide (AlGaAs) are prototypical semiconductors used for the formation of 2DEGs due to their closely matching lattice constants, including in the devices used to facilitate the work described in this thesis. The coloured layers in the schematic shown in Fig. 2.1a depict the typical heterostructure layers that form the 2DEG (at the lower boundary between GaAs and AlGaAs) of the devices discussed in this thesis. The fabrica-

2.1. 2DEG Heterostructures

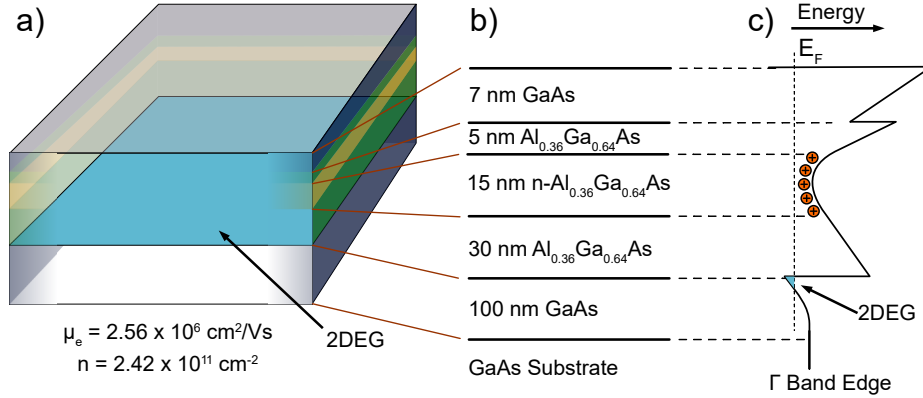


Figure 2.1: (a) Three-dimensional schematic of a heterostructure (not to scale) showing the location of the 2DEG in blue along with the electron mobility μ_e and density n of the 2DEGs used in this thesis. (b) Layer compositions and thicknesses of the heterostructures. (c) Conduction band diagram indicating the location of uniform doping (orange circles) and δ -doping along with the triangular well that hosts the 2DEG.

tion of these heterostructures is carried out by our collaborators at Purdue University [17]–[19] via Molecular Beam Epitaxy (MBE). The use of MBE for the growth of these structures allows precise control over the thickness, composition, and doping of each layer – all of which are crucial for the formation of a high-quality 2DEG. GaAs exhibits a bandgap of 1.42 eV at room temperature [20], while $\text{Al}_x\text{Ga}_{1-x}\text{As}$ has a tunable bandgap, ranging from 1.42 to 2.16 eV, depending upon the aluminum content (x) [21]. This tunability of AlGaAs along with the very similar lattice constants of AlGaAs and GaAs (5.662 Å and 5.653 Å respectively [22]) makes these materials ideal for forming high-quality 2DEG hosting heterostructures.

It is the combination of the close match in the lattice constants of GaAs and AlGaAs along with the precision of MBE and a specific doping strategy that enables the formation of a nearly defect-free interface between the two semiconductors, which in turn allows a highly mobile 2DEG to form. While n-type doping is necessary to provide the excess of electrons that form the 2DEG, it must be done carefully to maintain high mobility in the resulting

2.1. 2DEG Heterostructures

2DEG. Typically, dopants are added uniformly throughout the growth of a heterostructure. For the formation of 2DEGs, however, this is not a suitable doping strategy: it causes a loss of electron mobility and an increase in charge noise at the 2DEG as a result of introducing inhomogeneities and deep donor levels (DX centers) close to the 2DEG heterojunction [15], [23]–[26]. This severely limits the usefulness of the 2DEG for the investigation of quantum phenomena. Instead, a process called modulation-doping is used to strategically increase the density of the 2DEG whilst maintaining high mobility [15], [27].

Modulation doping involves spatially separating conduction electrons from their parent donor impurity atoms [15]. This reduces the influence of impurity scattering on the conduction electrons, facilitating the formation of a high-mobility 2DEG. In the heterostructures discussed in this thesis, 100 nm of pure GaAs is first evaporated on the GaAs substrate to ensure a clean interface. Then the AlGaAs at the GaAs/AlGaAs boundary is deposited without any intentional doping for the first 30 nm to act as a spacer layer (Fig. 2.1b). This is followed by 15 nm of uniformly doped ($4.8 \times 10^{18} \text{ cm}^{-3}$) AlGaAs. Finally, a 5 nm layer of pure AlGaAs and 7 nm of pure GaAs cap the structure. With an unintentional doping rate as low as $\sim 10 \times 10^{13} \text{ cm}^{-3}$ [17], the 2DEG hosting interface remains relatively defect-free. While the specific composition of doping can drastically change the properties of the 2DEG, the 2DEGs used for the measurements throughout this thesis exhibit an electron density $n = 2.42 \times 10^{11} \text{ cm}^{-2}$ and electron mobility $\mu_e = 2.56 \times 10^6 \text{ cm}^2/\text{Vs}$.¹

As shown in Fig. 2.1c, because of the larger bandgap of the AlGaAs than GaAs, the electrons from the donor atoms in the AlGaAs prefer to drop down into the lower-energy GaAs conduction band at the GaAs/AlGaAs interface (despite the spatial separation). This bandgap difference in combination with the attractive potential of the now positive donor atoms traps the electrons in a near triangular potential well at the heterojunction. The very short length scale of this triangular potential well results in the formation of two-dimensional subbands in the well. Typically, the heterostructures

¹Electron mobilities an order of magnitude larger are not uncommon [17].

2.2. Quantum Point Contacts (QPCs)

are designed such that only the lowest energy subband is populated at low temperatures, thereby forming the quasi-2D electron gas [28], [29].

For the devices discussed in this thesis, the 2DEGs were separated into an array of “mesas” by chemical etching, using a UV laser writer to define the mesas. This was followed by electron beam lithography to define NiAuGe ohmic contacts that enable electrical contact to be made to the 2DEG that lives 57 nm below the surface of the heterostructure. The ohmic contacts are metallic pads that are diffused from the surface of the heterostructure down to the 2DEG via rapid thermal annealing. For a detailed description of a mesa etching and ohmic fabrication see Ref. [30]. Additionally, 10 nm of HfO₂ was deposited by atomic layer deposition. This dielectric layer helps to further insulate gates (discussed below) from the 2DEG, improving gating stability [31], [32].

2.2 Quantum Point Contacts (QPCs)

Quantum Point Contacts (QPCs) are local constrictions of the 2DEG to a short one-dimensional channel (Fig. 2.2). They are formed by applying an electric potential to metal “gates” on the top of the heterostructure. QPCs are a crucial component of many 2DEG devices and can be used for various purposes. Here, I will briefly describe how they are formed and their behaviour.

Figure 2.2a shows a simple schematic of a typical QPC. To fabricate the QPC (and any other gate structures), a process of electron beam lithography followed by metal evaporation is used to form ~ 10 nm thick metal gates on the surface of the heterostructure (~ 50 nm above the plane of the 2DEG). By applying a negative potential to the two metal gates relative to the 2DEG, the density of states in the 2DEG is reduced near the gates. With a negative enough potential, the 2DEG is completely depleted, preventing electron flow in those regions. If the two gates are placed close enough to each other (~ 200 nm), it is possible to form an effectively 1D channel between them.

At low temperatures (< 1 K), the conductance through the QPC is quan-

2.2. Quantum Point Contacts (QPCs)

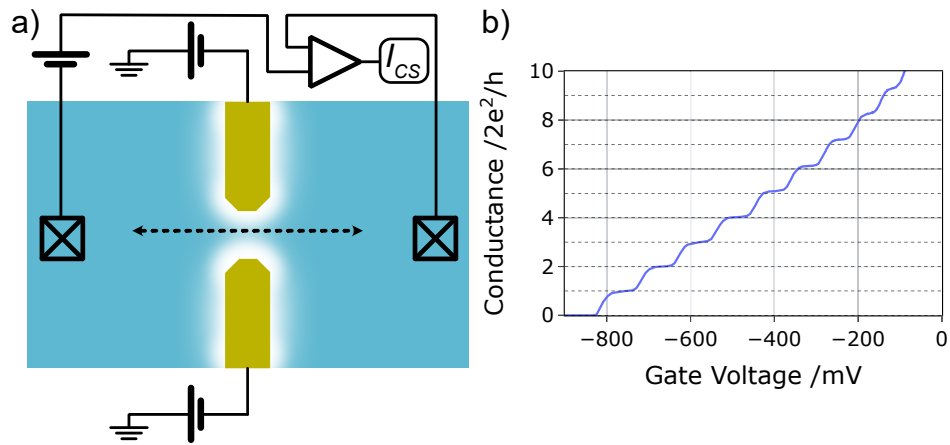


Figure 2.2: (a) A top-down schematic of a quantum point contact formed in the 2DEG (blue) between two gates (gold) with negative potential applied. The white region around the gates indicates the depletion of the 2DEG in proximity (and under) the gates. Crossed squares represent ohmic contacts through which the conductance of the QPC (dashed line) can be measured using an external voltage source and current amplifier. (b) A typical measurement of the quantized conductance plateaus of a quantum point contact at low temperature, including “pinch off” at -830 mV. The gate voltage is applied to both gates.

2.3. Quantum Dots

tized in steps of $2e^2/h$ (Fig. 2.2b) [33]–[37]. This is a result of the additional confinement forming a series of 1D subbands that (in the absence of a magnetic field) can each be occupied by a spin-up and down electron; therefore, each subband contributes $2e^2/h$ to the conductance of the QPC. As the negative potential on the two gates is reduced (from left to right in Fig. 2.2b), the steps in conductance correspond to the energy level of additional 1D subbands falling below that of the Fermi energy of the 2DEG.

The simple structure that is a QPC has been used in various ways, including investigating the ballistic nature of electrons in a 2DEG [38]–[46], forming highly sensitive charge sensors [47], [48], and creating a detector for spin-polarization [49], to name a few. In our work, we make use of them as charge sensors, heaters, and controllable tunnel barriers for quantum dots.

2.3 Quantum Dots

Because we are interested in measuring systems with only a few electrons, the next logical step after confining the 2DEG to 1D with a QPC is to further confine a region of 2DEG to a zero-dimensional space, called a Quantum Dot (QD). Figure 2.3a shows a simple schematic of such a device. The left and right gates form two QPCs between them and the bottom gate. Then, in combination with the middle gate, they can enclose a small region of the 2DEG to form a QD. Figures 2.4a and 2.6 also contain QDs with different gate geometries.

To form a QD, the two QPC gates must have sufficient negative potential such that the conductance of both QPCs individually are less than $2e^2/h$, thus forming tunnel barriers. The middle gate must first be negative enough that the 2DEG is fully depleted between it and the two QPC gates to either side; then it can be further fine-tuned to control the energy levels in the quantum well that is formed (Fig. 2.3a).

When a source-drain voltage bias V_{SD} is applied across the quantum dot (with $T, eV_{SD} < E_C$, where T is the system temperature and E_C is the charging energy of the QD), the transport of electrons through the dot depends on the alignment of the Fermi levels in the 2DEG leads with the

2.3. Quantum Dots

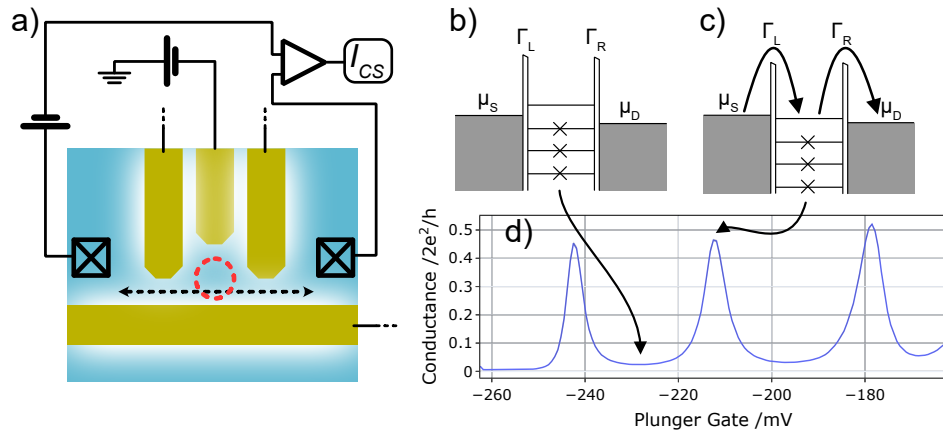


Figure 2.3: (a) A schematic of a quantum dot (dashed red circle) formed in the 2DEG (blue) between 4 gates (gold). Crossed squares indicate Ohmic contacts through which the conductance of the QD can be measured by applying an external bias and measuring the resulting current. (b and c) Coulomb blockade energy diagrams of a QD with coupling strength Γ_L and Γ_R to the 2DEG leads. The chemical potential of the leads is μ_S and μ_D where $eV_{SD} = \mu_S - \mu_D$. The lines marked with crosses indicate the occupied energy levels in the QD, where the spacing between them is the charging energy E_C of the QD. In panel b the QD is insulating as the chemical potentials of the leads fall between energy levels of the QD preventing any first-order tunnelling processes. In panel c the QD is conducting due to the energy level of the QD falling between μ_S and μ_D such that first-order tunnelling processes can occur. (d) The conductance through a QD as plunger gate (top middle gate in panel a) voltages is swept.

2.3. Quantum Dots

discrete quantum levels within the quantum dot. As shown in Fig. 2.3c, transport can only occur when an energy level within the quantum dot lies between the Fermi levels of the source and drain leads, thus allowing an electron to consecutively tunnel into and out of the quantum dot.

This conductance dependence on the energy level of the QD can be more clearly observed by varying the energy levels in the QD by sweeping the potential on the plunger gate. Each time an energy level in the QD falls between the Fermi energy of the leads, the QD will become conducting, and otherwise the QD will be insulating. This results in periodic conductance peaks that correspond to a change in the average occupation of the quantum dot (Fig. 2.3d), a phenomenon known as Coulomb blockade. Such a device is also known as a single electron transistor (SET).

In addition to the charging energy E_C that arises from Coulomb interactions, small quantum dots exhibit discrete energy levels akin to atomic orbitals in atoms [50]. The orbital level spacing Δ arises as a result of the de Broglie wavelength of the electrons being comparable to the size of the QD, and scales as $\Delta \propto l^{-2}$, where l is the dot size [51]. For the majority of the QDs discussed in this thesis, $\Delta \gg k_B T$,² and therefore the QDs exhibit a discrete density of states where only the lowest orbital energy level need be considered. Due to the large orbital level spacing in small QDs, when an odd number of electrons populate the dot, it will exhibit a net spin. This arises because, in accordance with the Pauli exclusion principle, all other electrons form spin-singlet pairs, leaving only one electron in the highest energy state without a paired spin. This property is particularly relevant to the discussion of the Kondo effect in QDs (Section 3.2.2).

Quantum dots have been used in a wide range of research and are often used as the building blocks of spin-qubit quantum computers [52]–[57]. For our purposes, we use QDs as both sensors and building blocks for constructing more complex quantum circuits to study many-body quantum phenomena.

²The exception being the big dot, discussed in Chapter 7, where $\Delta \ll k_B T$, thus resulting in an effectively continuous density of states.

2.4. Charge Sensors

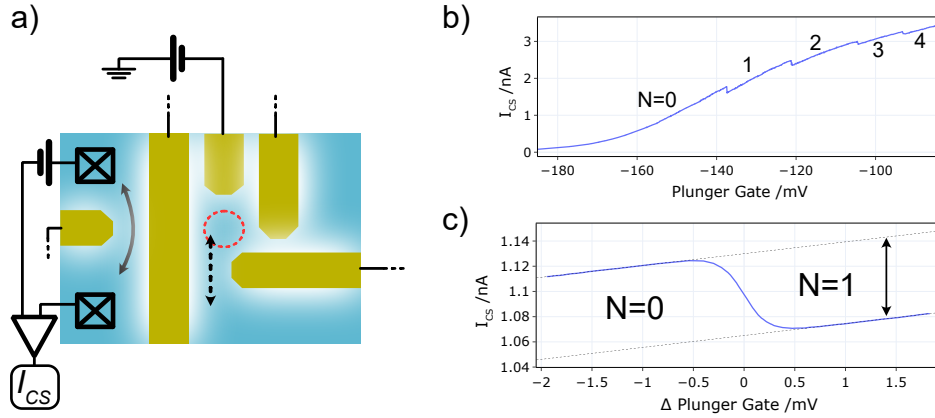


Figure 2.4: (a) A schematic of a charge sensor QPC in close proximity to a QD. The vertical gate in the middle forms both, the charge sensor QPC in conjunction with the left gate, and the QD with the remaining gates on the right. The QD has only one lead through which electrons can enter or leave (dashed arrow). (b) Current through the charge sensor QPC with fixed bias as the plunger gate of the QD is swept over a wide range such that the QD is unoccupied at the left, and contains 4 electrons at the far right. Each sawtooth step indicates a change in the occupation of the QD. (c) A much narrower and higher resolution scan showing the change in plunger gate voltage from the first sawtooth in panel b at -138 mV showing the thermally broadened Fermi distributed charge transition of the QD at 100 mK. The vertical arrow represents the sensitivity of the charge sensor to the addition of one electron to the QD.

2.4 Charge Sensors

For the measurement of entropy, the capability to monitor the charge of the QD is crucial. As depicted in Fig. 2.4a, this is achieved by placing a QPC in close proximity to the QD.

The functioning of a QPC as a charge sensor is based on the sensitivity of the conductance of a QPC to the electrostatic environment near the QPC. As the charge state of the nearby quantum dot changes due to the addition or removal of an electron (or more precisely the time average occupation of the QD), the resulting change in the electrostatic environment modulates the conductance of the QPC. By continuously monitoring the conductance

2.5. Determining Electron Temperature

of the QPC (typically a current measurement with 100 uV DC bias) as the plunger gate is swept, it is possible to infer the occupation of the quantum dot with a precision $\sim 0.01e$. Figure 2.4b shows a typical measurement of the current through a charge sensor as the plunger gate voltage is varied over a wide gate voltage range, leading to sequential tunnelling of several electrons into the QD. The overall slope of the conductance through the QPC is a result of the direct cross capacitance between the sweeping plunger gate and the QPC, and the sudden steps indicate when the occupation of the QD increases as a result of the energy level of the QD falling below that of the Fermi sea. For the measurements presented in this thesis, the sweep range is typically limited to a small window around a single charge transition so that we can accurately resolve the fractional time average occupation of the QD as a result of thermal or coupling-strength broadening (Fig. 2.4c).

2.5 Determining Electron Temperature

Another key requirement for our entropy measurement protocol is the ability to determine the electron temperature precisely. For the addition of an electron to a QD with weak tunnel coupling to an electron reservoir, the charge sensor current I_{CS} lineshape is given by

$$I_{CS} = I_{amp} \tanh\left(\frac{V_P - V_{mid}}{2\Theta}\right) + \gamma V_P + I_{const}, \quad (2.1)$$

where I_{amp} is the amplitude of the charge transition (the sensitivity of the charge sensor to the occupation of the QD), V_P is a plunger gate potential, $\Theta = \frac{k_B T}{\alpha e}$ is the thermal broadening in units of gate voltage, $\alpha \equiv d\epsilon/dV_P$ is the lever arm, γ represents the direct cross capacitance between the plunger gate and the charge sensor and I_{const} is a constant offset.

Figure 2.5a depicts fits of Eq. 2.1 to charge transition measurements taken at 100 and 200 mK, where fitting is performed using least squares minimization allowing all parameters to vary. To facilitate an accurate determination of electron temperature T_e , the Θ parameter is extracted from a fit to a heavily averaged measurement of the charge transition. Typically,

2.5. Determining Electron Temperature

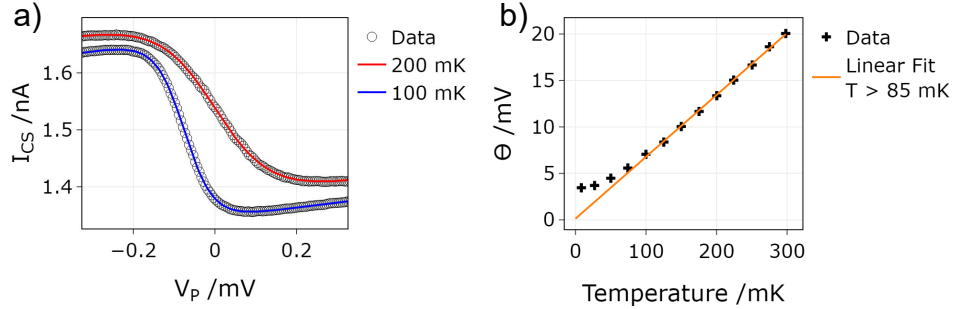


Figure 2.5: (a) Fits of Eq. 2.1 to charge sensor current measurements of the addition of an electron to a QD in a weakly coupled regime at $T = 100$ and 200 mK. Each dataset represents the average of many repeated measurements, and are offset from each other for clarity. Note that the x-axis represents fine-tuned gate potentials applied in addition to a coarse potential that is not shown. (b) The extracted Θ parameters from fits to charge transition measurements over a range of cryostat temperatures from 8 mK to 300 mK. A linear fit of the Θ s for $T > 85$ mK is shown, extrapolated back to $T = 0$.

100 or more repeated measurements of the charge transition are averaged together after aligning them based on the V_{mid} parameter of fits of Eq. 2.1 to each trace individually. This averaging procedure is necessary because of electrostatic fluctuations that occur as a result of nearby charge motion in the dopant layer of the heterostructure. These fluctuations affect the QD energy ϵ , effectively shifting the charge transition left/right with a frequency spectrum typically between $1/f$ and $1/f^2$ [19], [23]. Therefore, by measuring individual charge transitions quickly, and aligning the transitions before averaging, we mitigate the otherwise broadening effect of these electrostatic fluctuations.

For the conversion from Θ to T_e that will allow us to use this procedure as an electron temperature thermometer, we require the lever arm α . While there are several ways α can be determined, a convenient method is to measure a charge transition at a cryostat temperature where the electron temperature remains in thermal equilibrium with the cryostat. In practice, it is preferable to take measurements for a range of cryostat temperatures,

2.6. Additional Measurement Procedures

typically from 300 mK down to the base temperature of the cryostat (typically ~ 8 mK in our cryostats). Figure 2.5b depicts Θ extracted from measurements over such a range. From these measurements, it is clear that, for $T > 100$ mK, the thermal broadening Θ has a directly proportional relationship with the cryostat temperature T . A linear fit can then be used to calculate α , and thus convert any Θ to electron temperature T_e . If the linear fit does not extrapolate through the origin, it suggests either that the coupling of the QD to the reservoir does not meet the condition $\Gamma \ll k_B T_e$, or that significant voltage noise is present, which can blur the charge transition.

The deviation of Θ from a directly proportional relationship with T for $T \lesssim 100$ mK in Fig. 2.5b indicates that the 2DEG electrons are no longer in thermal equilibrium with the cryostat (the heterostructure itself does remain in thermal equilibrium with the cryostat). This is a result of the weakening electron-phonon interaction $\propto T^5$ [58] and the presence of electrical noise that persists despite the filtering implemented in the cryostat wiring. Typically, this results in a base electron temperature ~ 30 mK. Observing higher base electron temperatures may suggest increased electrical noise affecting the sample. This could be due to issues like compromised cryostat electrical filtering or external setup problems such as ground loops or overloaded power supplies.

2.6 Additional Measurement Procedures

In the experiments discussed in this thesis, some additional measurement procedures warrant further explanation.

To reduce charge noise in our device measurements, we cool down our devices with a positive bias applied to all of the gates that will be operated in a depletion regime. An in-depth investigation of the effects of bias cooling is presented in Ref. [23]. Effectively, charge carriers that are present in the doped layers of the heterostructure are mobile at high temperatures and move to screen the positive potential applied to the electrically isolated gates. Upon cooling, these carriers freeze in place and remain even after the positive bias is removed. In addition to reducing charge noise, these trapped

2.6. Additional Measurement Procedures

negative charges under the gates decrease the negative potential that must be applied to the gates to deplete the 2DEG beneath them. In essence, a positive cool-down bias of, for example, +100 mV can be equated to an additional ~ -100 mV applied to the gate once cooled.

It is often desirable to control a specific parameter in an experiment in isolation (such as dot energy ϵ). However, it is often the case that the specific parameter is either, not controlled by a single gate potential, or the gate potential that primarily affects that parameter also significantly affects other parameters (such as a coupling Γ). In these cases, we can utilize a combination of gates to form a virtual gate. A virtual gate is a linear combination of two or more real gates that when combined effectively target a specific parameter of the system. For example, consider two physical gates, Gate A and Gate B, near a quantum dot. If Gate A predominantly changes dot energy but also affects coupling, and Gate B predominantly changes coupling but also affects dot energy, a combination of voltages on Gate A and Gate B can be found that changes the dot energy without substantially affecting the coupling. As an example of the naming convention used throughout this thesis, the combined virtual gate would be called A' (denoting that A is the primary gate). Typically, the non-primary gates vary over a smaller range and with the opposite sign to the primary gate. Note that only the primary gates potentials are shown on the axes of figures throughout this thesis; it is implied that the secondary gates are adjusted as necessary.

Similarly, we often require very fine control over gate potentials, including adjusting around specific values significantly distanced from zero, like -500.001 mV. This large offset from zero prevents us from using a simple potential divider on the digital-to-analog converter (DAC) output. To overcome this, we combine potentials. Instead of utilizing the combined effect of multiple gates (as we do with virtual gates), we combine the outputs of multiple DAC channels that are connected to a single gate. The DACs (AD574) each have a range of ± 10 V and a step size of 0.305 mV (20 V/ 2^{16}). We typically operate in the -2 to 1 V range, but often require a precision < 1 μ V. Practically, we achieve this by combining two DAC outputs with

2.7. Summary

a passive voltage adder circuit; essentially two potential dividers that share the same resistor to ground. We use a small potential divider for one DAC channel (typically $\frac{1}{2}$), and a much larger potential divider for the second DAC channel (typically between $\frac{1}{100}$ and $\frac{1}{10000}$). The combination of the two DACs allows us to vary gate potentials with a very high level of precision (< 100 nV) over a very wide range of gate voltages (-5 to 5 V). Out of convenience for analysis and interpretation, we often work with and display only the values of the fine-tuned DAC potentials (that typically vary around 0 mV). In reality, however, a combined potential is applied to the gate.

2.7 Summary

Figure 2.6 shows a three-dimensional schematic of many of the key components typical of the devices discussed throughout this thesis. This schematic can be used to combine many of the ideas discussed in this chapter. The white regions represent places where the 2DEG is depleted by the combination of frozen-in charge carriers (from a positive cool-down bias) in addition to the potentials applied to the gates. Ohmic contacts that provide an electrical connection from the surface of the heterostructure down to the 2DEG are shown on either side of a quantum point contact (QPC) that acts as a charge sensor for the quantum dots. A bias of 100 μ V is typically applied across the ohmics, with the resulting current measured using a current-to-voltage amplifier (Basel SP983c). The gate directly between the ohmics is used to tune the charge sensor to its most sensitive regime ($G \approx \frac{e^2}{h}$) via the combination of coarse and fine-tune DAC channels that are added with a passive potential adder. The QD closest to the charge sensor has an additional “accumulation” gate, so-called because we originally intended to accumulate electrons under it by applying positive potential. In practice, the accumulation gate is typically used for fine tune control of the QD energy (only varied near 0 V) as it couples more strongly (larger lever arm α) to the QD energy than the conventional plunger gate (the gate that also defines the top side of the QD). A virtual gate is often made from the accumulation gate and charge sensor gate such that the dot energy can be varied with the

2.7. Summary

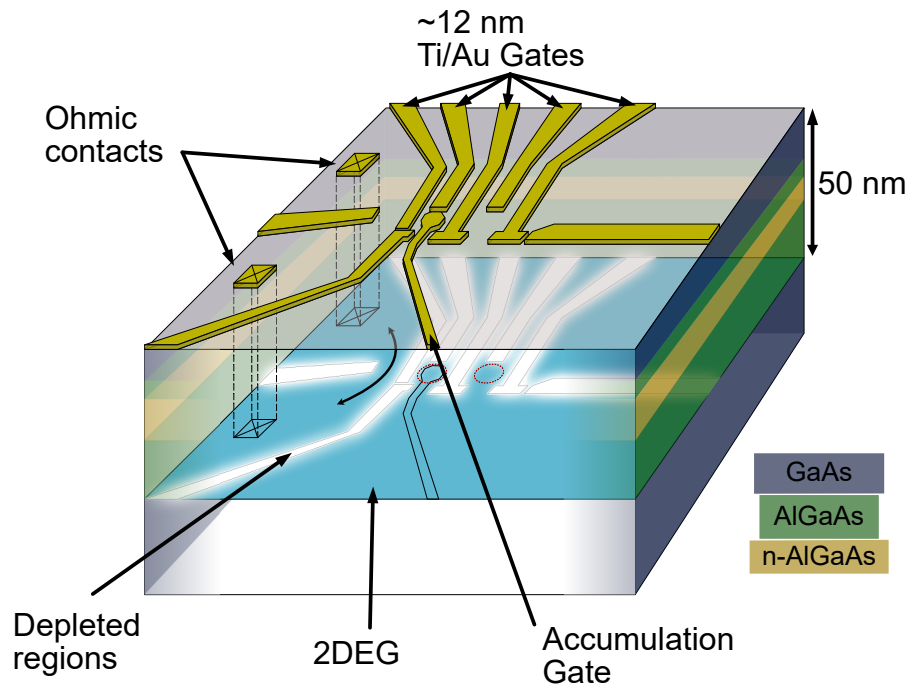


Figure 2.6: Three-dimensional schematic (not to scale) of a device with a charge sensor, two quantum dots, and an “accumulation gate” in one of the QDs. Where most gates typically have negative enough potential to deplete the 2DEG underneath them (white regions), the accumulation gate is typically held close to 0 V and so is largely invisible to the 2DEG (black outline depicts where the 2DEG *would* deplete with a negative bias applied).

2.7. Summary

direct cross-capacitive effect of the accumulation gate on the charge sensor QPC cancelled out. For example, as the (primary) accumulation gate is swept more positively, a corresponding linear negative change of the (secondary) charge sensor gate potential holds the current through the charge sensor QPC roughly constant, excluding the changes in current that result from change in QD occupation.

The vast majority of measurements conducted on mesoscopic systems thus far depend upon conventional conductance measurements through the system of interest (a method that, while valuable, is often limited in its ability to provide insight into the system's quantum state). The advent and refinement of 2DEG heterostructure fabrication as well as the development of gating techniques have enabled the development of progressively more complex devices. Only now, with access to such devices, is a novel entropy measurement like that described in this thesis feasible.

Chapter 3

Background

This chapter provides the theoretical and methodological context for the research in this thesis. It begins with an overview of entropy in mesoscopics and describes the progress made with conventional heat capacity techniques, highlighting the requirement for a fundamentally different approach. Alternative approaches (developed concurrently with the work presented here) are summarized, followed by the theoretical framework upon which our novel technique is based. The Kondo phenomenon that is measured in later chapters is explained, with a particular focus on its manifestation in mesoscopic devices. Finally, the numerical renormalization group (NRG) method – employed to generate theoretical predictions to which we compare experimental data – is described at a high level.

3.1 Entropy

Entropy is generally understood as a measure of disorder and can be described by a number of different formalisms.³ This section narrows the scope to the relevant formalisms, provides an overview of related techniques and measurements, describes the technical details of the approach to entropy measurement that we have developed, and compares our approach with other approaches that have been developed in the last few years.

³Including Shannon Entropy, Boltzmann Entropy, Gibbs Entropy, von Neumann Entropy, Tsallis Entropy, and Reyni Entropy.

3.1. Entropy

3.1.1 Entropy in mesoscopics

Most readers' introduction to entropy was likely through the Boltzmann equation:

$$S = k_B \ln(\Omega), \quad (3.1)$$

which defines the total entropy of the system based on the number of possible microstates, assuming all states are equiprobable. For the purposes of the experimental development of a direct entropy measurement technique, as described in this thesis, the Boltzmann equation must be extended to handle non-equiprobable states. Such a formalism is known as the Gibbs entropy, and is defined as follows:

$$S = -k_B \sum_i p_i \ln(p_i), \quad (3.2)$$

where k_B is the Boltzmann constant, and p_i is the probability that the system is in microstate i . To understand why the Gibbs entropy (as opposed to Boltzmann entropy) is required to model the entropy of our systems, consider the simple case of a QD that is weakly coupled to a reservoir of electrons (a lead) and whose average occupation can be continuously changed from 0 to 1 electron.

$\langle N \rangle$	$P(0\rangle)$	$P(\uparrow\rangle)$	$P(\downarrow\rangle)$	Entropy / k_B
0	1	0	0	$\ln(1) = 0$
1/4	3/4	1/8	1/8	0.74
1/2	1/2	1/4	1/4	1.04
2/3	1/3	1/3	1/3	$\ln(3) = 1.10$
3/4	1/4	3/8	3/8	1.08
1	0	1/2	1/2	$\ln(2) = 0.69$

Table 3.1: A few examples of the probability of QD state and corresponding QD entropy for $0 \leq \langle N \rangle \leq 1$. $|0\rangle$ represents the unoccupied state while $|\uparrow\rangle$ and $|\downarrow\rangle$ represent the QD occupied with a spin up or down electron respectively. Entropy is calculated using the Gibbs formula (Eq. 3.2) with exact values shown where non-zero probabilities are equal (i.e. Eq. 3.1 applies).

In this very simple example, there are two main parts to the thermody-

3.1. Entropy

dynamic system: the reservoir and the QD. Because the reservoir has, effectively, an infinite number of electrons (it is grounded), the reservoir part of the system does not change when an electron is added to the QD. Therefore, we can ignore its contribution to the total entropy of the system and focus on the QD alone. Then, there are only three possible states for the QD part of the system: it is either unoccupied ($|0\rangle$) or occupied with a spinful electron ($|\uparrow\rangle$ or $|\downarrow\rangle$). Table 3.1 shows the probability that the QD occupies each of these states for various average occupation $\langle N \rangle$ along with the entropy associated with the QD at that point (calculated using Eq. 3.2). Notably, when $\langle N \rangle = 2/3$, the probability for the system to occupy each of the three states is equal, hence the maximal entropy of $k_B \ln(3)$ (that can be determined directly from Eq. 3.1). For any other occupation between 0 and 1, while the probability of $|\uparrow\rangle$ and $|\downarrow\rangle$ remain equal to each other, they differ from that of $|0\rangle$ and thus Eq. 3.2 is required.

Note that this simple example is valid only under a specific set of circumstances. The magnetic field must be zero for the energy levels of the QD to be spin degenerate [59]. Additionally, the thermal energy $k_B T$ of the system must be small compared to both the charging energy ($k_B T < E_C$) and the orbital spacing of the QD ($k_B T < \Delta$) for us not to have to consider states with two electrons and for there to be no occupation of excited states, respectively. With these constraints, in the example scenario (as described in Table 3.1), the time average occupation of the QD $\langle N \rangle$ only includes contributions from the lowest energy single electron states of the QD ($|\uparrow\rangle$ and $|\downarrow\rangle$), or the unoccupied state ($|0\rangle$).

The Gibbs entropy is a calculation of the total entropy of a system;⁴ however, measurements (including our own) are typically sensitive to the change in entropy. In the example given, the initial unoccupied QD only has one possible state ($S = k_B \ln(1) = 0$). Therefore, the total entropy and the entropy change of the system are equal ($\Delta S = S$). However, Chapter 5 will describe several measurements in which the initial and final state of the QD part of the system both have a finite entropy. In these cases, entropy

⁴Of course, the true total entropy of the system would include the entropy of the electron reservoir, and therefore the previous example is already a simplified model.

3.1. Entropy

change must be calculated to compare to measured values.⁵

Even in a system as simple as that presented in Table 3.1, where the physics is well established, the measurement of entropy remains interesting in its own right as a direct probe of the quantum microstates of a confined electron. Of course, the ability to directly probe information about the quantum states of the system becomes increasingly interesting when applied to systems that are expected to exhibit more exotic quantum states.

There are numerous systems where the measure of entropy would be useful for distinguishing exotic states, including non-abelian anyons in the $\nu = 5/2$ fractional quantum hall (FQH) state [14], neutral edge modes in FQH [60], and Fibonacci anyons in a 3-channel Kondo state [61], [62]. A particularly noteworthy example of an exotic state system of interest is that of one containing a Majorana Zero Mode (MZM). As a type of non-abelian anyon, MZMs can enable topological quantum computation, where the braiding of MZMs would facilitate robust, fault-tolerant unitary operations thanks to their non-trivial topological state that remains immune to weak local perturbations [63]. The problem with MZMs is that they are notoriously difficult to detect through conventional conductance measurements [64]–[66]. Through a direct entropy measurement, however, a non-trivial $\frac{1}{2}k_B \ln(2)$ entropy would clearly distinguish them from non-topological states [11]. For a more thorough description of how a measurement such as this is possible with the entropy measurement protocol discussed in this thesis, see Section 5.6.

3.1.2 Conventional entropy measurement applied to mesoscopics

The conventional technique for measuring the entropy of a system is via heat capacity $C = Q/\Delta T$ – a quantity that can be measured by observing the change in system temperature ΔT when a small amount of heat Q is

⁵It is also true that for several of the measurements in this thesis, the initial state of the QD part of the system corresponds to $N = 0$ and therefore $S = 0$; hence, the entropy change and total entropy of the system are equal ($\Delta S = S$), and in these cases, the terms entropy and entropy change may be used interchangeably.

3.1. Entropy

added, or vice versa. This quantity is connected to the system's entropy via the Clausius definition $dS = dQ/T$. By integrating the heat capacity as a function of T , the entropy change of the system can be calculated by:

$$\Delta S = \int_{T_1}^{T_2} \frac{C}{T} dT. \quad (3.3)$$

While this approach to determining entropy works well for macroscopic systems, as the size of the systems becomes smaller, one must measure ever-decreasing heat flows to calculate the specific heat capacity. As such, heat capacity measurements of 2DEG systems are considered to be some of the most challenging experiments due to the very small contribution of the electrons compared to the entire heterostructure [67]. Despite the difficulty, there have been a series of successful experiments that have measured the specific heat [67]–[70] and entropy [71] of 2DEG systems since the mid-1980s. The following descriptions of these measurements are intended to highlight the substantial progress that has been made toward applying more conventional entropy measurement techniques to mesoscopic systems, whilst also providing the context for the requirement of the fundamentally different approach that is discussed in this thesis.

One of the pioneering experiments of entropy-related measurements was conducted using heterostructures with 172 2DEG layers that were thermally isolated by suspension from superconducting wires [68]. Short (100 μ s) heating pulses were applied and the resulting temperature changes (~ 30 mK) measured at $T = 1.5$ K. By repeating this measurement at varying magnetic fields, and under the assumption that the field affects only the electronic contribution to specific heat, Gornik et al. were the first to be able to qualitatively detect the specific heat contribution of the 2DEGs to the total specific heat of the heterostructure via field dependent oscillations. Shortly after Gornik et al.'s 1985 experiment, Wang et al. [69] utilized AC calorimetry to measure the heat capacity of a 75-layer 2DEG system. Here, an oscillating heating current (driven at 750 Hz) induces temperature oscillations in the sample that can be measured at twice the heating frequency. This moderately fast oscillation of heat flux allowed them to measure the

3.1. Entropy

thermal response of the heterostructure before the heat dissipated to the sample holder or thermal bath (in contrast to the previous approach that attempted to thermally isolate the system with superconductors). Although this facilitated a more accurate measurement of the total system heat capacity, it is worth noting that even at 1.3 K,⁶ the authors estimated that 40% of the total contribution came from the wires and evaporated metals of the measurement apparatus (and that is compared to the full heterostructure, not just the 75 layers of 2DEG.) Nearly a decade later, Bayot et al. improved upon previous measurements using a combination of the previous two approaches to determine 2DEG heat capacity at temperatures as low as ~ 60 mK (similar to the temperatures we are interested in). This paper is the first to discuss the potential to use this type of measurement to probe the entropy of the electronic system. However, these measurements still took place in a 100-layer 2DEG system, far from the few electron limit which is the subject of this thesis. More recently, in 2007, Schulze-Wischeler et al. [70] made significant strides in reducing the scale of heat capacity measurements, moving away from layered systems to examine a meandering path (~ 10 nm) of a single 2DEG layer. They used yet another new strategy in which they applied very brief (10 ns) heat pulses to the back of the heterostructure that essentially bombards the 2DEG with ballistic phonons. This allowed them to measure the resistance change (and therefore ΔT) of the 2DEG as a result of the ballistic phonon heating before the 2DEG reached thermal equilibrium with the substrate [72]–[74]. This was the first measurement to directly measure the heat capacity of the electrons (albeit in arbitrary units) rather than deducing the electronic contribution from oscillations of total heat capacity versus magnetic field. Finally, the most recent result, published in 2017 by Schmidt et al. [71], took the same experimental methodology a step further by not only measuring the specific heat of a single layer 2DEG but also by using this measurement to calculate the entropy of the electronic system. In this experiment, square wave Joule

⁶We are interested in measuring systems at temperatures $40\times$ smaller (~ 30 mK)

3.1. Entropy

heating was applied to the system.⁷ By measuring the thermalization time between the electrons of the 2DEG and the phonons of the heterostructure, they were able to determine the specific heat of the 2DEG. Then, by integrating the specific heats measured over a range of temperatures (Eq. 3.3), they calculated the entropy change ΔS of the system between 40 – 150 mK.

3.1.3 Few-electron entropy-related measurements

The conventional heat capacity-based experiments described in Section 3.1.2 showed marked improvement over time, but even the most recent approach from 2017 demonstrated a measurement of $\sim 10^9$ electrons. Measuring entropy in few electron systems, such as the quantum dots that are the subject of this thesis, clearly requires a fundamentally different approach.

One approach to measuring the entropy at the quantum dot scale is to take advantage of the fact that the rate at which electrons tunnel into or out of a quantum dot in Coulomb blockade is directly related to the degeneracy (entropy) of the energy states of the QD [75]–[77]. This approach utilizes the general principle of detailed balance⁸ [78], [79] along with the ability to precisely measure electron tunnelling rates between a QD and a reservoir [77], [80], [81]. The tunnelling rates are determined by time-resolved detection of individual tunnelling events into or out of the QD using a charge sensor QPC in close proximity to the QD [77], [81], [82]. Intuitively one might expect the tunnelling rate in and out to be equal to one another in light of the time-reversal symmetry of tunnelling; however, this doesn't account for the degeneracies of the initial and final QD states. Ref. [77] claims, that on the basis of detailed balance, the tunnelling rates are proportional to the ratio of degeneracies of the N and $N+1$ states of the QD. Thus, ΔS is not measured directly but can be inferred when starting from a known state (e.g. $N = 0$). For example, observing a tunnelling rate into the QD ($N \rightarrow N+1$) as double (or half) the rate of tunnelling out ($N+1 \rightarrow N$)

⁷Coincidentally, this measurement bears a significant resemblance to the heating method we employ in measurements discussed in Chapter 4, although we use the information obtained very differently.

⁸The principle of detailed balancing is that, for a system in equilibrium, the average rate for every individual process is equal to its reverse process.

3.1. Entropy

implies a degeneracy increase (decrease) by a factor of two. Although this approach has been demonstrated to map the energy state degeneracies of quantum dots with a handful of electrons in both a GaAs/AlGaAs 2DEG [77] and in bilayer graphene [81], the method is specific to the measurement of extremely weakly coupled QDs where the tunnelling rate is slow enough that one can resolve individual tunnelling events.

Another more general approach is to utilize the Maxwell relation

$$\left(\frac{\partial S}{\partial N}\right)_T = -\left(\frac{\partial \mu}{\partial T}\right)_N \quad (3.4)$$

that connects the change in entropy S with respect to particle number N (that can be fractional), to the change in the chemical potential μ with the change of temperature of the system T [8], [12], [83], [84]. In a mesoscopic system, these quantities (μ , N , and T) are often relatively easy to measure or control; that having been said, a measurement protocol utilizing this equation was proposed in 2009 [12] as a means of detecting non-abelian quantum hall states, and it was almost a decade later before a related approach was used to measure the much more mundane entropy of a spin-1/2 electron [8]. In the measurement described in Ref. [8], the thermal response of the charge of a QD as its occupation is increased by one was measured with a lock-in amplifier (applying an AC bias that heats the 2DEG reservoir connected to the QD). Then, by assuming a thermally broadened charge transition lineshape and utilizing Eq. 3.4, they extracted the entropy change of the system as a parameter of a fit to the thermal response. While this approach had the advantage of not requiring precise calibration of the measurement itself, the reliance on knowledge of the charge transition lineshape specific to the system measured renders the approach unsuitable for more exotic systems (as further described in Chapter 4).

More recently, Eq. 3.4 was utilized to provide entropic evidence of a Pomeranchuk effect⁹ in magic-angle twisted bilayer graphene (MATBG) [84],

⁹The Pomeranchuk effect refers to a phenomenon where liquid He³ may solidify upon heating due to the large entropy of the paramagnetic solid phase [85], [86].

3.1. Entropy

[86].¹⁰ Although the two experiments approach the measurement of μ quite differently (with Saito et al. utilizing gates that span the entire device to make global measurements [87], and Rozen et al. utilizing a scanning single electron transistor to make local measurements in addition to global measurements), both measure μ relative to the charge neutrality point of the MATBG. In both measurements, the entropy change of the system is determined by the integral of Eq. 3.4 with respect to N , where they approximate $\partial\mu/\partial T$ from the finite difference of μ measurements at ~ 4 K and ~ 15 K. Although their measurements illuminated interesting behaviour in MATBG, their approaches benefitted from two key features that are atypical of the systems we are interested in: they were able to use the charge neutrality point as a reference for $\mu = 0$ that facilitates comparison of significantly time-separated measurements, and the interesting physics occurred over a higher and larger temperature range that significantly increases the signal-to-noise ratio.

A third approach to the determination of entropy in mesoscopic QD systems utilizes thermo-electric transport measurements [88]–[93]. The Mott relation, when applied to a mesoscopic system, describes a contribution to thermopower (or Seebeck coefficient) that arises from energy-dependent transmission through the system, dG/dE : if thermally-excited electron states above the Fermi energy exhibit a higher (or lower) transmission than thermally-excited hole states below the Fermi energy, a current will tend to flow toward (or away from) the cooler reservoir when the chemical potentials of both reservoirs are aligned. In addition to the aforementioned contribution to thermopower, there is another derived from entropy considerations: Eq. 3.4, for example. This Maxwell relation implies that, for a fixed average N on the dot, the associated reservoir chemical potential will vary between reservoirs at different temperatures, depending on the particular dS/dN . Consequently, in a standard thermopower measurement setup, where no current is permitted to flow, hot and cold reservoirs will tend to equilibrate at different μ . Therefore, by comparing thermopower

¹⁰In these papers, N and S from Eq. 3.4 are replaced by ν and s , the filling factor and entropy per moiré superlattice unit cell, respectively.

3.1. Entropy

predictions from the Mott relation to actual thermopower measurements, one can in principle gain insight into the entropy of the system in question. Moreover, predictions based on the Mott relation can, in theory, be derived from conductance measurements if one equates dG/dV_G to dG/dE (where V_G refers to the potential on a gate that tunes the local energy of the system). This is the approach proposed, and to some extent tested, in Ref. [90]. The problem with this approach is that dV_G and $d\mu$ are seldom directly connected, especially in mesoscopic systems that have strong interactions with their reservoirs. Consequently, making reliable predictions from the Mott relation using conductance measurements can be problematic.

3.1.4 Theoretical background of novel measurement technique

Here, the theoretical framework that underpins our novel entropy measurement protocol is described. In comparison to the approaches that utilize Eq. 3.4, our approach more naturally maps to quantities that are easy to control or measure experimentally, allowing us to avoid some of the simplifying assumptions that the other approaches rely on. We approach the problem of measuring mesoscopic entropy via a different Maxwell relation

$$\left(\frac{\partial S}{\partial \epsilon}\right)_{T,\mu} = -\left(\frac{\partial N_d}{\partial T}\right)_{\epsilon,\mu} \quad (3.5)$$

from that described in Section 3.1.3. Using this relation allows us to extract the entropy change of a system by measuring a change in the occupation of a QD N_d with varying temperature T as we quasi-statically change the dot energy ϵ . A useful derivation of Eq. 3.5 begins with the definition of the Grand Potential Φ_G (otherwise called Landau potential or Landau free energy):

$$\Phi_G \stackrel{\text{def}}{=} U - TS - \mu N$$

where U is the internal energy, N represents the number of particles, T is the temperature, and μ is the chemical potential of the system. In this

3.1. Entropy

equation, N refers to the total number of particles in the system, a quantity that we divide into N_{res} and N_d to denote the number of particles in the reservoir and dot respectively.

Crucially, the measurement protocol relies upon the QD's contribution to the total internal energy U of the system alone. By separating this ϵN_d contribution we obtain

$$\Phi_G = U - TS - (N_{\text{res}} + N_d)\mu + N_d\epsilon. \quad (3.6)$$

From here, we take partial differentials with respect to the dot energy ϵ and system temperature T .

$$\left(\frac{\partial\Phi_G}{\partial\epsilon}\right)_{T,\mu} = N_d \quad (3.7)$$

$$\left(\frac{\partial\Phi_G}{\partial T}\right)_{\epsilon,\mu} = -S \quad (3.8)$$

Then by equating

$$\frac{\partial^2\Phi_G}{\partial\epsilon\partial T} = \frac{\partial^2\Phi_G}{\partial T\partial\epsilon}, \quad (3.9)$$

we can obtain

$$\left(\frac{\partial N_d}{\partial T}\right)_{\epsilon,\mu} = -\left(\frac{\partial S}{\partial\epsilon}\right)_{T,\mu} \quad (3.10)$$

$$\left.\frac{dN_d}{dT}\right|_{\epsilon,\mu} = -\left.\frac{dS}{d\epsilon}\right|_{T,\mu}. \quad (3.11)$$

In this formulation, we have been careful in handling the subtle difference between ϵ of the dot, and μ of the reservoir. Specifically, we work under the approximation that the local gate-tuned potential of the QD couples only to the charge of the QD (e.g. we assume it does not affect μ of the reservoir).

3.2. Kondo Effect

By rearranging Eq. 3.11 into an integral form

$$\Delta S_{\epsilon_1 \rightarrow \epsilon_2} = - \int_{\epsilon_1}^{\epsilon_2} \frac{dN_d(\epsilon)}{dT} d\epsilon, \quad (3.12)$$

we obtain an equation that allows us to calculate the entropy change of the full system ΔS as we change the energy of the QD whilst monitoring the thermal response of the QDs occupation. It is important to note that N_d is not limited to integer values as it represents the time-average occupation $\langle N_d \rangle$ of the QD in equilibrium.

In practice, we approximate dN_d/dT by the discrete derivative¹¹

$$\frac{dN(\epsilon)}{dT} \approx \frac{N(\epsilon)|_{T_2} - N(\epsilon)|_{T_1}}{T_2 - T_1} \quad (3.13)$$

giving the exact measured function as follows:

$$\Delta S_{\epsilon_1 \rightarrow \epsilon_2} \approx \frac{\int_{\epsilon_1}^{\epsilon_2} N(\epsilon) d\epsilon|_{T_2} - \int_{\epsilon_1}^{\epsilon_2} N(\epsilon) d\epsilon|_{T_1}}{T_2 - T_1}. \quad (3.14)$$

Overall, the approach delineated by the derivation in this section requires no assumptions regarding the nature of the system's quantum state and is therefore generally applicable; additionally, it depends only on parameters that naturally map to controllable or measurable quantities (described further in Chapter 4).

3.2 Kondo Effect

Given that an eventual goal of the work discussed in this thesis is to use the proposed entropy measurement described in Section 3.1 to measure the entropy change associated with the formation of Kondo correlations, here I will provide a background of the Kondo effect and discuss some of the existing measurements in mesoscopic devices. The Kondo effect is a remarkable many-body quantum phenomenon that arises from the interaction between

¹¹An alternative measurement approach using a lock-in amplifier could be used to measure dN_d/dT more directly, but as mentioned in Chapter 4, this alternative approach is susceptible to additional sources of error.

3.2. Kondo Effect

a localized magnetic impurity and the conduction electrons in a metal or a semiconducting host.¹² The effect was first observed – long before it gained its name – as an anomalous increase in the electrical resistivity of a gold wire at very low temperature, contrary to the expected decrease due to reduced phonon scattering [95]. In subsequent years, the effect was observed in a wide range of metals [96]–[101], but despite much attention from experimentalists and theorists alike [102]–[104], the effect went without a complete explanation for 30 years. Then, in 1964, Jun Kondo provided a theoretical explanation of the effect, and the phenomenon gained its name: the Kondo effect [105].

3.2.1 Overview of the Kondo effect

The underlying mechanism of the Kondo effect involves the formation of a correlated state between an impurity and a cloud of electrons that surrounds it. This state results in a scattering rate of conduction electrons that has a strong dependence on the energy difference between the incoming conduction electron and the Fermi level (that leads to the anomalous low T behaviour). The fact that the low-temperature resistance minimum was observed even in very dilute alloys [106] led Kondo to explore the possibility that individual magnetic impurities may exhibit anti-ferromagnetic coupling with the conduction electrons of the host metal rather than a correlation between the localized spins of the impurities themselves [107].

Where earlier calculations of the scattering probability of conduction electrons with the magnetic impurities had been calculated to the first Born approximation [108] (i.e. assuming that interactions can be treated as single scattering events), Kondo realised that calculation to the second Born approximation (i.e. including second-order scattering events) introduced a temperature-dependent term that explained the resistance minimum [105]. Typically the term that arises from the second Born approximation is much smaller than that of the first, however, Kondo found that, due to the dynam-

¹²While we focus on the Kondo impurity model, which deals with isolated magnetic impurities, it is worth noting there exists a Kondo lattice model that describes the collective behavior of periodic arrays of magnetic impurities in a metal [94].

3.2. Kondo Effect

ical nature of the impurity spin system, the second term involves a factor that has a singular dependence on the energy of the initial state relative to the Fermi energy and that results in a large contribution at low T (i.e. when the Fermi surface is sharp). An example of a second-order scattering event in the context of a QD is described in Section 3.2.2.

Overall, the formation of a Kondo correlation can be understood intuitively by considering a simplified scenario where the spin of a magnetic impurity S interacts with a single spinful conduction electron S' [109]. In the case that there is no exchange interaction between the spins ($J = 0$), the ground state of the impurity is a doublet. However, with any amount of anti-ferromagnetic coupling $J < 0$, even if it is very weak, the ground state becomes a singlet between the impurity and conduction electron, separated from the excited triplet state by J (which can be considered the binding energy). This potential to lift the degeneracy of the impurity state is what underpins the Kondo effect [109]. Note that this simple picture (considering the interaction of the impurity with only a single conduction electron) is analogous to the mechanism of the formation of a Kondo-correlated state, but it does not yet explain the resistivity increase that results.

In reality, the impurity does not couple to a single conduction electron: because the conduction electrons are freely moving in space, it is hard for the impurity to “capture” a single electron [109]. Instead, through the coherent superposition of many such interactions, it couples to a local spin density s from the surrounding continuum of conduction electrons [110]. The binding energy between the impurity S and the spin density s is no longer described by J ; instead, the Kondo temperature T_K is introduced. It is T_K that sets the energy scale for the Kondo-correlated many-body spin singlet state. At low enough temperature ($T < T_K$), this correlated state between the impurity and many surrounding electrons effectively increases the scattering cross-section of the impurity, thus increasing the resistance of the bulk material [107].

3.2. Kondo Effect

3.2.2 Kondo effect in mesoscopics

To study the Kondo effect in mesoscopic devices, one can mimic the magnetic impurity with a quantum dot that has a net spin. The 2DEG that is coupled to the QD is equivalent to the conduction electrons in a bulk material; by measuring the conductance through such a QD (in comparison to measuring the resistance of a bulk material), one can infer the formation of a Kondo-correlated state, as is described in more detail below.

As discussed in Chapter 2, a quantum dot through which conductance is measured is often called a single electron transistor (SET) and therefore the terms are often used interchangeably. A small ($< \sim 100$ electrons [111]) QD can be tuned to exhibit the Kondo effect and was first demonstrated by Goldhaber Gordon et al. [112], [113] (shortly followed by two other groups [114], [115]) in 1998. For a QD to exhibit Kondo correlations, two requirements must be met via gate tuning: First, the QD must be tuned to have a net spin. In a small quantum dot, a simple way that this can be achieved is by starting with a very negative potential on the plunger gate such that the dot is unoccupied, then reducing the negative potential until there is one (or any odd number) of electrons in the dot. ¹³

Second, the QD must have a reasonably strong coupling Γ to the leads. The strength of the coupling Γ has a similar effect to varying the strength of the exchange interaction J between the conduction electrons and the magnetic impurities in a bulk material – a quantity that in bulk materials is largely fixed by the material properties. In a mesoscopic device, however, this coupling can be tuned over several orders of magnitude by varying the potential on the two gates that control the tunnel barriers on either side of the QD, and as a result, T_K of the system can be varied significantly.

With a QD tuned to odd occupation (N) and with reasonably strong coupling to the leads, the conductance through the QD becomes very sensitive to the presence or absence of the Kondo effect. As discussed in Section 2.3, with the QD energy level $E(N) = \epsilon$ below the Fermi energies of the leads μ

¹³Many published measurements involving Kondo correlations utilize QDs with 10s of electrons [111]–[115] and infer the odd/even occupations from the behaviour of the system.

3.2. Kondo Effect

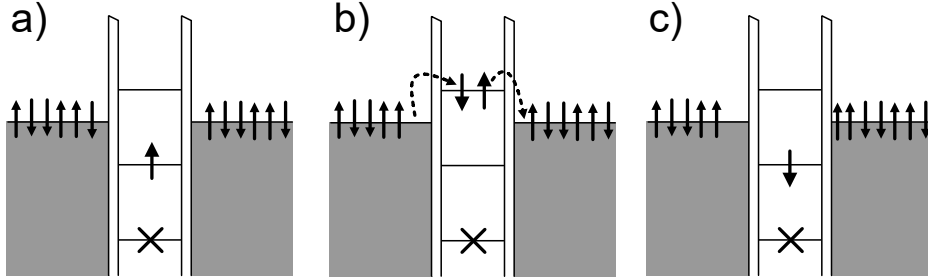


Figure 3.1: Schematic of a 2nd order tunnelling process illustrating a spin flip of the unpaired electron in the QD. Each panel depicts a QD coupled to two leads where the E_C separated energy levels of the QD straddle the Fermi energy of the leads. Crosses represent that all lower energy levels of the QD are filled with no net spin, leaving a single energy level below the Fermi energy that can be filled by a single spin up or down electron. (a) Initially, the QD has a net spin-up. (b) An intermediate state in which a spin-down electron has tunnelled into the QD from the left lead. Within a short time, a spin-up electron on the QD tunnels to the right lead. (c) The final state of the system after a single 2nd order tunnelling process where the QD now has a net spin-down.

(specifically, $\mu - \epsilon > k_B T$), and $E(N + 1) = \epsilon + E_C$ above that of the leads ($\epsilon + E_C - \mu > k_B T$), one would expect the QD to be insulating since first-order tunnelling processes through the QD are blocked. However, if we now consider second-order tunnelling processes (analogous to the second-order scattering events Kondo considered in bulk materials), we find that there is a mechanism for electrons to pass through the QD. Much like the bulk case, this involves the dynamical nature of the spin state of the QD.

To understand these second-order tunnelling processes, let us consider the example shown in Fig. 3.1 that illustrates one possible process. We start with an initial state (Fig. 3.1a) where the QD has a well-defined occupation (N and $N + 1$ levels are far from the Fermi level of the leads), with a single unpaired spin-up electron occupying the N^{th} level and an abundance of electrons in each lead. Fig. 3.1b depicts an intermediate state in which a

3.2. Kondo Effect

spin-down electron enters the $N + 1^{\text{th}}$ level from the left lead.¹⁴ Although this is not classically allowed due to the energy level of the $N + 1^{\text{th}}$ state being well above the Fermi energy, Heisenberg's energy-time uncertainty principle allows this as an intermediate state, if, within a short time, an electron also tunnels out of the QD. Because the electron that tunnels out of the QD need not be the same electron that tunnels in, the spin state of the QD can be flipped, as shown in Fig. 3.1c (where additionally, one electron has moved from the left lead to the right). Note that Fig. 3.1 depicts only one of many possible virtual processes. In general, the intermediate state can involve the QD first gaining (or losing) an electron from (to) either lead, followed by losing (gaining) an electron to (from) either lead. Any time an electron comes from a lead, it can have either spin,¹⁵ meaning that not all of these processes necessarily involve spin flips. However, just as in the bulk case, it is the processes that involve spin-flips that contribute to the Kondo correlated state (because the operators involved in the spin-flip processes do not commute [105]).

In contrast to the bulk case, where the correlated Kondo states contribute to an increased resistivity of the material, in a QD the opposite behaviour is observed: the conductance through the QD increases. The increase in conductance is a direct consequence of the fact that the correlated state that forms in the case of a QD, involves electrons in both leads (the QD naturally exhibits anti-ferromagnetic coupling with electrons in both leads). This correlation across leads effectively results in the QD becoming transparent, and thus the conductance through the system increases.

Figure 3.2 shows a schematic of a QD used to measure the enhanced conductance that results from Kondo correlations. In this setup, a gate positioned directly over the QD modulates its energy. As the gate potential shifts positively, it becomes energetically favourable for the occupation of

¹⁴Both electrons are shown at the higher energy level to emphasize that it is the energy of the QD that is temporarily above the Fermi energy; the electrons themselves are not bound to specific energy levels.

¹⁵Of course, the Pauli exclusion principle applies in the QD; however, the orbital level spacing is typically a fraction of the charging energy, so an electron with the same spin could enter with an intermediate energy of $\epsilon + E_C + \Delta$.

3.2. Kondo Effect

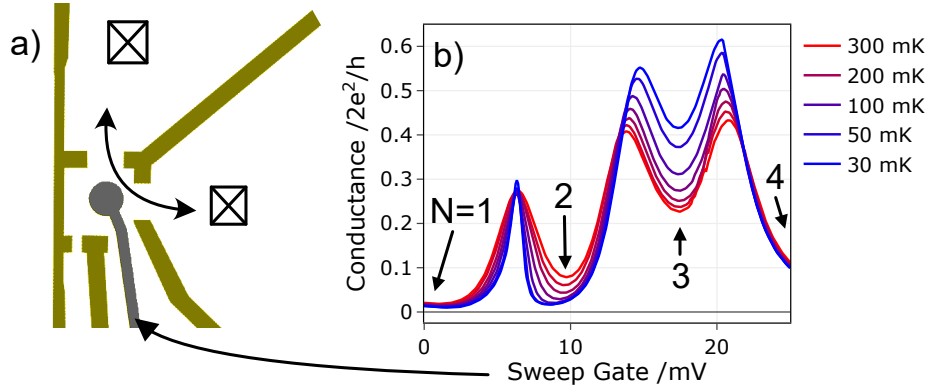


Figure 3.2: (a) A schematic of a QD with an “accumulation” sweep gate in grey to distinguish it from the regular gates in gold. Crossed boxes represent ohmic contacts. (b) Conductance through the QD vs. sweep gate voltage measured with close to zero bias (1 μV) for electron temperatures ranging 30 to 300 mK. QD occupation for each Coulomb valley is indicated. Notably, conductance increases with decreasing temperature for the Coulomb valley where $N = 3$ due to the Kondo effect while the conductance where $N = 2$ falls with decreasing temperature as expected in the Coulomb valley.

the QD to increase. Specifically, the conductance peaks observed at 7 and 13 mV in Fig. 3.2b approximately align with the QD energy states where the dot occupation transitions between 1 to 2 and 2 to 3 electrons, respectively. The conductance measurements are obtained by using a lock-in amplifier to apply a small ($\sim 1 \mu\text{V}$) AC bias, measuring the resulting current oscillations at the same frequency. The measurement is repeated at varying cryostat temperatures with corresponding electron temperatures in the range 30 to 300 mK. Notably, for the Coulomb valley near 18 mV, the conductance increases as a function of decreasing temperature indicating the formation of a Kondo-correlated state between the net spin of the QD and the conduction electrons in the two leads. In fact, when the conductance is measured carefully [111], [113], [114], [116]–[121], it is possible to observe $\log(T)$ temperature dependence of the enhanced conductance that results from Kondo correlations [122]–[124]. This behaviour mirrors the resistance characteristics seen in the bulk Kondo effect.

3.2. Kondo Effect

It is worth noting that the enhanced conductance due to the presence of the Kondo effect in a QD is generally observed when there is close to zero source-drain bias (V_{SD}) applied (in the absence of magnetic field). The enhanced conductance is typically a zero bias effect because the Kondo-correlations lead to a peak in the density of states (DOS) on the impurity site at the Fermi level [123], [124]. While this DOS peak is not directly probed by resistivity measurements in metals, it is exactly what is probed by conductance measurements across a QD. With significant bias across the QD, the Kondo correlations are suppressed due to dissipative transitions in which electrons are transferred from the higher energy lead to the lower one [123], [124] which eventually results in the complete loss of the coherence of the Kondo correlation [125], [126]. Although not a focus in this thesis, there does exist an intermediate regime in which a small but non-zero applied bias ($V_{SD} \lesssim 20k_B T_K$ [127]) results in a splitting of the enhanced DOS into two peaks, representing an increased density of states at the chemical potential of each lead independently [123], [124], [128], [129]. Observations of this behaviour have been achieved in several ways: by adding a third coupling to the QD that acts as a probe for the resonances established by the first two [127], by replacing one lead with a coupling to the middle of biased quasi-ballistic nanowire that itself has a double-step Fermi distribution [130], or by applying a small in-plane magnetic field ($g\mu_B B < k_B T_K$ [107]) that is equal to the V_{SD} bias [131], [132]. (The induced Zeeman splitting of the QD spin states also splits the Kondo resonance resulting in enhanced conductance when bias and field splittings align).

In mesoscopic devices, the Kondo effect can be categorized into three regimes: the Kondo regime, mixed-valence regime, and empty (or full) orbital regime. As described in Ref. [113], these regimes can be parameterized by $\tilde{\epsilon}_0 = \epsilon_0/\Gamma$, where ϵ_0 represents the depth of the odd occupation QD energy level below E_F , and Γ is the coupling strength between the QD and the reservoir. With this notation, the Kondo regime (resembling the bulk case) is characterized by $\tilde{\epsilon}_0 \ll -0.5$, corresponding to a situation in which the QD predominantly exhibits a net spin due to the ϵ_0 energy level being mostly or fully occupied (the Coulomb valley in Fig. 3.2b). This is

3.2. Kondo Effect

the most commonly investigated regime, as this is where the Kondo effect has the most pronounced impact on the behaviour of the system, assuming $T_{\text{sys}} < T_K$. Then, there is the mixed-valence regime, observed when $-0.5 \lesssim \tilde{\epsilon}_0 \lesssim 0$. In this regime, the occupation of the QD fluctuates significantly but still mainly exhibits a net spin. Kondo-physics remains present, but the behaviour changes; for example, conductance enhancement becomes less pronounced, but the Kondo temperature increases significantly [113]. Notably, the mixed valence regime is the focal point of the measurements discussed in Chapter 6. Finally, the empty orbital regime comes into play when $\tilde{\epsilon}_0 \gtrsim 0$. In this case, the ϵ_0 energy level is mostly unoccupied: the QD is mostly in a state of even occupation with no net spin. However, the QD does still exhibit a net spin occasionally, thus Kondo-physics is not entirely absent but has a greatly diminished impact on the behaviour of the system.

While conductance measurements of the Kondo effect in mesoscopic systems have been measured in many experiments,¹⁶ an eventual goal of the work presented in this thesis is to measure the formation of Kondo correlations via a fundamentally different approach. Instead of observing the effect of Kondo correlations on the conductance of the system, we aim to directly probe the entropy change of the system upon the formation of Kondo correlations (Chapters 6 and 7). In contrast to the observation of an enhanced zero bias conduction peak, we intend to observe the change of entropy of the system from a spin-degenerate QD in the absence of Kondo correlations ($k_B \ln(2)$) to a system in which the ground state is that of a single Kondo correlated state ($k_B \ln(1) = 0$). In other words, we are interested in the change in entropy of the QD-lead system as we tune from a regime where $T \gtrsim T_K$ to $T \ll T_K$ (either by changing the temperature T or by tuning parameters of the system that affect T_K).

¹⁶A subset of which include Refs. [48], [111]–[121], [127], [130]–[139].

3.3 Numerical Renormalization Group (NRG) Calculations

For the measurements discussed in this thesis that involve strong coupling between a QD and a reservoir of electrons, the systems cannot be modelled analytically. Instead, we compare to numerical simulations generated by our theory collaborators (Yigal Meir, Yaakov Kleeorin, and Andrew Mitchell) using flexible density matrix numerical renormalization group (DM-NRG) code [140], [141] on the standard single impurity Anderson model. The single impurity Anderson model is the Hamiltonian that describes a single magnetic impurity, with discrete energy levels, coupled to a sea of non-interacting conduction electrons [142].

NRG is a method that was initially developed in the mid-1970s [143], and it has proved to be an incredibly powerful tool for the study of quantum impurity systems (open quantum systems with infinite thermal reservoirs) such as Kondo problem [143]. The method is generally suitable for such systems in which a small system with a few interacting degrees of freedom (the impurity) is coupled to a large system with many (non-interacting) degrees of freedom [144] (such as the reservoir of electrons in a 2DEG lead). While the calculations themselves are not a primary focus of this thesis, a rough understanding of the NRG method helps elucidate the theoretical calculations with which our experimental measurements are compared.

A challenge of investigating quantum impurity systems theoretically is the requirement of non-perturbative calculations to be made for interacting many-body systems with a continuum of excitations covering a wide range of energies [144]. For such problems with a continuous spectrum of energies, one can employ the renormalization group approach to investigate the system.

Renormalization group (RG) theory is a mathematical framework in theoretical physics that facilitates the systematic investigation of problems that involve a statistical continuum limit [143]. In particular, the NRG method is suitable due to this specific approach being non-perturbative in all system parameters (in contrast to most RG methods) at the cost of having

3.3. Numerical Renormalization Group (NRG) Calculations

to be performed numerically [144]. In fact, it is one of the most powerful non-perturbative methods available today [145].

This general overview of the NRG approach is described in Refs. [143], [144] as:

- Segmentation of the energy range of the reservoir’s spectral function into logarithmically sized intervals.
- Transformation of the continuous spectrum into a discrete set of states (logarithmic discretization). The continuous spectrum in each interval is replaced by a single pole at the average energy with the same total weight, resulting in a discretized spectrum that has poles at exponentially reducing energies (with exponentially reducing weight) approaching the Fermi energy.
- Mapping of the discretized states onto a semi-infinite chain where the impurity represents the first site in the chain.
- Iterative diagonalization of this chain, starting from the impurity site and successively adding degrees of freedom, keeping only a fraction of the lowest-lying many-particle states each time, obtaining a new effective Hamiltonian at each step.
- Further analysis of the energies and matrix elements calculated during the iterative diagonalization.

Effectively, the approach hinges on the physical idea that the energy (or length etc.) scales are locally coupled [143]. This implies that the behaviours at a particular point on the scale are most strongly affected by nearby points on that scale. This physical assumption allows breaking the problem into smaller chunks that form a cascade, where an important feature of this cascade is that the behaviour of each chunk is similar as a result of the lack of a characteristic scale [143].

The lack of characteristic scale means that, in the iterative process of diagonalization, one can reach a “fixed point” where the effective Hamiltonian after each step becomes self-similar. Then, by repeatedly carrying out this

3.3. Numerical Renormalization Group (NRG) Calculations

iterative process with varying initial conditions, one can determine so-called amplification and de-amplification factors that in turn determine which parameters of the initial Hamiltonian are “relevant” or “irrelevant” [143].

These amplification factors are the second key feature of the cascade picture, where small changes in a parameter at the small end of the cascade can result in either amplifying or de-amplifying behaviour as the cascade develops. For parameters whose effects amplify (a relevant variable), small changes in the small end of the scale can result in macroscopic changes at the large end of the scale, despite no assumption of a direct relationship between them, thus maintaining the ability of this approach to capture macroscopic effects that result from microscopic behaviours [143].

Overall, the NRG approach allows for non-perturbative simulations of complex systems that accurately capture the low-energy behaviour of the original systems. It can be used to make predictions for the entropy, conductance, and occupation (among other things) of the system being modelled over a wide energy scale, and is thus well-suited for simulating the mesoscopic quantum systems that are measured and discussed in this thesis.

Chapter 4

Proof of concept measurement (Single Isolated QD)

In this chapter, a demonstration of the new entropy measurement technique discussed in Section 3.1 is presented. This demonstration is analogous to that of Ref. [8] in that it is a demonstration of measuring the entropy change of a quantum dot upon the addition of a single spin-1/2 electron. However, in contrast to the previous work, the following demonstration is generalizable to more complex systems (as will be demonstrated in later chapters).

This chapter focuses on the technical details of the measurement protocol, along with a discussion of solutions to problems that were encountered in the development of this new technique that would likely be encountered by others attempting to replicate similar measurements. A large portion of the contents of this chapter are published in Ref. [146].

4.1 Introduction

As discussed in Section 3.1, we utilize Maxwell relations to measure S (or, more accurately, changes in S) by sensing changes in charge with temperature. This follows the work presented in Ref. [8] that used a charge-sensing approach to measure ΔS due to the addition of a single spin-1/2 electron in a lithographically defined quantum dot. Although the experiment in Ref. [8] served as a promising step toward a direct entropy measurement protocol

4.2. Device Design and Layout

based on charge sensing, the applicability was limited¹⁷ to simple systems for which the measurement of entropy holds little scientific value and allowed only the determination of entropy change caused by adding one full electron at a time. Additionally, the experimental method described in that work left room for artifacts in the measurement signal that could contaminate the determination of ΔS .

The goal of the work presented in this chapter is to outline the improvements made to the experimental approach in Ref. [8] that make it more robust at a technical level and applicable to a broader range of measurements. From the analytical side, the extraction of ΔS is based on the formulation of the Maxwell relation (Eq. 3.12 as derived in Section 3.1)

$$\Delta S_{\epsilon_1 \rightarrow \epsilon_2} = - \int_{\epsilon_1}^{\epsilon_2} \frac{dN(\epsilon)}{dT} d\epsilon, \quad (4.1)$$

where N and ϵ represent the occupation and energy of the quantum dot (QD) respectively, and T is the temperature of the electron reservoir. Equation 4.1 enables the determination of entropy (change) continuously as a function of gate voltages or other parameters that control ϵ . In the experiment, significant improvements to the thermal design and measurement protocol eliminate many sources of error. Beyond the description of the new experimental protocol, we describe common challenges and possible strategies to overcome them that other groups may encounter in attempting this type of measurement.

4.2 Device Design and Layout

A circuit designed to measure the entropy of a QD using $\partial S/\partial\epsilon = -\partial N/\partial T$ must have three elements: a QD with tuneable energy ϵ that is coupled to an electron reservoir, the ability to change the temperature of this reservoir, and a charge sensor to detect the occupation of the QD. At the outset, it is important to note the use of ϵ rather than the chemical potential of the

¹⁷This is primarily due to the specific implementation of the Maxwell relation in that initial work.

4.2. Device Design and Layout

thermodynamic reservoir μ that is more commonly referenced in relation to Maxwell equations. This is a result of the difficulty in controlling μ experimentally [83]. Instead, we tune the energy of the QD level ϵ . In practice, it is the difference between μ and ϵ that controls when electrons will enter the dot, so tuning ϵ has a similar effect to tuning μ .

Figure 4.1 shows an example of a circuit with the three elements listed above. The device was fabricated in a GaAs/AlGaAs heterostructure that hosts a 2D electron gas (2DEG) as described in Chapter 2. The electrostatic gates were fabricated with two stages of electron beam lithography followed by electron beam evaporation: a fine step for the inner parts, and a coarse step for the outer parts of the gates. In the fine step, 2/12 nm of Pd/Au were deposited. In the coarse step, 10/150 nm of Ti/Au were deposited. Measurements were carried out in a dilution refrigerator at temperatures ranging from 30 mK up to 500 mK. Electron temperatures below 30 mK were not attainable in our cryostat, and temperatures higher than 500 mK brought in sources of S unrelated to those of interest in the measurement. Electron temperatures were determined using the procedures explained in Section 2.5.

The QD itself was defined following standard design guidelines developed through two decades of few-electron dot measurements across the mesoscopics community; see, for example, Refs. [51], [54], [147]. The gates immediately surrounding the dot were cooled down with a +400 mV bias so that when cold, the 2DEG under the gates was depleted of carriers with no voltage applied. The resulting QD could be readily tuned to an occupation of $0 \rightarrow 5$ electrons using the surrounding gates, with the voltage V_P applied to the plunger gate, as shown in Fig. 4.1, dedicated to the coarse tuning of the dot occupation.

One of the advantages of our measurement protocol, which relies on charge-sensing measurements rather than conductance, is its impact on device design: the QD only requires a single tunnel barrier to a reservoir. Furthermore, as a charge-sensing approach, the measurement is relatively insensitive to the precise strength of coupling between the QD and reservoir. However, some factors are especially important for the entropy measurement

4.2. Device Design and Layout

that may not be as relevant in other experiments. For example, tuning of the QD energy level ϵ is central to this technique, and this tuning must be accomplished without changing other dot parameters significantly. For this reason, the design includes a gate extending into the middle of the dot, labelled V_D in Fig. 4.1, with a very large electrostatic coupling to the QD electron wavefunction: the lever arm of this gate (the ratio of the change in QD energy to the gate voltage applied) was typically 0.2 eV/V for this gate, compared with 0.04 eV/V or less for V_P .

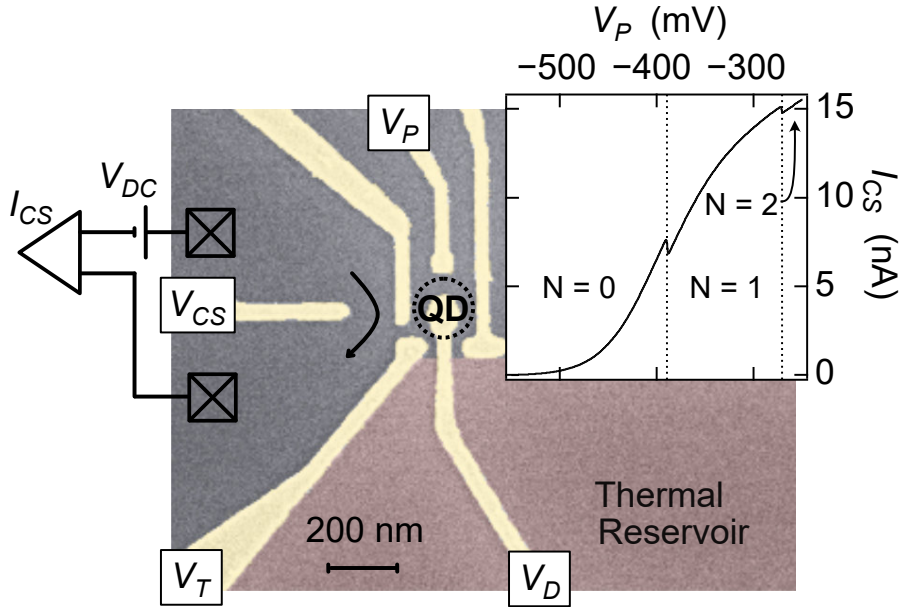


Figure 4.1: (main panel) False-coloured scanning electron micrograph (SEM) of the key parts of the entropy sensor. Electrostatic gates (gold) define the circuit in a 2D electron gas (2DEG). The thermal electron reservoir (red) can be rapidly heated by driving current through quantum point contacts (QPCs) far away. (inset) Current through the charge sensor, I_{CS} , for a wide sweep of the coarse plunger gate, V_P , demonstrating the alignment of the $0 \rightarrow 1$ transition at the steepest part of the trace to maximize sensitivity.

The quantum point contact (QPC) operated as a charge sensor was formed by the three leftmost gates in Fig. 4.1, and used to detect the oc-

4.2. Device Design and Layout

cupation of the QD [47], [48], [148]. A DC bias, typically between 50 and 300 μV , was applied across the charge sensor, with the resulting current I_{CS} recorded using a current-voltage converter (10^8 A/V, 1 kHz bandwidth set by a two-stage low-pass filter). For the measurement protocol described here, real-time monitoring of the current is important, so the output of the current preamplifier was fed into an analog-digital converter with a 2.5 kHz sample rate.

V_{CS} was tuned to maximize the charge sensor sensitivity to charge in the QD. The inset to Figure 4.1 shows $0 \rightarrow 1 \rightarrow 2$ electron transitions for the QD, in this case, driven by V_P , with the $0 \rightarrow 1$ transition tuned to the steepest slope below the 1st conductance plateau. The relatively large cross capacitance between V_P and the charge sensor is apparent in the data in Fig. 4.1 inset: just 200 mV applied to V_P can tune the QPC from pinch-off to nearly full transmission. This highlights the importance of tuning dot occupation with V_D during the entropy measurement.

The charge sensor sensitivity could also be increased by tuning the gates around the dot to bring the center of the electron wavefunction as close as possible to the charge sensor: in some cases, we were able to achieve a 10% change in charge sensor transmission due to the addition of an electron to the QD, using this gate geometry. We point out, however, that increasing the QD–charge sensor coupling has both advantages and disadvantages. Stronger coupling reduces the bias that must be applied to the charge sensor for the same signal-to-noise. At the same time, stronger coupling shifts the charge detection process farther from the weak measurement limit that may be desirable from the point of view of back-action on the quantum system under study [149]–[151]. Which of these factors is more important will, in general, be different from experiment to experiment.

The coupling of the QD to the heated electron reservoir was controlled by V_T . For simplicity, the measurements presented here are in the weak coupling limit (very negative V_T), where the broadening of the QD energy levels due to the coupling with the reservoir, Γ , is much less than that of thermal broadening ($\Gamma \ll k_B T$); however, measurements using this technique are also possible in the strongly coupled regime (as discussed in Chapter 6).

4.3. Measurement Protocol

For the measurements presented here, Γ is estimated to be of the order $0.001 k_B T$ (extrapolated from measurements in the strong coupling regime where Γ measurably broadens the charge transition [152]). The limit on arbitrarily weak coupling arises from the requirement that the tunnelling rate between the QD and the reservoir must be much faster than the measurement rate (the inverse of the time spent sitting at each setting of ϵ during which an average N was recorded). From a thermodynamic perspective, this restriction ensures that the QD can transition between all available microstates within the measurement time.

4.3 Measurement Protocol

The measurement of $\partial N/\partial T$ that is central to Eq. 4.1 was carried out by evaluating the discrete derivative $\Delta N/\Delta T$ (Eq. 3.13), using the charge sensor to monitor the change in N between two nearby temperatures $\Delta N = (N(T + \Delta T) - N(T))$. The choice to measure at two particular values of T , rather than the simpler approach of oscillating T (approximately) sinusoidally at frequency f_T , then locking into variations in N at f_T , was found to be important to the quantitative determination of ∂T in Eq. 4.1 with better than 10%-20% error, and was also helpful in troubleshooting spurious changes in the dot potentials that could appear when attempting to change only T .

It is the response of N to temperature alone, with all other parameters (such as the chemical potential μ and dot energy ϵ) constant, that contains information about the entropy of the system. This requirement, for identical μ and ϵ between the two temperatures, turns out to pose a significant experimental challenge. In practice, any changes $\delta\mu$ in the thermal reservoir or $\delta\epsilon$ in the dot energy between the measurements at $T + \Delta T$ and T will introduce inaccuracy in the entropy measurement by an amount of order $\delta\mu/(k_B\Delta T)$ or $\delta\epsilon/(k_B\Delta T)$, respectively. For measurements below 100 mK, where ΔT is less than a few tens of mK, this restricts $\delta\mu$ and $\delta\epsilon$ between the two temperatures to be much less than 1 μeV for an accurate determination of ΔS . There are both intrinsic and extrinsic factors that must be taken

4.3. Measurement Protocol

into account to keep μ and ϵ constant to such a high degree.

Quantum dots fabricated in GaAs/AlGaAs heterostructures experience intrinsic, albeit small, electrostatic fluctuations due to nearby charge motion in the dopant layer of the heterostructure, resulting in noise in the QD energy ϵ with a frequency spectrum typically between $1/f$ and $1/f^2$ [19], [23]. It is therefore crucial that the measurements $N(T + \Delta T)$ and $N(T)$ be carried out as close to each other in time as possible, protecting the measurement from noise in the low- f limit. The requirement to alternate rapidly between hot and cold reservoir temperatures mandates that the temperature change is accomplished locally on the chip, rather than by changing the temperature T of the entire cryostat. For this reason, and to minimize the heat capacity of the thermal system, Joule heating due to a bias current I_H was used to raise the electron temperature T_e of the thermal reservoir adjacent to the QD (Fig. 4.1) above the sample (chip) temperature T : $T_e = T$ when $I_H = 0$ and $T_e = T + \Delta T$ at finite I_H .

Driving I_H directly into the thermal reservoir will generally change its potential, however. Since the occupation N of the QD depends on the difference between the chemical potential of the reservoir μ and dot energy ϵ , this direct effect of I_H must be avoided. At the same time, the advantage of very local heating must be balanced by the requirement for full thermal equilibration of charge carriers in the reservoir, in contrast to the non-equilibrium distribution that is expected when injecting carriers at high bias through a mesoscopic circuit.

A two-chamber heater was used to ensure a thermalized electron reservoir with a μ that did not change when the Joule heating current was applied (Fig. 4.2a): I_H was sourced through QPC1 and drained through QPC2 to heat the first chamber directly, whereas the second chamber (the thermal reservoir immediately adjacent to the QD) was heated indirectly by electrons diffusing from the first chamber through QPC3. Cooling of the reservoirs occurred via electron-phonon coupling (especially at higher temperatures) and by diffusion through QPC1, QPC2, and QPC4 to the 2DEG regions connected to ohmic contacts, which remain at the chip temperature due to their large volume and therefore strong electron-phonon equilibration. For

4.3. Measurement Protocol

most experiments, QPCs 1, 2, and 3 were set at their $2e^2/h$ conductance plateau, while QPC4 was set at $6e^2/h$.

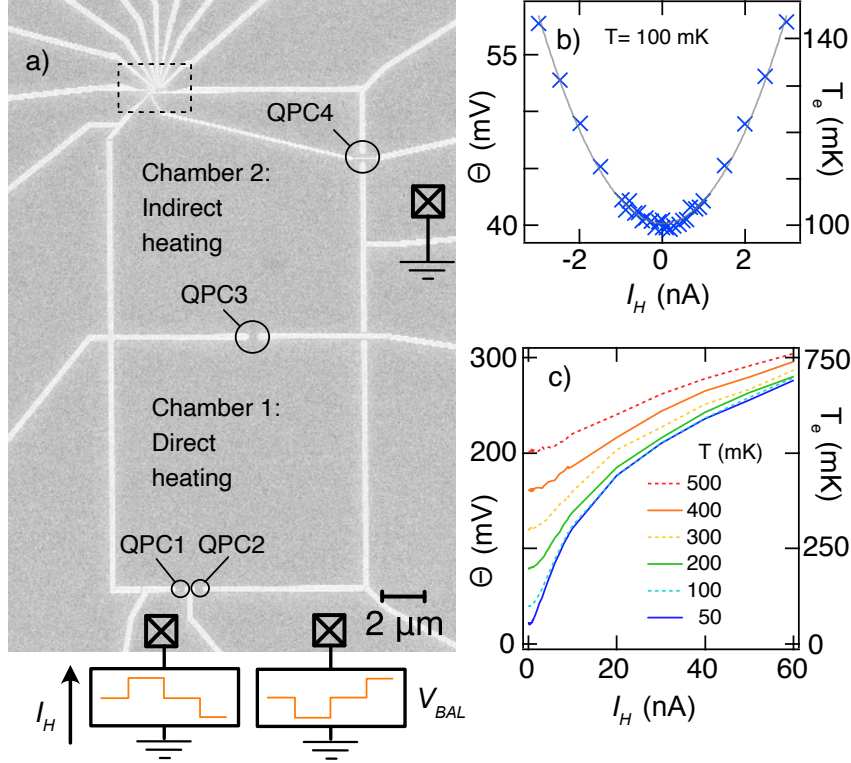


Figure 4.2: (a) SEM micrograph of the full measurement device showing the large ($10\ \mu\text{m}$ square) chambers used for electron thermalization, QPCs 1 and 2 through which Joule heating current I_H flowed, and QPCs 3 and 4 through which heat diffused but no net current flowed. The dashed rectangle in the upper left is the region shown in Fig. 4.1a, including QD and charge sensor. (b) Crosses: broadening of the charge transition (Θ , left axis), converted to electron temperature (T_e , right axis), increases above the sample temperature, $T_s = 100\ \text{mK}$, due to I_H driven through QPCs 1 and 2. Solid line: quadratic fit to $|I_H| < 1\ \text{nA}$ data, with deviations seen at higher $|I_H|$. (c) Extension of panel b to higher I_H and for a range of different sample temperatures. Sub-linear behaviour at very large I_H reflects electron-phonon cooling at higher temperatures.

One advantage of using quasi-enclosed chambers for heating is the rel-

4.3. Measurement Protocol

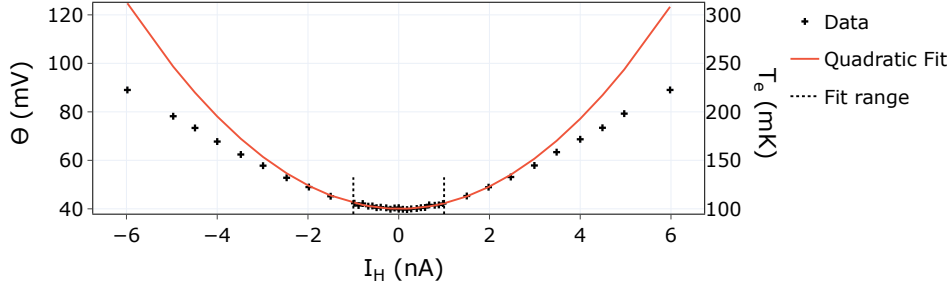


Figure 4.3: Electron temperature vs I_H , with an extended I_H range compared to Fig. 4.2b, to emphasise the non-quadratic response for larger $|I_H|$. The solid line represents the same quadratic fit ($I_H < 1$ nA).

atively low values of I_H required to achieve a significant temperature rise. Figure 4.2b shows that T_e of chamber 2, measured via the broadening of a weakly coupled charge transition in the QD, can be increased from a sample temperature $T = 100$ mK to $T + \Delta T \sim 130$ mK with I_H less than 2.5 nA. At a quantitative level, of course, the temperature rise for a given current depends on the settings of all four QPCs.

The electron temperature is approximately quadratic in I_H for small heating currents, as might be expected from Joule heating power $P \propto I_H^2$, but already by $\Delta T \sim 20$ mK small deviations are visible in Fig. 4.2b, where $T = 100$ mK. Figure 4.3 depicts the behaviour over a slightly wider range of I_H , more clearly showing the non-quadratic response of electron temperature to I_H . The deviations become more extreme at higher I_H or lower chip temperature T . Non-quadratic behaviour results from the temperature dependence of the thermal conductivity κ between the reservoir electrons and the cold thermal ground, whether it be via electron–phonon coupling to the chip’s lattice ($\kappa_{e-ph} \propto T^{3-4}$ expected) or Wiedemann–Franz cooling¹⁸ ($\kappa_{WF} \propto T$ expected) to the cold reservoirs connected to ohmic con-

¹⁸The Wiedemann–Franz law states that the ratio of the electronic contribution of the thermal conductivity κ to the electrical conductivity σ is equal to the Lorentz number L times temperature T :

$$\frac{\kappa}{\sigma} = LT$$

4.3. Measurement Protocol

tacts [153]. Figure 4.2c illustrates the extreme deviation from quadratic behaviour for large I_H , corresponding to large ΔT . The sub-linear line-shape of $T_e(I_H)$ at the highest currents demonstrates that phonon cooling has become dominant.

The potential of chamber 2 (Fig. 4.2a) was held constant by biasing I_H through QPC1 while applying a balancing voltage V_{BAL} behind QPC2. V_{BAL} was tuned such that the potential in chamber 2, when sensed directly by the QD, remained constant. The inverse signs of I_H into QPC1 and V_{BAL} behind QPC2 are illustrated schematically at the bottom of Fig. 4.2a. To alternate the temperature while ensuring that μ stays constant, opposing three-level square waves were created by two channels of a 2.5 kHz digital-analog converter to generate I_H and V_{BAL} . The top row of Fig. 4.4 shows the square wave driving I_H , with an inverse wave setting V_{BAL} . The square wave has four 20 ms segments: two segments heated with equal magnitude but opposite sign ($I_H = \pm 3$ nA in this case), separated by two segments at $I_H = 0$. Only after confirming the expected response in all four segments is it possible to conclude that the heating process has not affected μ .

Figures 4.4a–d show the response of the charge sensor (I_{CS}) to the square wave, at the four positions along the charge transition indicated by arrows in Fig. 4.4e. Before and after the transition (Fig. 4.4a,d) there is no effect of I_H . Checking these “control” positions is important to confirm the absence of spurious coupling between I_H and the charge sensor, such as capacitive coupling between the wires carrying I_H and those carrying I_{CS} , or between the current path of I_H and the charge sensor itself. Before the midpoint of the transition (Fig. 4.4b), Joule heating of chamber 2 leads to a drop in I_{CS} , reflecting extra charge in the dot and therefore positive dN/dT (Eq. 4.1). Within the noise of this measurement, there is no difference between positive and negative I_H . This confirms that first-order effects of I_H are strongly suppressed, for example by properly setting V_{BAL} . For $V_D \gtrsim 0.03$ mV, the Joule heating of chamber 2 leads to a rise in I_{CS} ; therefore, dN/dT becomes negative before returning to zero after the transition.

The raw data, $I_{CS}(t)$, are processed to determine a single value ΔI_{CS} for each V_D applied to the gate that tunes dot energy. This involves separating

4.3. Measurement Protocol

the data into two segments corresponding either to T or $T + \Delta T$. Before that is done, however, it is important to remove the time periods during which the measurement is settling to new parameter values. This settling time, on the order of a few milliseconds, is clearly visible in Fig. 4.4**b,c**. We note that the rate of settling is limited by the response of the cryostat wiring in our case; thermal equilibration times within the device are many orders of magnitude faster [71]. The two segments at T , or $T + \Delta T$, are then averaged to find $I_{CS}(T)$, or $I_{CS}(T + \Delta T)$. These values, determined at each V_D , are plotted in Fig. 4.4**e** in blue (T) and red ($T + \Delta T$), with the difference, ΔI_{CS} , in Fig. 4.4**f**.

$\Delta N/\Delta T$ is obtained from the ΔI_{CS} measurement using parameters obtained from the charge transition itself, $I_{CS}(V_D)$. Weakly coupled transitions are broadened by the Fermi–Dirac distribution in the reservoir and may be fit to [37], [58]

$$I_{CS}(V_D) = \frac{-I_e}{2} \tanh\left(\frac{V_D - V_0}{2\Theta}\right) + I'(V_D - V_0) + I_0, \quad (4.2)$$

where I_e quantifies the sensitivity of the charge sensor to the occupation of the QD, V_0 is the center of the charge transition, Θ represents the thermal broadening in equivalent gate voltage, I' quantifies the cross-capacitance between V_D and the charge sensor, and I_0 is the current through the charge sensor midway through the transition. Although the cross-capacitance is well approximated as a simple linear term for weakly coupled transitions, for more strongly coupled transitions, it may have different slopes on the $N = 0$ and $N = 1$ sides of the transition, which require more elaborate fitting.

4.3. Measurement Protocol

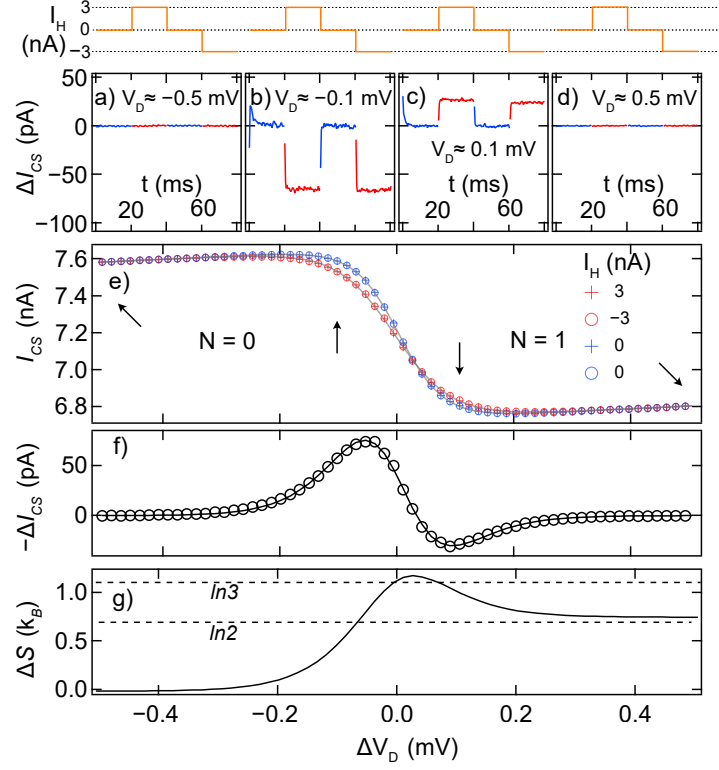


Figure 4.4: A step-by-step inspection of the analysis procedure that goes into an eventual calculation of ΔS . The fine-tuning plunger gate, V_D , is used to lower the energy of the QD level such that one electron enters from the thermal reservoir. (top) Schematic illustration of $I_H(t)$ through one complete 80 ms cycle. (a–d) Charge sensor current through the 80 ms cycle, calculated with respect to the unheated sections, at four locations on the $0 \rightarrow 1$ transition: $V_D = -0.5, -0.1, 0.1, 0.5$ mV. Data shown here are averaged over 1200 square wave cycles. Blue (red) indicates times at which the thermal reservoir is unheated (heated). The relaxation time of the measurement (~ 3 ms) is visible in panels **b** and **c**. (e) Charge sensor current separated into averages over the 4 parts of the square heating wave, where heating is applied with an alternating current direction ($I_H = 3, -3$ nA), with zero bias applied in between ($I_H = 0$). Fits to the average “cold” and “hot” data are shown in grey. (f) The difference in charge sensor current between the “cold” and “hot” traces. (g) $\Delta S(V_D)$ obtained by integration of ΔI_{CS} using Eq. 4.1. ΔT is 28.1 mK, equivalent to 0.011 mV when converted to effective gate voltage, determined from the difference in thermal broadening of heated and unheated I_{CS} .

4.3. Measurement Protocol

Of these parameters, I_e and Θ are crucial to the conversion between ΔI_{CS} and $\Delta N/\Delta T$. I_e is the difference in current through the charge sensor between the unoccupied ($N = 0$) and occupied ($N = 1$) states, and is therefore used to scale the charge sensor reading to $\Delta N = -\Delta I_{CS}/I_e$ (the minus sign appears because an increase in N causes a drop in I_{CS}). ΔT is determined from the difference in the broadening term, Θ , for heated and unheated transitions. This calculation is straightforward when the QD is in the weakly coupled limit, with the charge transition well modelled by Eq. 4.2. As determined by fits to Eq. 4.2, Θ will have units of gate voltage instead of energy, and the lever arm $\alpha \equiv \Delta\epsilon/\Delta V_D$ that converts changes in the gate voltage V_D to changes in the dot energy ϵ would be needed to convert Θ to $k_B T$. In practice, it is more convenient to perform the integral in Eq. 4.1 over the gate voltage V_D actually controlled in the measurement, rather than over the equivalent ϵ (in units of energy). Therefore, the denominator in the integrand $\Delta N/\Delta T$ is more conveniently expressed as $\Delta\Theta$ in units of equivalent V_D rather than ΔT in Kelvin. The ΔS obtained (Fig. 4.4g) by this approach is then in units of k_B . Following this procedure, the factor α cancels and need not be measured directly.

As described in Section 3.1, for a weakly coupled non-interacting QD, the entropy is well modelled by the classical Gibbs entropy (Eq. 3.2). For the measurements shown in Fig. 4.4, the QD starts in an unoccupied state ($S = k_B \ln(1) = 0$), corresponding to the example described in Section 3.1 where $\Delta S = S$ and the entropy of the system is expected to change from $0 \rightarrow k_B \ln(2)$ with a peak at $k_B \ln(3)$ at the point where the QD is both spin and charge degenerate. As V_D is made more positive, bringing ϵ towards μ , the average occupation of the QD begins to increase from zero at $V_D \sim -0.3$ mV, reaching $\langle N \rangle = 2/3$ (charge and spin degenerate) at $V_D \sim 0.025$ mV, and finally $N = 1$ at $V_D \sim 0.25$ mV.

The values $1.07 k_B \ln(3)$ and $1.07 k_B \ln(2)$ in Fig. 4.4g illustrate typical experimental errors resulting from the approach outlined in this work. It is more robust than the approach of Ref. [8] in the sense that this technique can be applied to arbitrarily complex systems without modification to the analysis procedure; however, it is susceptible to calibration errors, giving a

4.4. Common Problems

typical uncertainty of up to 10% for this method.

4.4 Common Problems

The rather complicated thermalization device design described in the previous section was arrived at after an initial round of experiments, e.g., Ref. [8], with a much simpler design. That design is illustrated in Fig. 4.5, with Joule heating through a single QPC directly across a channel from the QD to be measured. In addition to the more efficient heating in the present design ($\Delta T \sim 30$ mK at $T = 100$ mK requires 3 nA at 40 μ V bias compared to 8 nA at 160 μ V bias in Ref. [8]), Figures 4.5**b,c** illustrate two of the experimental artifacts that were introduced by the simpler design.

Figure 4.5**b** shows the effect of poor thermalization of the electrons due to I_H before they interact with the dot. Electrons (or holes) passing through the Joule heating QPC enter the reservoir (channel) with very high energy (160 μ eV in the example above) compared to the final temperature they will have after equilibration ($k_B \cdot 130$ mK ~ 11 μ eV). Due to the ballistic nature of the channel (mean free path > 5 μ m), the electrons will impinge on the QD far from equilibrium when arriving due to a straight path trajectory [40], [44]–[46]. The effect of this non-equilibration is visible in the ΔI_{CS} data taken with transverse field $B_{\perp} = 0$ as a series of bumps preceding the peak in ΔI_{CS} (and deviating dramatically from the theoretical curve shown with a solid line). Although we do not have a microscopic explanation for the details of these bumps, they are suppressed by B_{\perp} as the trajectories from heating QPC are bent away from the QD. Unfortunately, magnetic fields of at least 200 mT were required to eliminate these deviations entirely (Fig. 4.5**b**), and at this field, the entropy measurement was perturbed both by the Zeeman energy of the field and by the onset of Shubnikov de Haas oscillations in the channel.

4.4. Common Problems

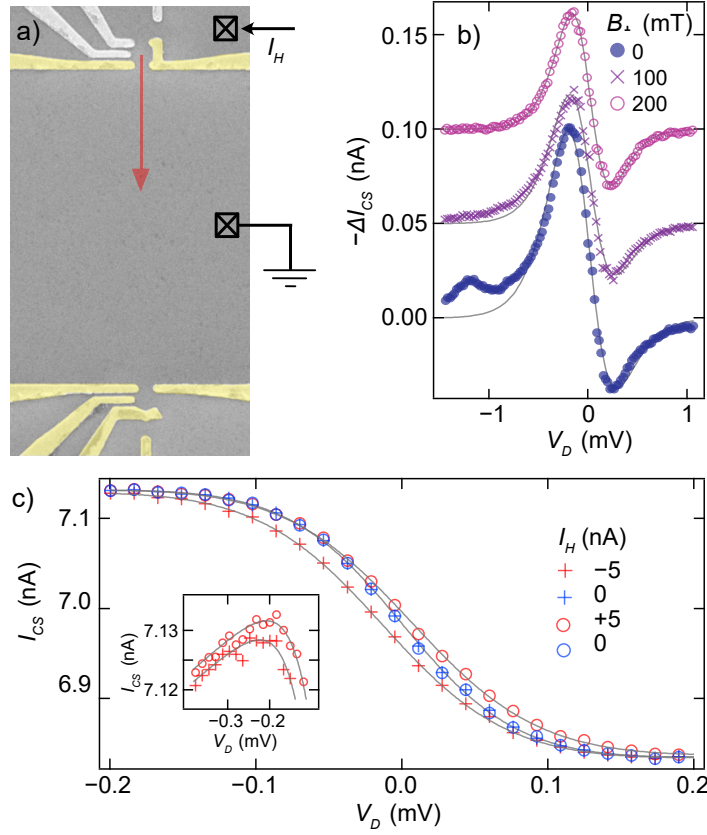


Figure 4.5: (a) False-colour scanning electron micrograph similar to the entropy measuring circuit from Ref. [8] where the thermal electron reservoir was heated by I_H through a single QPC (top), with no additional confinement of the heated channel. (b) Using the circuit in panel a, ΔI_{CS} measurements over the $0 \rightarrow 1$ transition for 0, 100 and 200 mT of magnetic field applied perpendicular to the plane of the 2DEG. Then, 100 and 200 mT data are offset by 0.05 and 0.1 nA respectively. Illustrates the effect of unthermalized electrons from the heater QPC reaching the QD, for 0 and 100 mT data. Fits to theory for weakly coupled transitions (solid grey) emphasize the deviation of data from theory on the $N = 0$ side of the transition. (c) Four segments of I_H square wave averaged separately, analogous to Fig. 4.4e and made using the circuit in Fig. 4.2a, but without proper balancing to keep the chemical potential of the reservoir at ground. The result is a shift of $I_H = +5$ nA with respect to -5 nA data. Inset: zoom-in to the $V_D = -0.4 \rightarrow -0.1$ mV range of the main panel, showing both lateral and vertical offsets ± 5 nA data.

4.5. Conclusion

Figure 4.5c illustrates the damaging effect of the direct (linear) offset of the reservoir potential due to I_H . When I_H is driven through the heater QPC in the geometry from Fig. 4.5a, a voltage offset is generated in the reservoir outside the QD due to the non-zero resistance to ground. This offsets μ , contravening the requirement to measure $\partial N/\partial T$ with μ fixed. At the same time, it may have a capacitive effect on the charge sensor, directly affecting the measurement of N . Because these effects reverse with the sign of the current being driven through the heater QPC, whereas the Joule heating itself does not, it is easy to identify their influence via a shift of the two heated traces (one at $+I_H$ and one at $-I_H$) away from each other. Direct influence on the reservoir potential causes the traces to separate laterally (Fig. 4.5c main panel), whereas cross-capacitive effects on the charge sensor cause the traces to separate vertically (Fig. 4.5c inset). Averaging the $\pm I_H$ traces together is not sufficient to remove these offsets due to non-linearity in $I_{CS}(V_D)$, and may artificially raise or lower the apparent entropy determined from analyzing ΔI_{CS} data.

While using a lock-in amplifier for the measurement of dN/dT has some advantages, it introduces its own set of challenges. Notably, the deviation from the $\Delta T \propto I_H^2$ relationship makes the lock-in-based approach problematic. This approach hinges on T_e changing at the second harmonic of a sinusoidal I_H , making it especially tricky to calibrate accurately. Additionally, the use of a lock-in amplifier can obscure the issues outlined in the previous paragraph, making them challenging to detect and address. These difficulties reinforce the merits of our alternation between T and $T + \Delta T$ approach.

4.5 Conclusion

This chapter has described the development of a new thermal circuit design and measurement protocol for quantifying entropy changes in mesoscopic devices in the quantum limit, based on monitoring how the charge of the system changes with temperature using a Maxwell relation. This same approach will be applied to more complex systems in the following chapters.

Chapter 5

Non-local entropy measurements in a double QD system

This chapter details an experiment in which an additional QD is coupled to the QD that we use for entropy measurement, demonstrating the ability to measure the entropy of a system that extends beyond that of the locally charge sensed QD.¹⁹ The measurements discussed in this chapter were significantly contributed to by Owen Sheekey, an undergraduate with whom I worked closely through the whole process from device fabrication to measurement and analysis.

5.1 Introduction

During the preliminary measurements that eventually led to the published work detailed in Chapter 4, we often observed anomalous deviations in the measured entropy change of the QD system from the anticipated $\Delta S = k_B \ln(2)$ upon adding a spinful electron to an empty QD. These early observations led us to think more deeply about the implications of the generality of our measurement technique, and ultimately, to better understand the potential to measure systems that extend beyond the QD that we measure the charge of directly.

As discussed in Section 4.4, several systematic issues can arise if the system is not heated carefully. Moreover, given the often significant background

¹⁹The proposals of Refs. [11] and [154] to measure exotic quantum states rely on such an ability.

5.1. Introduction

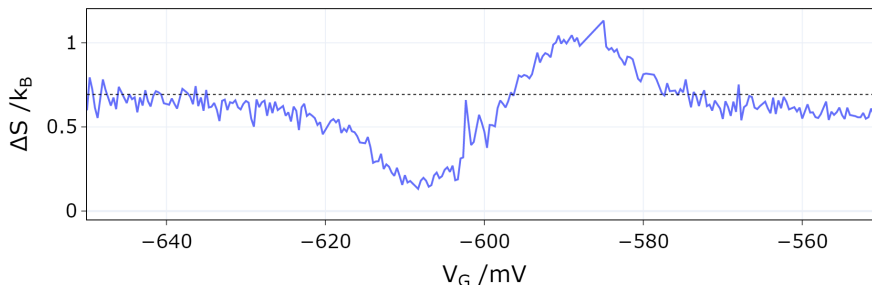


Figure 5.1: Measured entropy change ΔS from the addition of the first electron to a weakly coupled QD where an additional contribution varies as a function of the potential applied to one of the nearby gates. The dotted line marks $k_B \ln(2)$, the expected entropy change in the absence of additional contributions. Each value of ΔS corresponds to entropy change extracted from a 1D measurement over the $N = 0 \rightarrow 1$ charge transition of the QD.

noise relative to the ΔI_{CS} signal, especially during the device tuning phase where typically less averaging is applied in favour of measurement speed, a significant random error contribution is also expected. Thus, there were numerous reasons why we would not be surprised by considerable deviations from the anticipated entropy change in any given measurement. What was less expected, however, were deviations that were repeatable and robust over long periods of time. The repeatability ruled out signal-to-noise and other fluctuating measurement conditions over time as the cause of the deviations. These entropy deviations also remained consistent despite varying many controllable parameters (e.g., heating current, heater QPC settings, low magnetic fields), ruling out the systematic issues discussed in Section 4.4.

Upon a closer and more systematic investigation of the deviations, it was apparent that many had a characteristic “S” shape (Fig. 5.1): as we adjusted a single gate voltage, there was a region where entropy was below expectations, followed by a region above expectations, eventually settling back to $\sim k_B \ln(2)$. The reproducibility, combined with this S shape led us to hypothesize that we were observing a real effect stemming from an additional entropy change linked to a nearby impurity in the heterostructure. The behaviour would often depend very strongly on the tuning of one gate

5.1. Introduction

(i.e. small gate voltage changes of only a few mV), while other nearby gates (that one would expect to have a very similar effect on the QD based on their similar proximity) would have a much weaker effect on the deviation (10s or 100s of mV to have a similar impact). This reinforced our belief that these deviations arose from additional entropy contributions of impurities in the heterostructure, especially in the doped layers closer to the heterostructure surface than the 2DEG. The close proximity of these impurities to the heterostructure's surface might elucidate why some gates exerted more pronounced effects than others; specific gates could be in closer proximity to these impurities.

With this picture in mind, the entropy fluctuations have a simple explanation: impurities near the QD exist whose states are contingent on the local potential that includes a contribution from the QD's charge. For example, let us consider a charge impurity that has two possible states, $|A\rangle$ and $|B\rangle$. And, let us assume that the impurity is in close proximity to a gate with potential V_G , and the ground state of the impurity (with the QD unoccupied) is $|A\rangle$ for $V_G \leq -101$ mV, and $|B\rangle$ for $V_G \geq -99$ mV (shown in Fig. 5.2). In the intermediate regime (-101 mV $< V_G < -99$ mV), the impurity's state is a mixture of $|A\rangle$ and $|B\rangle$, and therefore, has an increased entropy in that regime (with a maximum of $k_B \ln(2)$ when $P(|A\rangle) = P(|B\rangle) = 0.5$). We then take entropy measurements by sweeping a plunger gate (e.g. V_{D1}) such that the occupation of the QD is increased by one (as described in Chapter 4). For simplicity, let us assume that V_{D1} couples only to the QD energy and has no impact on the impurity whatsoever. In the case that the QD's charge also has no impact on the impurity, then it makes no difference whether the impurity starts in a pure state or a mixture of states as its entropy will remain constant throughout the measurement. Because the entropy measurement is sensitive to change only, we would measure the $k_B \ln(2)$ entropy change of the QD alone for all V_G .

However, if we instead imagine that, the additional charge of the QD upon the addition of an electron, has an equivalent effect on the impurity as a -1 mV change in potential of V_G , then, depending on the initial V_G , the impurity may change state during an entropy measurement. For example,

5.1. Introduction

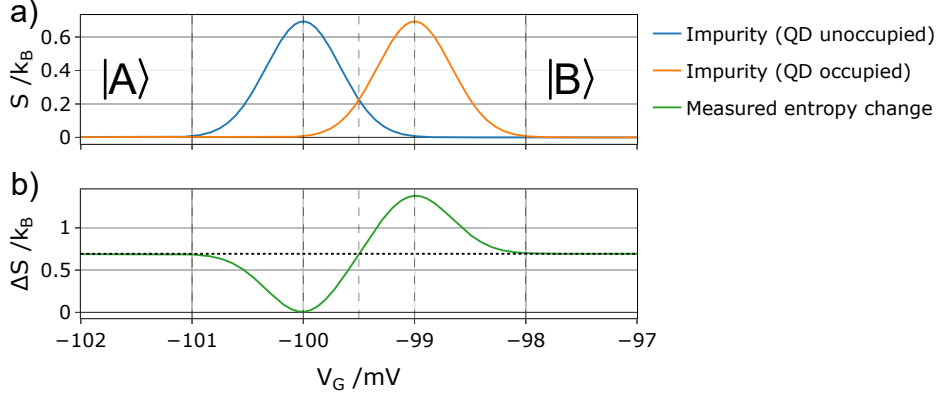


Figure 5.2: Fictitious example of an impurity's effect on measured entropy change of a QD. (a) The absolute entropy of the impurity that depends on the QD occupation. (b) The total entropy change that would be measured for the addition of the first electron to the QD for a range of V_G values.

if V_G starts at -100 mV, the increase in QD occupation during the entropy measurement will result in the impurity seeing an effective $V_G = -101$ mV by the end of the measurement, thus, changing it from a state with $k_B \ln(2)$ entropy (when $|A\rangle$ and $|B\rangle$ are degenerate), to a state with 0 entropy (when it is in state $|A\rangle$ only). Consequently, if we take several entropy measurements, varying V_G between each measurement from -102 to -97 mV, for example, the additional entropy change of the impurity can be broken into 6 parts (also depicted Fig. 5.2):

- $V_G \leq -101$ mV – No change as the impurity remains in the pure $|A\rangle$ state throughout
- -101 mV $< V_G < -100$ mV – Increasingly negative entropy change as the impurity starts in a mixture of $|A\rangle$ and $|B\rangle$ (initially $|A\rangle$ dominant) and ends in the pure $|A\rangle$ state.
- -100 mV $< V_G < -99.5$ mV – Decreasingly negative entropy change as the impurity starts in a more mixed state, and ends in a less mixed state (with a higher probability of $|A\rangle$).
- -99.5 mV $< V_G < -99$ mV – Increasingly positive entropy change as

5.1. Introduction

the impurity starts in a less mixed state (with a higher probability of $|B\rangle$), and ends in a more mixed state.

- $-99\text{ mV} < V_G < -98\text{ mV}$ – Decreasingly positive entropy change as the impurity starts in a pure $|B\rangle$ state, and ends in a mixed state that becomes increasingly $|B\rangle$ dominated
- $V_G \geq -98\text{ mV}$ – No entropy change as the impurity remains in the pure $|B\rangle$ state throughout

The generality of the derivation of Eq. 3.12 implies that the entropy change that we measure as we add an electron to the QD is not that of the QD’s entropy change alone, but the entire system as it depends upon the QD’s energy. Physically, this occurs through a thermodynamic back-action effect of the rest of the system on the QD [11]. At any specific QD energy ϵ , the charge on the QD reflects a minimization of the thermodynamic potential of the full system, not the QD alone. As a result, we would expect the additional contribution of the impurity’s entropy change to result in the S shape deviation from the $k_B \ln(2)$ entropy change expected of the QD in isolation.

It is important to remember that, for the Maxwell relation (Eq. 3.5, upon which Eq. 3.12 is derived) to be reliable, the full system must be in thermodynamic equilibrium. This is an assumption that we cannot make when considering impurities that lie within the heterostructure itself, due to the way in which we currently heat the system. Because we heat the 2DEG electrons directly, we cannot assume that the phonon temperature of the heterostructure is in equilibrium with the 2DEG. In fact, we assume that most of the heterostructure remains in thermal equilibrium with the cryostat because the thermal conductivity between the cryostat and heterostructure is much stronger than that of the electron-phonon coupling between the 2DEG and the heterostructure phonons at low T [58]. Given that we expect the charge impurities to live within the heterostructure, electrically isolated from the 2DEG, we cannot assume a thermal equilibrium of the full system, and thus, although the measured deviations were still indicative of local entropy changes, the magnitude and precise nature of the changes measured

5.2. Device Design

were untrustworthy. Therefore, to explore the idea of sensing the additional entropy change of nearby impurities further, we designed a device in which the behaviour of a nearby impurity is mimicked by a second QD. By doing so, we can make concrete comparisons between measurements and a system that we can make precise predictions for, whilst also ensuring thermal equilibrium of the full system. The rest of this chapter describes the design and measurements of this device.

5.2 Device Design

The device used for these measurements is the same device as presented in Chapter 4, only we are now interested in additional features of that device that can be seen in Fig. 5.3 (that were hidden behind the inset of Fig. 4.1). These additional gates are used to form a second QD, close to the entropy-sensing QD, to act as a controllable impurity. In fact, the same device was designed with three experiments in mind, and as such, also included gates to form a third QD (greyed-out gates in Fig. 5.3), but those can be ignored for the remainder of this chapter.

The second QD (QD2) that acts as the impurity was designed to be nearly identical to QD1, both being modifications from previous devices that indicated QD diameters of ~ 200 nm are ideally suited (in this particular heterostructure) to have their occupations be tuneable down to empty $N = 0$ QDs. Although it is not technically necessary to be able to reach $N = 0$ to perform the intended measurements, there are a couple of advantages to doing so. With small QDs that hold very few electrons, the orbital energy spacing of the QD energy levels Δ is large, and thus, we can more safely assume that only the lowest orbital energy is occupied at the low T used in the experiment. In addition, with a maximum of one electron per QD, we can be sure that there are not unintended complex ground states for the QDs to fall into as a result of many-body interactions within the QD, thereby simplifying the interpretation of any measurements. Additionally, QD2 was designed with direct coupling to the thermal reservoir so that we can be sure that it (as well as QD1) remains in thermal equilibrium with

5.2. Device Design

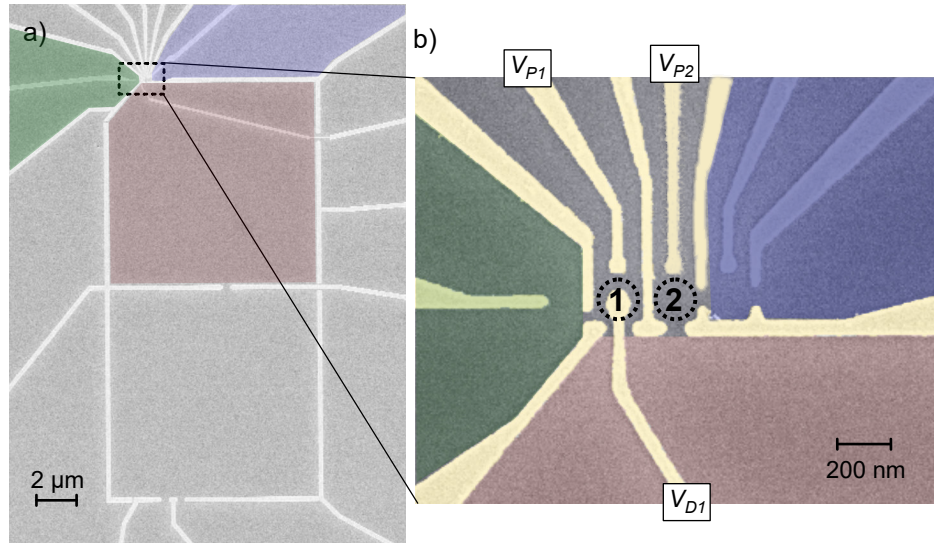


Figure 5.3: False-coloured scanning electron micrographs (SEMs) of the device, with (a) showing the heater reservoirs, and (b) showing where the two QDs form. The green region represents the charge sensor. Red represents the thermal electron reservoir that is heated and cooled rapidly during entropy measurement. Blue represents an area of 2DEG that remains cold and must be decoupled from QD2 in order to ensure QD2 remains in thermal equilibrium with the thermal reservoir. Note that the gate labelled V_{D1} is varied only close to 0 V, and as a result, is largely transparent to the 2DEG (in comparison to the other gates that typically form opaque barriers in the 2DEG). The two greyed-out gates in the blue region are unused and kept grounded. For more detail of connected circuitry, see Figs. 4.1 and 4.2 that depict the same device.

5.2. Device Design

the reservoir at all times.²⁰

The placement of QD2 was chosen such that it is as close as possible to the entropy sensing QD whilst being as far from the charge sensor as possible. We want the two dots to have a strong inter-dot Coulomb interaction energy U [155] such that the occupation of QD2 is highly dependent on the occupation of the entropy sensing QD1 (to mimic the charge impurities), but we also want to minimize the direct contribution of QD2's occupation on the charge sensor current. Minimizing the direct effect of QD2's occupation on the charge sensor is important when it comes to converting the change in current through the charge sensor (ΔI_{CS}) to dN_{QD1}/dT . This is because we typically assume, after accounting for the direct cross-capacitance of the sweeping gate on the charge sensor, that ΔI_{CS} can be directly related to a ΔN of the entropy sensing QD alone (ΔN_{QD1}). On a related note, a significant difference between QD1 and QD2 is the absence of an "accumulation" gate over QD2 (so-called because we originally intended to accumulate charge underneath it by applying positive potential). For QD1, the gate directly over the QD helps to minimize the direct cross-capacitive effect on the charge sensor when sweeping over the QD transition (as discussed in Section 4.2). For QD2, it is not necessary to have such a gate, as we do not intentionally sweep the QD2 energy level during the measurement. Between measurements, it is sufficient to use the more conventional V_{P2} gate (that has a weaker lever-arm) to tune the QD2 energy level.

Because the third QD gates were left grounded (and had a negligible effect on the 2DEG), QD2 was left with a second tunnel barrier that controlled its coupling to the unthermalized (cold) 2DEG (blue area of Fig. 5.3). Additional care was taken to ensure that QD2's coupling to the unthermalized reservoir was much weaker than that to the thermalized one, to ensure the proper thermalization of QD2.

As described in Chapter 4, two-stage heating reservoirs are used to en-

²⁰More recent measurements appear to indicate that it is possible to maintain thermal equilibrium via strong enough coupling to a QD that is itself coupled to the thermal reservoir, but at the time of these measurements, we wanted to be very sure that thermal equilibrium would not be an issue.

5.3. Methods

sure a uniform thermal distribution in the reservoir that is coupled to the QDs. All tuning and operation of the heating reservoirs is the same as that previously described.

5.3 Methods

The device was cooled from room temperature to 100 mK with +400 mV bias applied to all gates excluding V_{D1} that was left grounded (Section 2.6). This is particularly noteworthy for the V_{P2} gate; although it is operated with positive potentials in this measurement, the frozen-in potential from the cooldown bias means that the 2DEG effectively sees a net negative potential, similar to the rest of the gates.

After the device was cooled, we first tuned the double QD system into a weakly coupled regime, where both QDs were weakly coupled to the thermal reservoir ($\Gamma_{QD1}, \Gamma_{QD2} < k_B T$). While the QDs have a reasonably strong Coulomb interaction, there is no direct tunnel coupling between them, though they can exchange an electron via the reservoir (discussed further in Section 5.5). Similar to the measurements in Chapter 4, we aimed for this weakly coupled regime to simplify the measurement both theoretically and experimentally. Because of the weak coupling, the QD charge transitions were thermally broadened and, at the low T that we measured, relatively sharp in terms of plunger gate potential. The benefits of thermally broadened sharp transitions are two-fold: ease of dot tuning and charge sensor signal strength. To elaborate, dot tuning is made easier because the change in QD occupation shows up more clearly in charge stability plots (Fig. 5.4, for example) as a result of causing a more sudden change in charge sensor current as the plunger gate is swept. Broader transitions tend to get lost in comparison to the direct cross-capacitive effects of the plunger gate. Additionally, the transitions being thermally broadened results in a much stronger dependence of the occupation of the QD on the temperature of the heated reservoir. This is beneficial for QD1, as it is this temperature dependence that results in the charge sensor signal ΔI_{CS} that we scale and integrate to calculate the entropy of the system.

5.3. Methods

Although QD2 was designed to be as far from the charge sensor as possible, the occupation of the second QD did still have a small ($\sim 1/5$ that of the first QD) effect on the conductance of the charge sensor QPC. Although this behaviour is not ideal for the conversion of ΔI_{CS} to dN_{QD1}/dT , this weak effect did help facilitate relatively easy tuning of the system, as the charge state of both QDs was detected by the single charge sensor (as seen in Fig. 5.4). This enabled us to tune into a state in which both QDs were minimally occupied ($0 \leq N \leq 1$).

Figure 5.4 depicts the charge stability of the double dot system, focusing on the region in which both QDs have occupations between zero and one. There are a few noteworthy observations to make from these plots. We can see that the cross-capacitive effect of QD2 on the charge sensor is much weaker than that of QD1 by the significantly smaller change in differentiated current (roughly a factor of 5 difference) of the charge transition lines that are associated with QD2 (the more horizontal lines). The reduced effect is a result of both the increased distance between the charge sensor and QD2, and the additional screening from the gate between the two QDs. We can also see the effect of the inter-dot capacitance, apparent as the diagonal (blue) line between the two triple points in Figs. 5.4**b,c**. The diagonal line represents gate voltages where the lowest unoccupied energy levels of both QDs are degenerate and below that of the Fermi energy; along this line, it is energetically favourable to have an electron in either of the two QDs, but not both at the same time (as depicted in Fig. 5.8). In other words, if one dot has the N^{th} electron, the energy cost of adding an electron to the other dot is increased by U due to the presence of the additional negative charge in the first dot.

For the range of V_{P2} where the occupation of the first dot influences the occupation of the second, the double dot system is in a regime that is analogous to the single QD with a nearby impurity that contributes to the entropy change of the system. To realize a situation in which it is only the occupation of QD1 that affects QD2, and not additionally the V_{D1} potential, a virtual gate ($D1'$) is used to sweep the QD1 energy while holding the QD2 energy constant (Fig. 5.4**c**). Then, entropy measurements are carried out

5.3. Methods

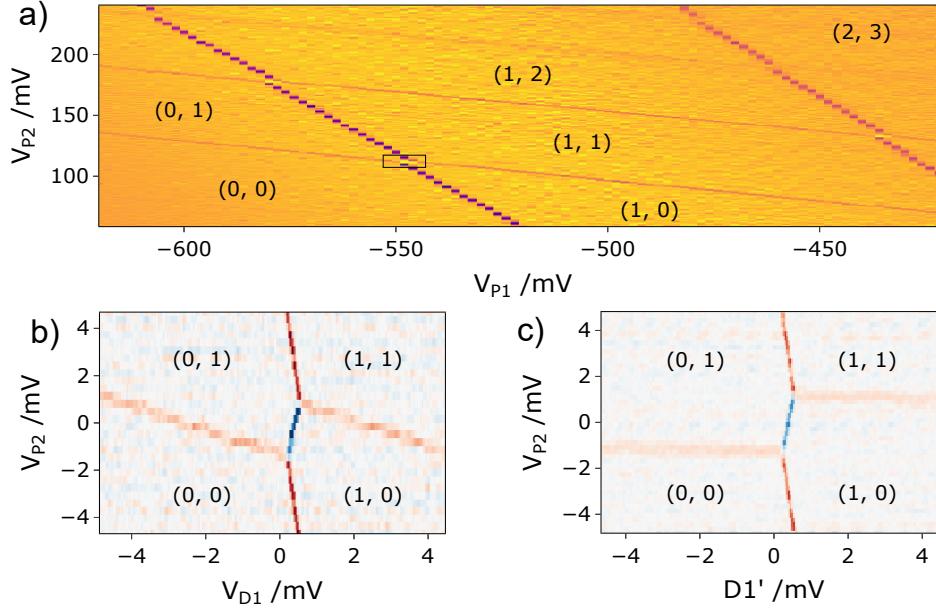


Figure 5.4: Charge stability plots of the double dot system. All panels show charge sensor current differentiated in the y-direction in order to emphasise the charge transitions of both QDs (QD2 transitions – the more horizontal lines – are hard to see otherwise). In all panels, lines represent where the occupation of QD1 increases from left to right, and QD2 from bottom to top. (a) Various charge states of the two QDs (N_{QD1}, N_{QD2}) over a relatively wide range of gate space. The rectangle at $(-550, 110)$ depicts the region measured in the lower panels. (b and c) Fine scans over the region indicated in panel a where the applied gate voltages represent fine-tuned control in addition to fixed gate voltages chosen near the inter-dot charge degeneracy point. Panel c is measured with a virtual x-axis gate that holds the QD2 occupation constant (hence, the horizontal QD2 transition lines). The diagonal line between triple points (blue colour) is where the two QDs are charge degenerate. Note that the blue line does not represent an inherently different effect of the charge transition on the charge sensor current; it is merely a consequence of the differentiation axis, which conveniently serves to highlight the region of interest.

5.4. Results

using the same procedure and parameters as discussed in Chapter 4.

5.4 Results

The possible states of the double dot system can be expressed in terms of the states of the individual dots. Considering just the 0 or 1 occupation of the two dots, the possible states for the double dot system would be $|0, 0\rangle, |0, 1\rangle, |1, 0\rangle, |1, 1\rangle$, where $|A, B\rangle$ corresponds to dot QD1 with state $|A\rangle$ and QD2 with state $|B\rangle$. Since we have no in-plane magnetic field applied, the electron spins are degenerate, and the occupied state can either be $|\uparrow\rangle$ or $|\downarrow\rangle$, resulting in 9 possible states in total (assuming $0 \leq N_{QD1}, N_{QD2} \leq 1$). Figure 5.5 depicts the possible states of the full system at various key points in gate space. The entropy of the full double dot system can be calculated using the Gibbs entropy formula (Eq. 3.2), and as discussed in Section 3.1, we expect to measure the change in entropy from the initial state (left) to final state (right). The summary of expected entropy changes at key points are given in Table 5.1.

V_{P2} /mV	Fig. 5.6 Panels	Initial States	Final States	Entropy Change $/k_B$
0.8	b, f	$ 0, \uparrow\rangle, 0, \downarrow\rangle$	$ \uparrow, \uparrow\rangle, \downarrow, \uparrow\rangle,$ $ \uparrow, \downarrow\rangle, \downarrow, \downarrow\rangle,$ $ \uparrow, 0\rangle, \downarrow, 0\rangle$	$\ln(6) - \ln(2) =$ $\ln(3)$
-0.5	c, g	$ 0, \uparrow\rangle, 0, \downarrow\rangle$	$ \uparrow, 0\rangle, \downarrow, 0\rangle$	$\ln(0)$
-2	d, h	$ 0, 0\rangle, 0, \uparrow\rangle,$ $ 0, \downarrow\rangle$	$ \uparrow, 0\rangle, \downarrow, 0\rangle$	$\ln(2) - \ln(3)$
-3	e, i	$ 0, 0\rangle$	$ \uparrow, 0\rangle, \downarrow, 0\rangle$	$\ln(2)$

Table 5.1: Summary of the Initial and Final states of the double dot system corresponding to Figs. 5.6**b-i**, including the total entropy change of the system for each case.

Figure 5.6 summarizes the key measurements of the double QD system in the weakly coupled regime. Figure 5.6**a** shows the charge sensor signal

5.4. Results

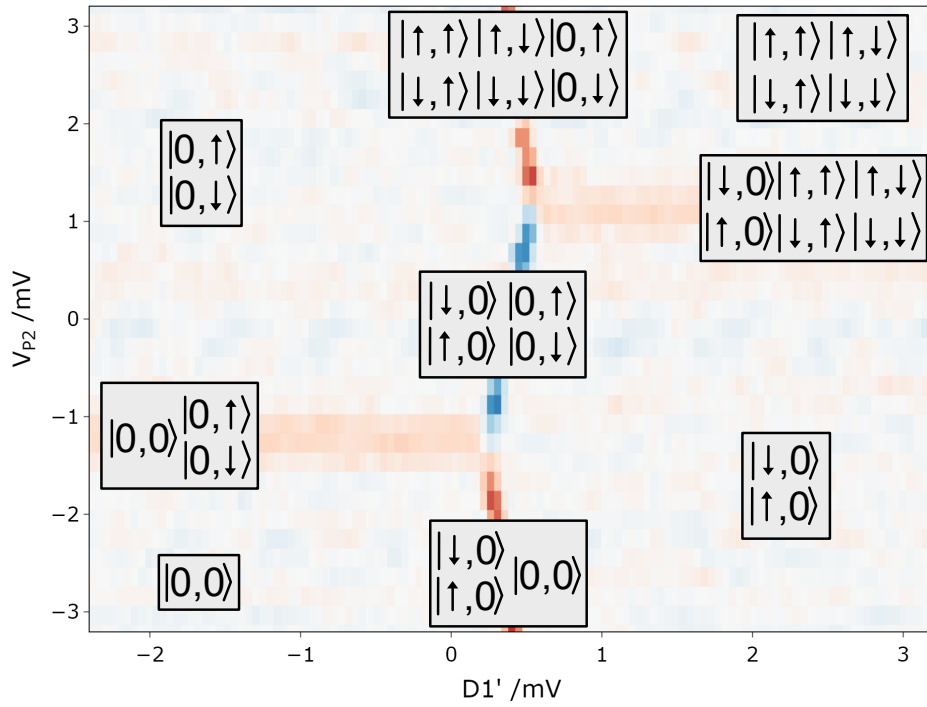


Figure 5.5: Charge stability diagram with possible double dot states overlaid at key positions. $|\uparrow, \downarrow\rangle$ represents a state in which QD1 is occupied with a spin-up electron, and QD2 is occupied with a spin-down electron, for example. The data is the same as that of Fig. 5.4c.

5.4. Results

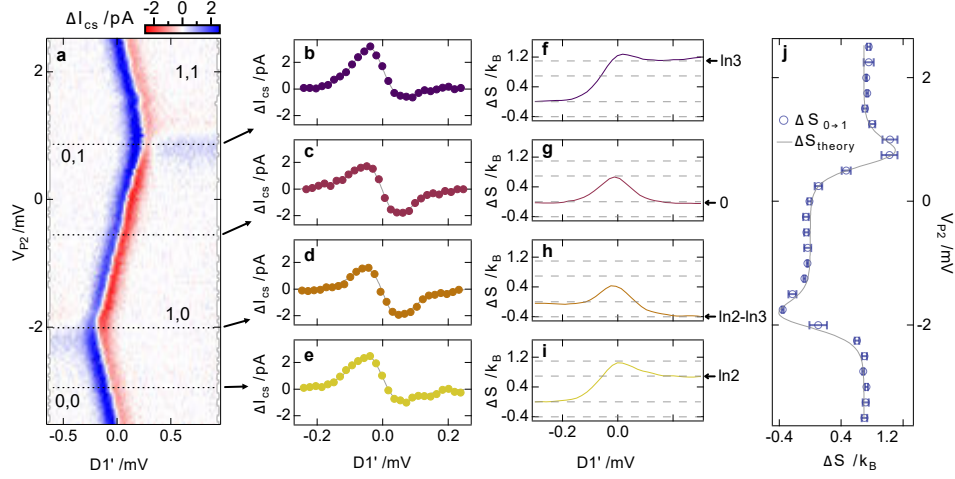


Figure 5.6: (a) Charge sensor signal, $\Delta I_{CS} \propto dN/dT$, as a function of a virtual gate controlling the QD1 energy, and a plunger gate that primarily affects the QD2 energy, where both represent fine-tune additions to coarse gate values set close to inter-dot charge degeneracy. Occupations of the two QDs are displayed for various regions of the graph with notation (N_{QD1}, N_{QD2}) . For simplicity, a virtual gate is not used for QD2, hence the slope in the QD1 transition at the top and bottom of panel a. (b–e) Line cuts from a taken at $V_{P2} = 0.8, -0.5, -2$ and -3 mV respectively, that when integrated result in the entropy changes ΔS shown in panels (f–i). (j) The total entropy change of the system calculated from the measurement shown in panel a. All but panel j have x-axes that correspond to the energy of QD1, where the occupation increases from left to right at the near vertical feature in panel a, similar to that of Fig. 5.4). Similarly the y-axis of panels a and j primarily correspond to the energy of QD2, where occupation increases from bottom to top at the faint horizontal features in panel a. Table 5.1 summarizes the expected mixed states and entropy changes of the system at the key points depicted in panels b–i.

5.4. Results

$\Delta I_{CS} \propto dN/dT$ as a function of the occupation of both dots where the effect of the Coulomb interaction U can again be seen by the diagonal line $((-0.2, -2)$ to $(0.2, 1))$ between triple points. Similar to the charge stability measurements, the ratio of contribution to the charge sensor signal directly from QD1 compared to QD2 is again $\sim 5 : 1$, as expected. Note that, in the regimes where the QD2 occupation remains constant, there is no additional contribution. Additionally, in the regime where charge transfers between the two QDs (and not the reservoir), the additional contribution can be accounted for because $N_{QD1} = 1 - N_{QD2}$ exactly. Effectively, the amplitude of the QD1 charge transition is reduced by 20%, but that reduced value can be used when scaling the charge sensor signal to entropy. It is not trivial to account for the additional QD2 contribution in the regimes where charge transfers occur between both QDs and the reservoir ($V_{P2} \approx -2$ and 0.5 mV), however, to distinguish between $\ln(3)$ and $\ln(2)$ or $\ln(2/3)$ and 0 , the $< 20\%$ contribution is acceptable. Thus, although we would ideally see no contribution from QD2, for the purpose of these measurements, the effect is small enough in the regime that it cannot easily be accounted for that it does not significantly impact the interpretation of the results. Figures 5.6**b–e** are 1D linecuts from Fig. 5.6**a**, highlighting some of the key features of the double dot system. Figures **f–i** show the same data scaled and integrated according to Eq. 3.12, where the final values can be compared to the entropy changes listed in Table 5.1.

Let us first consider Figs. 5.6**e,i**, representing gate voltage settings where N_{QD2} remains zero throughout the addition of an electron to QD1 – the same scenario as in Chapter 4 where we measure the entropy change of single weakly coupled QD alone. We again see an asymmetric ΔI_{CS} that corresponds to a total entropy change of the system of $k_B \ln(2)$ with a peak at $k_B \ln(3)$ where QD1 is both charge and spin degenerate. For Figs. 5.6**d,h**, on the left side of the QD1 transition, we start with QD2 in a state of charge and spin degeneracy with the thermal reservoir, $(|0, 0\rangle, |0, \uparrow\rangle, |0, \downarrow\rangle)$. As an electron is added to QD1, we first see an increase in the entropy of the system corresponding to an additional charge degeneracy with QD1 at the triple point, followed by a net loss of entropy of the system. The final entropy

5.4. Results

change of $k_B \ln(2) - k_B \ln(3)$ corresponds to the system ending in a state where only QD1 is spin degenerate, ($|\uparrow, 0\rangle, |\downarrow, 0\rangle$), losing the spin and charge degeneracy of QD2. Figures 5.6**c,g** show a net entropy change of zero as a result of the system starting with a spin degeneracy in QD2, and ending with a spin degeneracy in QD1, with a region in the middle with an additional $k_B \ln(2)$ (for a total of $k_B \ln(4)$) entropy where there is both spin and charge degeneracy of both dots. Finally, we have Figs. 5.6**b,f**, where the system starts with no electrons in QD1 and one spin-degenerate electron in QD2, ($|0, \uparrow\rangle, |0, \downarrow\rangle$). For the final state of the system, we see how even very simple systems can have a relatively complex mixture of states in the ground state. The system ends in a state where QD1 is occupied with a spin-degenerate electron, and QD2 is both spin and charge degenerate (where the charge degeneracy is with the reservoir), resulting in 6 equiprobable possible states, ($|\uparrow, \uparrow\rangle, |\downarrow, \uparrow\rangle, |\uparrow, \downarrow\rangle, |\downarrow, \downarrow\rangle, |\uparrow, 0\rangle, |\downarrow, 0\rangle$). Therefore, a total entropy change of $k_B \ln(6) - k_B \ln(2) = k_B \ln(3)$ is observed.

Although we consider the contribution from QD2 to be negligible, the small contribution from it can be seen on the far right side of the data in Fig. 5.6**f**. The contribution shows up as a linear slope from a constant charge sensor signal contribution that does not depend on the occupation of QD1. Because the change of occupation of QD1 is zero ($\Delta N = 0$), the contribution to the charge sensor signal ($\Delta I_{CS} \propto dN/dT$) should also be zero. The result of not properly accounting for this undesired contribution to the charge sensor signal is a constant offset in dN/dT resulting in a linear slope of the integrated entropy. Having QD1 tuned to the weakly coupled regime where the transition is relatively narrow reduces the contribution from QD2; conversely, for a more strongly coupled QD1, the same constant offset would be integrated over a wider range resulting in a larger error overall.

Figure 5.6**j** depicts the total entropy change of the double QD system along the full range of Fig. 5.6**a**. The grey line corresponds to theory calculation of the double dot system, sent to us by Yigal Meir. The calculations take into account the energies of the two QDs ϵ_1 and ϵ_2 , the chemical potential of the reservoir μ , the temperature of the system T , and the inter-dot

5.5. Discussion

Coulomb interaction U . For the comparison to data, $U/T = 15$ fits best, representing a Coulomb interaction energy between the QDs that is much larger than $k_B T$. This can be seen qualitatively in the data by the relatively narrow charge transitions (that are thermally broadened) compared to the separation between triple points that arises from the Coulomb interaction between the QDs. When fitting the calculations to data, a linear scaling of the energy axis is applied to account for the conversion between plunger gate potential and dot energy. The near-perfect fit between calculation and measurement indicates that our measurement protocol is well suited to measuring the entropy change of full systems based on charge measurements of only a single “entropy sensing” QD.

5.5 Discussion

It is worth noting that, compared to the single QD measurements, the coupling between the QDs and reservoirs in the double dot setup had to be much stronger, although still maintaining $\Gamma \lesssim k_B T$. Specifically, the stronger coupling of each of the QDs was required in the regime where charge transitions occur between the QDs (rather than with the reservoir). The fact that the entropy measurement depends on the assumption that the system is in thermodynamic equilibrium requires the N that we measure to be the time average $\langle N \rangle$. When the device was tuned to have $\Gamma \ll k_B T$, we found that there was a significant region in which the rate of charge transfer back and forth between the two QDs could be as slow as 100 ms – much slower than our measurement – and therefore we were resolving the N^{th} electron to be discretely in either the left or the right QD, and not the time average.

Figure 5.7 depicts such behaviour, where Fig. 5.7a is a charge sensor current measurement (sweeping at ~ 20 mV/s) over a similar range as the previously discussed measurements. Notably, in the region where an electron transfers between the QDs, the signal shows many discrete jumps that often occur far from the charge degeneracy point. A single, much slower (~ 0.05 mV/s), measurement through the middle of this region ($V_{P2} = 0$ mV) is shown in Fig. 5.7b where, $I_{CS} \sim 7.6$ nA indicates QD2 is

5.5. Discussion

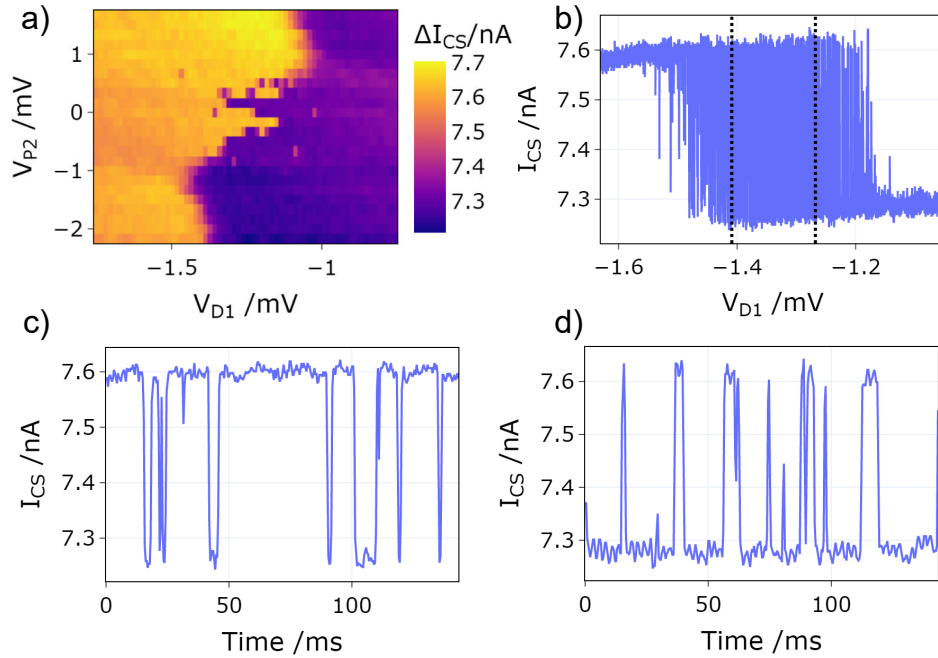


Figure 5.7: (a) Charge stability diagram of the double dot system in a regime where both dots are very weakly coupled to the reservoir. The apparently noisy region in the middle indicates that we are detecting discrete charge transitions between the QDs (rather than a time average). (b) charge sensor current of a much slower 1D scan at $V_{P2} = 0 mV$ that includes 100s of discrete charge jumps back and forth between the two QDs. (c and d) Close-up of the data shown in panel b where V_{D1} is effectively static over the range of measurement shown, hence, a time-axis is displayed.

5.5. Discussion

occupied, and $I_{CS} \sim 7.3 \text{ nA}$ indicates QD1 is occupied. By zooming in to two regions indicated by the vertical dotted lines, we can see the behaviour of the system as a function of time in regimes where the electron preferentially occupies QD2 (left, **c**) or QD1 (right, **d**). The sudden steps indicate individual tunnelling events from one QD to the other (via the reservoir) on a timescale of milliseconds, therefore, each individual measurement point is not representative of the thermodynamic equilibrium of the system.

As depicted in Fig. 5.8, we understand this drastically reduced rate of charge exchange to be a result of the fact that a second-order process is required for the electron to move from one QD to the other. For example, because the two dots are only capacitively coupled, the electron must pass through the reservoir as an intermediate step between QDs. (This is true even when the QD energy levels are aligned.) This is similar to the insulating phase of a QD in Coulomb blockade discussed in Section 2.3 (in the absence of the Kondo effect); to have current pass through the QD, there would need to be an intermediate state in which the dot is unoccupied (or doubly occupied) that, for a first-order transition, is energetically forbidden. However, similar to the discussion of the Kondo effect in QDs (Section 3.2), such intermediate steps are possible as virtual states, albeit, their rate of occurrence is relatively low. In the case of a double QD, rather than a QD coupled to two leads, we have two QDs coupled to a single lead. When two QDs have degenerate energy levels, after an electron leaves either QD, another electron will be equally likely to enter either QD. If the QDs have different energy levels, the lower energy state will be more likely to be filled; as a result, the lower energy state will naturally be occupied most of the time. In contrast to the measurement in Fig. 5.7, we require these virtual processes to occur much faster than we measure. This allows the system to explore all possible states in thermal equilibrium between measurements, as required for the entropy measurement protocol. We achieved this requirement by coupling each QD to the reservoir more strongly than we did in the measurements described in Chapter 4, while maintaining $\Gamma \lesssim k_B T$.

5.5. Discussion

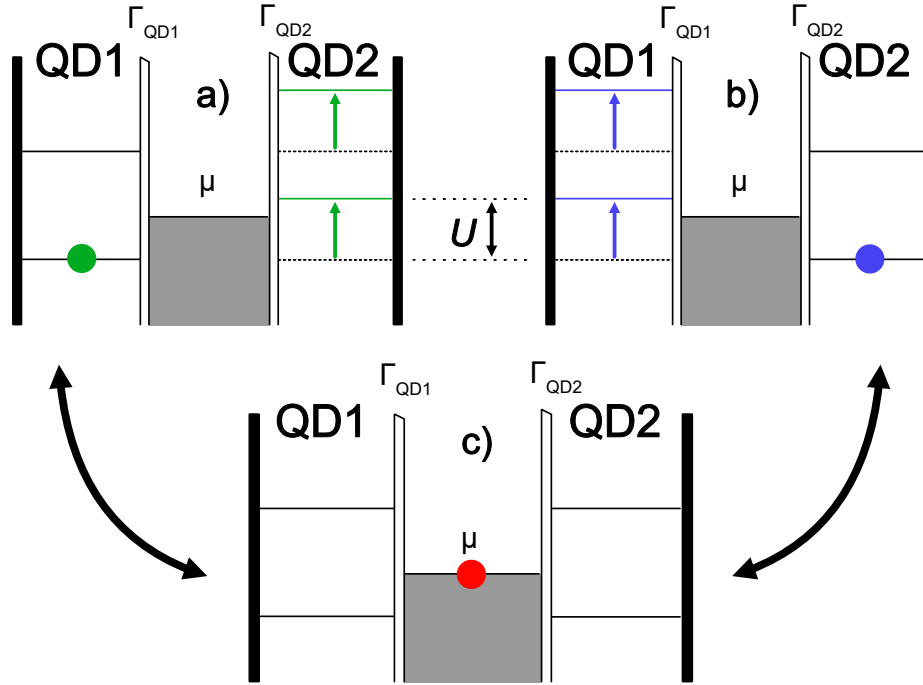


Figure 5.8: Schematics of the double dot system depicting charge transfer between the two QDs. QD1 and QD2 are coupled to the reservoir (that has chemical potential μ) with coupling strengths Γ_{QD1} and Γ_{QD2} respectively. (a and b) Schematics with QD1 or QD2 occupied, respectively, where the occupation of either QD shifts the energy levels of the other QD to higher energy as a result of the inter-dot Coulomb interaction U . (c) The intermediate step that facilitates the transfer of an electron from one QD to the other.

5.6 Conclusion

Overall, the measurements of this double dot system, where the second QD is capacitively coupled to the entropy sensing QD, serve as a good intermediate demonstration of the generality of our entropy measurement protocol. The fact that we can detect entropy changes of a second QD by charge sensing only the first QD demonstrates the use of the single QD as a more general entropy sensor for any system that is coupled to the charge of that QD (and in thermal equilibrium with it). I call this an intermediate demonstration because, although the system is more complex than a standalone QD, the measurements are so far made in the weak coupling limit where more limited approaches (such as Ref. [8]) may remain applicable.

Our double dot measurements also represent progress towards experiments like those proposed by Sela et al. [11] and Sankar et al. [154]. For example, Sela et al. [11] propose to measure the non-trivial $\frac{1}{2}k_B \ln(2)$ entropy of a Majorana zero mode (MZM). This proposed experiment involves engineering a system in which the presence of a single MZM depends upon the charge state of a QD. Then, as demonstrated in this chapter, with the presence of an MZM controlled by the charge on a QD (even if only by a weak capacitive coupling), the measurement of the entropy change as the occupation of a QD is varied will include the entropy change of the MZM system as well. A brief overview of the proposed experiment follows. First, one requires a system in which MZMs are expected to form, such as a semi-conducting nanowire [156]–[161]. Then, because MZMs naturally come in pairs (the Majorana qubit) with a trivial $\ln(2)$ entropy like any two-level system, it is required that the behaviour of one MZM be separated from the other. This can be achieved by coupling (with strength Γ) one end of the nanowire to a lead with a continuous density of states [10]. Specifically, when $\Gamma \gg T$, one of the MZMs is absorbed into the levels of the lead, and as a result, no longer contributes to the entropy of the nanowire system (and thus leads to a $-\frac{1}{2}k_B \ln(2)$ entropy change of the system). The crucial step that would allow for the detection of this entropy change is to connect the change of occupation of a QD (i.e. the entropy sensing QD discussed in this

5.6. Conclusion

chapter) to the change in the coupling of the nanowire system to its lead. If a change in the occupation of the QD can change Γ from $\Gamma \gg T \rightarrow \Gamma \ll T$, then the entropy associated with the transition can also be measured. This, in theory, can be easily achieved by placing the QD in close proximity to the nanowire-lead barrier, then (by capacitive coupling), the occupation of the QD will affect the local potential of the barrier, thus affecting Γ . In this situation, the thermal response of the QD charge as one (or more) electrons are added to the QD will (through thermodynamic back-action) reflect the entropy change of the full system [11]. Note that it is not necessary for the absorption of the MZM to the lead to depend upon a single charge transition of the QD; one could instead integrate the entropic contributions of the addition of several charges to the QD. Experimentally, the difficulty of such a procedure will involve designing a circuit in which the nanowire-lead barrier has a sufficient dependence on the charge of the QD such that the barrier can be tuned between the two extremes within a reasonable change of occupation of the QD. Additionally, one will have to be very careful that the experimental procedure for measuring the combined contribution of several consecutive charge steps of the QD takes into account the inevitable direct cross capacitance between the QD plunger gate and the nanowire-lead barrier, particularly as the plunger gate will have to be swept orders of magnitude further than in the measurements discussed in this chapter to sweep over many charge transitions. Nevertheless, the measurements discussed in this chapter are fundamentally very similar in procedure to those proposed in Ref. [11].

Chapter 6

Entropy measurements in the mixed valence regime

In this chapter, the first measurements of the entropy of a system showing signs of Kondo correlations are presented. This chapter largely follows that of already published work that can be found at Ref. [152].

6.1 Introduction

The measurements discussed in this chapter serve a dual purpose: they represent the first measurements of entropy in which Kondo correlations are expected to be present, and more generally serve as a demonstration of the generality of the new measurement approach where the foundational approach of Ref. [8] is clearly not applicable. Where the previous approach relied upon knowledge of the precise lineshape of a weakly coupled charge transition of the QD, in this chapter, the measurements lie well outside the weak coupling limit in a regime where there is no analytical solution to the lineshape of the charge transition. Therefore, it is the new general entropy measurement protocol described in Section 3.1 that allows us to measure entropy in this regime.

Single-impurity Kondo systems have been realized in several previous experiments [109], [111]–[114], [116]–[119], [121] that probed the Kondo state via measurements of conductance. Here, we perform the first entropy measurement of a Kondo-correlated dot, using the in situ heater and charge sensing approach outlined in the previous chapters. Recently, more complicated structures including multiple dots have been engineered to host multi-channel Kondo states [162], [163], or a three-particle simulation of

6.2. Methods

the Hubbard model [164]. We hope that this demonstration of direct entropy measurement of a single-impurity Kondo system will act as a step towards similar measurements in these more complex systems as entropy measurements made on any of these would offer a significant advance in their understanding.

6.2 Methods

We use the technique discussed in Section 3.1, starting by first replicating the measurements of Chapter 4 where the coupling Γ between the QD and reservoir is weak ($\Gamma \ll k_B T$). We then show that the onset of entropy as the electron enters the QD is strongly modified when $\Gamma \gtrsim k_B T$. The measurement of this modified entropy signature is the primary result of this work in this chapter, offering clear entropic evidence of the effect of strong reservoir coupling on the quantum state.

Measurements were performed on the same mesoscopic circuit used to obtain the measurements discussed in Chapter 4 (Fig. 6.1a). However, in this chapter, the device is operated in a very different regime. As before, the device includes a QD, a charge-sensing quantum point contact, and an electron reservoir that can be rapidly Joule-heated above the chip temperature T to an elevated $T + \Delta T$. However, in these measurements, the coupling Γ between the QD and the thermal reservoir was varied from $\Gamma \ll k_B T$ to $\Gamma \gg k_B T$. The coupling occurs via a single tunnel barrier that is controlled by V_T .

Throughout this chapter, V_D is reported with respect to the midpoint of the $N = 0 \rightarrow 1$ charge transition ($\Delta V_D \equiv V_D - V_D(N = 1/2)$) because the V_D gate is generally kept close to zero potential anyway ($|V_D| < \sim 10$ mV), and it is much easier to make comparison between the various measurements with a fixed reference point that has physical meaning. N in the QD was monitored via the current, I_{CS} , through the charge sensor [47] (Fig. 6.1b), which was biased with a DC voltage, typically 100 μ V. Changes in occupation, N , were scaled from I_{CS} using I_e , the change in I_{CS} across a 1e charge transition (following the same protocol discussed in Chapter 4). Fig-

6.2. Methods

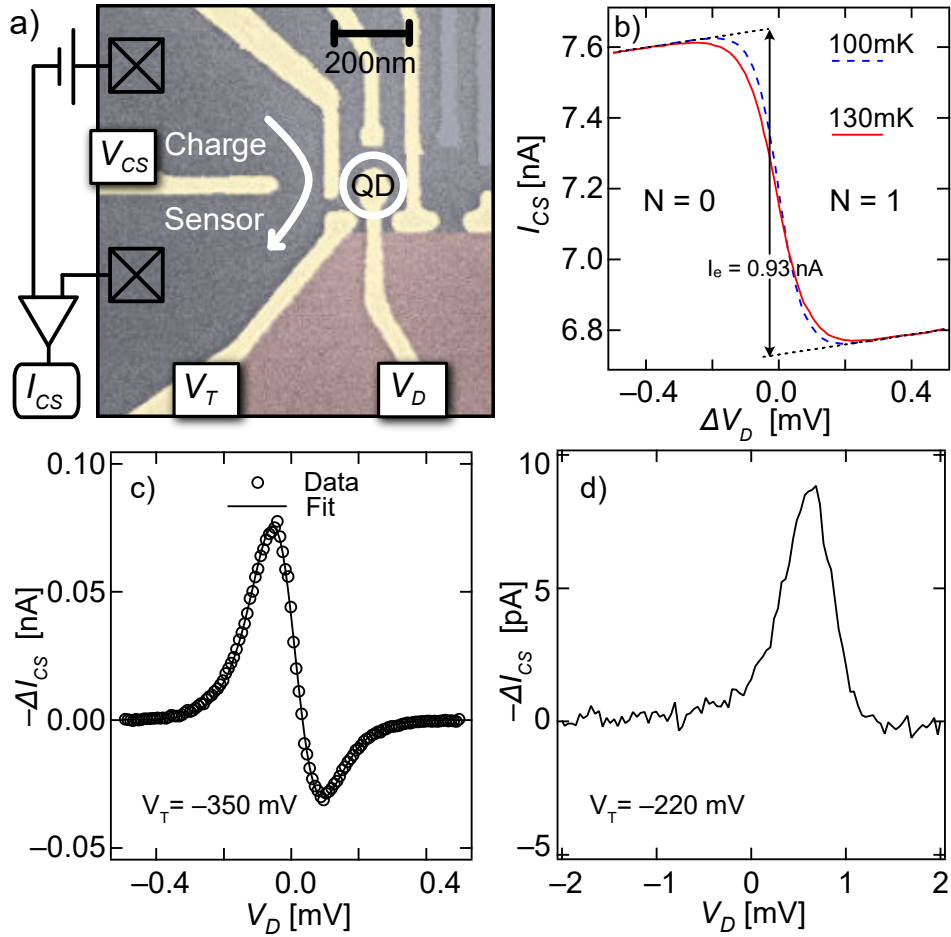


Figure 6.1: (a) Scanning electron micrograph of the device. Electrostatic gates (gold) define the circuit. Squares represent ohmic contacts to the 2DEG. The thermal electron reservoir (red) was alternated between base and elevated temperatures. (b) Current through the charge sensor, I_{CS} , for the $0 \rightarrow 1$ charge transition in a weakly coupled regime, separated into the unheated (100mK) and heated (130mK) parts of the interlaced measurement [146], showing the single electron step height I_e . (c and d) Change in I_{CS} from 100 to 130 mK, for weak (panel c) and strong (panel d) coupling between QD and reservoir. Panel c includes a fit to weakly-coupled theory.

6.2. Methods

Figure 6.1b illustrates weakly coupled $N = 0 \rightarrow 1$ transitions at $T = 100$ mK and $T + \Delta T = 130$ mK. Throughout this work both T and $T + \Delta T$ were calibrated by fitting to thermally broadened charge transitions; except where noted, $T = 100$ mK with $\Delta T \sim 30$ mK. As described in Chapter 4, the measurements at T and $T + \Delta T$ were interlaced by alternated Joule heating at 25 Hz.

Figure 6.1c shows the change in detector current from 100 to 130 mK, $\Delta I_{CS}(V_D) \equiv I_{CS}(T + \Delta T, V_D) - I_{CS}(T, V_D)$, scanning across the $0 \rightarrow 1$ transition in the weakly coupled regime. Note that $-\Delta I_{CS}$ is plotted instead of ΔI_{CS} in order to connect visually with ΔN , which increases when I_{CS} decreases. As in Ref. [8], the lineshape of $\Delta I_{CS}(V_D)$ in Fig. 6.1c may be fit to a non-interacting theory for thermally-broadened charge transitions to extract the change in entropy across the transition, ΔS_{fit} , not requiring calibration factors or other parameters (see Ref. [8] for details). For the data in Fig. 6.1c, this yields $\Delta S_{\text{fit}} = (1.02 \pm 0.01)k_B \ln(2)$, where the uncertainty reflects standard error among 5 consecutive measurements at slightly different V_T .

The limitation of this approach is illustrated by the very different lineshape in Fig. 6.1d, reflecting the $0 \rightarrow 1$ transition when the QD is strongly coupled to the reservoir. Fitting the data in Fig. 6.1d to thermally-broadened theory would yield a meaningless (and incorrect) $\Delta S_{\text{fit}} > 10k_B \ln(2)$ for the entry of the spin-1/2 electron. For a quantitative extraction of entropy beyond the weakly-coupled regime of Fig. 6.1c, we instead follow the integral approach in Eq. 3.12 that makes no assumptions on the nature of the quantum state and is additionally continuous across the transition rather than a single value for the complete $N = 0 \rightarrow 1$ transition.

Before moving to the quantitative evaluation of entropy, we note that the different lineshapes of $\Delta I_{CS}(V_D)$ in Figs. 6.1c,d – the peak-dip structure in Fig. 6.1c contrasting with the simple peak in Fig. 6.1d – can be understood as representing two temperature regimes for the Anderson impurity model. Figure 6.1c represents the high-temperature limit, where dN/dT is approximately a measure of the energy derivative of the density of states in the QD, and thus exhibits positive and negative lobes. At sufficiently low tempera-

6.2. Methods

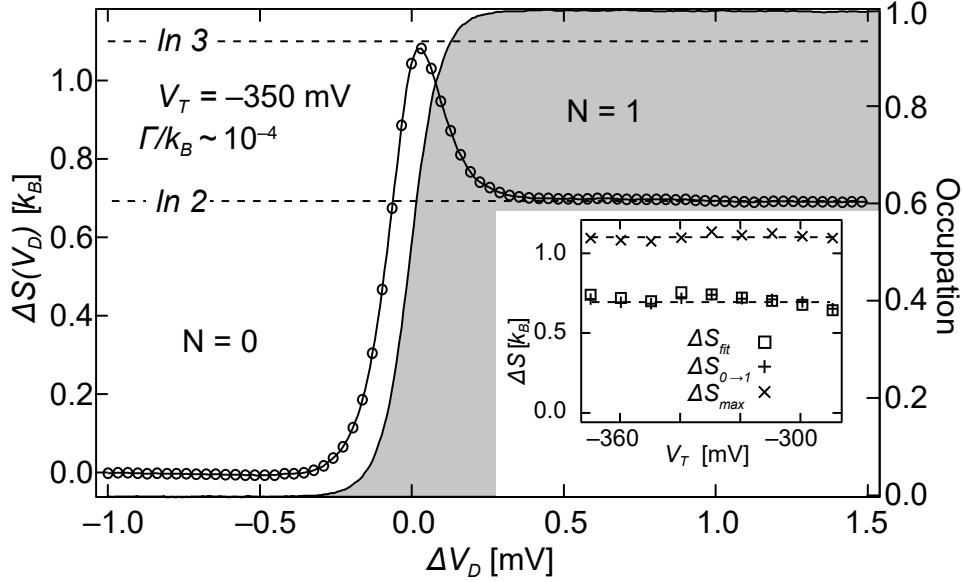


Figure 6.2: Change of S in the QD across the $N = 0 \rightarrow 1$ transition, obtained by integrating $\Delta I_{CS}(V_D)$ (Fig. 6.1c) following Eq. 3.12. Dot occupation across the transition is shown in grey. Data obtained in the weakly coupled limit, $V_T = -350$ mV corresponding to $\Gamma/k_B T \sim 1 \times 10^{-4}$. $\Delta S_{0 \rightarrow 1} = (0.99 \pm 0.02)k_B \ln(2)$ is the net change ΔS across the complete transition. Inset: comparison of ΔS_{fit} , $\Delta S_{0 \rightarrow 1}$, and ΔS_{max} (see text) for V_T covering approximately $10^{-5} < \Gamma/k_B T < 10^{-1}$.

tures, the exact solution [165], and the resulting Fermi liquid theory [166] predict a positive dN/dT for all values of the dot energy, from the empty level to the Kondo regime through the mixed-valence regime, with a peak expected at a dot energy corresponding to $T_K(\epsilon) \sim T$, where the entropy is expected to crossover from $S = 0$ to $S = k_B \ln(2)$. Figure 6.1d, corresponding to a measurement where $T \ll \Gamma$, demonstrates such all-positive dN/dT .

Following the same procedure as discussed in Chapter 4, the evaluation of Eq. 3.12 from experimental data starts with the approximation of $dN(\epsilon)/dT$ by the ratio $\Delta N(V_D)/\Delta T = -\Delta I_{CS}(V_D)/(I_e \Delta T)$. ΔT is expressed in units of gate voltage using the corresponding lever arm so that the integral may

6.3. Analysis

be evaluated over V_D , giving $\Delta S(V_D)$.

Figure 6.2 shows the entropy change across the $N = 0 \rightarrow 1$ charge transition in the weakly coupled regime calculated from the data in Fig. 6.1c, very similar to that in Chapter 4. The net change in entropy from beginning to end, $\Delta S_{0 \rightarrow 1} = (0.99 \pm 0.02)k_B \ln(2)$, is nearly identical to the $\Delta S_{\text{fit}} = (1.02 \pm 0.01)k_B \ln(2)$ from Fig. 6.1c, despite different sources of error for the two approaches.

The inset to Fig. 6.2 compares the fit and integral approaches for weakly-coupled charge transitions covering four orders of magnitude in Γ , tuned by V_T (see Fig. 6.5b inset for calibration of Γ). The consistency between $\Delta S_{0 \rightarrow 1}$ and ΔS_{fit} over the full range of weakly-coupled V_T , in addition to the fact that ΔS_{max} remains $k_B \ln(3)$ throughout this regime, confirms the accuracy of the integral approach. Small deviations from $\Delta S_{0 \rightarrow 1} = \Delta S_{\text{fit}} = k_B \ln(2)$, such as that seen around $V_T = -330$ mV, are repeatable but sensitive to fine-tuning of all the dot gates; we believe they are due to extrinsic degrees of freedom capacitively coupled to the dot occupation, such as charge instability in shallow dopant levels in the GaAs heterostructure (as described in Chapter 5).

After confirming the accuracy of Eq. 3.12 in the weakly coupled regime, we turn to the regime $\Gamma \gtrsim k_B T$ ($V_T > -280$ mV), where the influence of hybridization is expected to emerge. In other words, we repeat the same measurement protocol as we open up the tunnel barrier between the QD and reservoir by decreasing the negative potential on V_T .

6.3 Analysis

Before discussing the results of the strongly coupled regime, an understanding of the analysis procedures used is useful.

Each measurement of entropy presented in this chapter is, in fact, an average of many individual sweeps across the transition, as depicted in Fig. 6.3. The averaging of many sweeps is particularly important in the strongly coupled regime ($\Gamma > k_B T$) because the ΔI_{CS} signal becomes weaker as the transition becomes broader. In the weakly coupled regime, the transition

6.3. Analysis

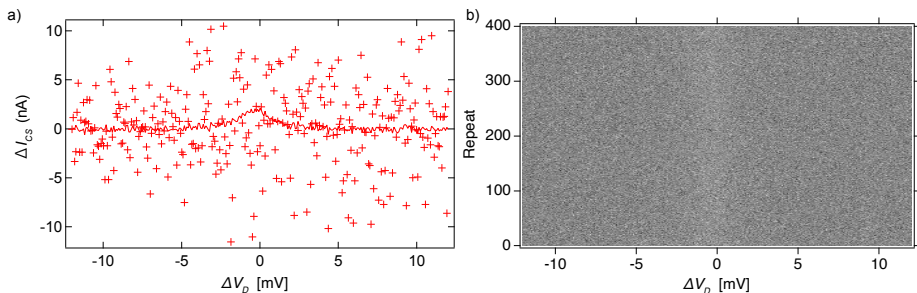


Figure 6.3: **(a)** Markers illustrate a single measurement across the charge transition, which takes 30 seconds to complete. No peak in ΔI_{CS} can be seen in this raw data. After averaging 400 of such scans together (solid line), however, a small peak in ΔI_{CS} is seen at $\Delta V_D = 0$. **(b)** Raw ΔI_{CS} data (greyscale) for 400 scans as in panel **a**. Averaged together, they yield the solid line in panel **a**.

width is dominated by thermal broadening, but for $\Gamma > k_B T$, the transition width is proportional to Γ . Because the magnitude of entropy change does not increase, but the transition spans an increasingly wide range of dot energies ϵ , the magnitude of dN/dT (and thus ΔI_{CS}) naturally decreases.

In the strong coupling regime, it was often necessary to measure the charge sensor signal over a single charge transition for tens of minutes or even hours to obtain a reasonable signal-to-noise ratio. Fig. 6.3a illustrates the terrible signal-to-noise ratio of a 30s measurement sweep. However, the presence of charge instability makes single slow measurements over the transition unreliable. By repeatedly sweeping over the transition quickly, then aligning each sweep based on a fit to the I_{CS} data before averaging, we can improve the signal-to-noise ratio of the corresponding ΔI_{CS} whilst mitigating the effect of charge instability. The alignment of data is exclusively based on the unheated parts of the I_{CS} measurement as it is crucial that no artificial shift between the heated and unheated parts of the data be introduced, otherwise, the conversion to entropy via Eq. 3.12 will be compromised.

For the most strongly coupled measurements ($V_T \geq -230$ mV), the very broadened charge transitions result in an uncertainty in the center parameter

6.3. Analysis

of the fit that exceeds that of the typical charge noise of the system; as a result, these data were averaged without centring first. The charge noise in the system (determined in the weakly coupled regime) typically causes sudden changes in dot energy $\Delta\epsilon \lesssim 6 \mu\text{eV}$ without significant long-term drift seen in the data. However, given that the transition width of measurements in the $V_T \geq -230 \text{ mV}$ regime is on the order of $400 \mu\text{eV}$, the lack of centring is expected to have a negligible effect. Occasional larger jumps in dot energy did occur on a timescale of hours; care was taken never to average data across such jumps.

To make a quantitative comparison between theory and experiment, we compare to DM-NRG simulations [140], [141] as described in Section 3.3. These calculations yield N as a function of T and ϵ_0 , where $-\epsilon_0$ is the depth of the dot level ϵ below the reservoir chemical potential μ . From $N(T, \epsilon_0)$, dN/dT and thereby ΔS are extracted via Eq. 3.12. To make a direct comparison with the experiment, $\Delta\epsilon_0 \equiv \epsilon_0 - \epsilon_0(N = 1/2)$ is defined like ΔV_D , centred with respect to the charge transition.

In the calculations, our collaborators assumed infinite interaction U , a constant density of states in the reservoir with bandwidth $D = 1$ exceeding all other energy scales, and kept 350 states per iteration with discretization constant $\Lambda = 2$. Note that the U in this case differs from that discussed in Chapter 5: here, it represents the Coulomb repulsion between electrons in the single QD (charging energy). Thus, an infinite U limits the QD occupation $0 \leq N \leq 1$ in the NRG simulation. The NRG results are given in arbitrary units of energy. Our collaborators note that the NRG curves are independent of the values of bandwidth W and of U as long as $U, W \gg T, \Gamma$ because, as with the experimental plots, all curves are shifted such that $x = 0$ corresponds to half filling.

NRG parameters are calibrated to match those in the measurements by aligning the occupation $N(\Delta\epsilon_0)$ with the measured $N(\Delta V_D)$, from which the appropriate Γ/T calculation may be selected and the precise connection between $\Delta\epsilon_0$ with ΔV_D is ensured. The procedure for fitting the occupation N of NRG calculations to measured data involves three additional steps before typical fitting procedures can be applied:

6.3. Analysis

- We linearly interpolate the 2D array of NRG calculations for Occupation N
- Add terms (amplitude, constant, linear) to account for the behaviour of the charge sensor in detecting the QD occupation
- Allow for an offset and scaling proportional to Θ (T in units of gate voltage) in the ϵ_0 axis

For a more thorough demonstration of NRG fitting, see Appendix A. Also note that, in the above procedure we effectively modify the NRG data to match measurement by adding terms to the NRG calculation. This is somewhat counter-intuitive when considering the aim is to compare data to theory. The choice is arbitrary and chosen this way around to visually match what the experimentalist is accustomed to observing in data. It would, of course, be exactly equivalent to subtracting the additional terms from the data to match the NRG occupation directly. In either case, the parameters of fitting are identical.

We fit the modified calculations to data using Powell’s method of minimization [167] to find the best fitting parameters, allowing all parameters to vary with the exception of Γ and Θ , for which only one is allowed to vary. In the weakly coupled regime, it is reasonable to approximate $\Gamma \sim 0$, and with that constraint, we can determine $\Theta(V_D)$. Repeating this fitting procedure for varying V_T (maintaining $\Gamma \sim 0$), we find a linear relationship between $\Theta(V_D)$ and V_T . Given that it is the lever arm α that connects Θ in units of gate voltage to temperature T in kelvin via

$$\alpha\Theta = k_B T, \tag{6.1}$$

and that we are very confident that the temperature T of the system is constant within $\sim 1\%$, the linear relationship between $\Theta(V_D)$ and V_T implies a linearly changing lever arm (Fig. 6.4).

As the lever arm α is a measure of the strength of effect the plunger gate V_D has on the QD energy, the linear change implies that as V_T is varied, the effect V_D has on the QD energy also varies. We attribute this to a change

6.4. Results

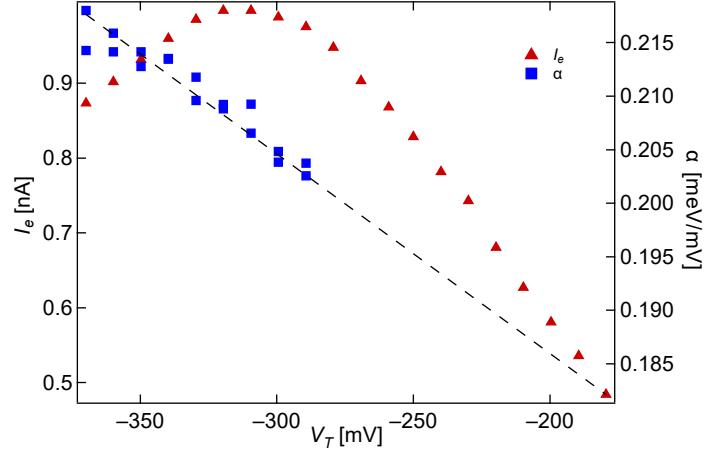


Figure 6.4: Variation of lever arm α , and charge step I_e measured independently over the full range of V_T explored in this experiment. Dashed line: extrapolation of α into the strongly-coupled regime where it cannot be measured directly

of shape of the QD that results in the charge moving further from V_D for more positive V_T .

For measurements into the strongly coupled regime (more positive V_T) where $\Gamma \gg 0$, we force the Θ parameter to follow the linear relationship found in the weakly coupled regime, allowing Γ to be a varying parameter. The fit parameters found by comparing N of NRG calculations to I_{CS} of measured data can then be used to directly compare between the NRG dN/dT calculations and ΔI_{CS} measurements. As seen in Fig. 6.5b, the data/theory agreement in terms of dot occupation N is within the experimental resolution, giving confidence that measured and calculated ΔS may be compared directly.

6.4 Results

If we now apply the above analysis to the measurements taken as the coupling Γ is increased between the QD and reservoir, we obtain the data summarized in Fig. 6.5. This figure shows the crossover from $\Gamma \ll k_B T$ to

6.4. Results

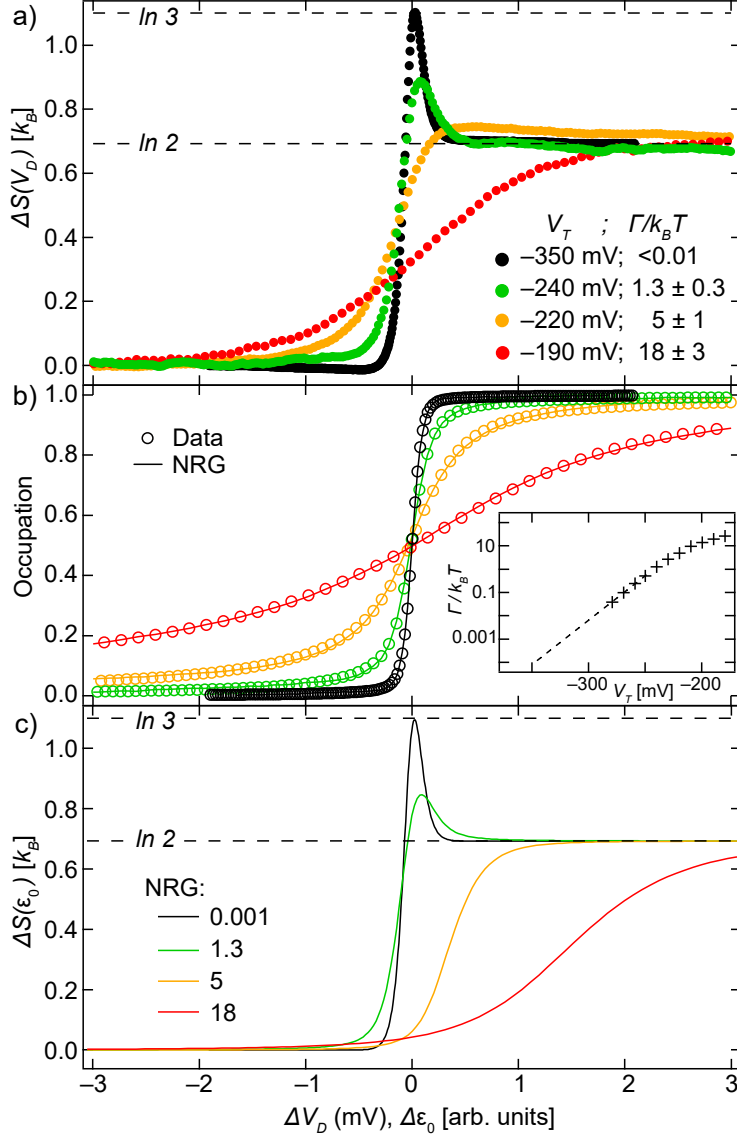


Figure 6.5: Evolution of $S(\epsilon)$ from the weak (black) to strong (red) coupling regimes, comparing data (a) to NRG calculations (c). Measurements of occupation across the charge transition are fit to NRG (b), leaving no free fit parameters for the $S(\epsilon_0)$ calculation. Panel b inset: Coupling strength of the QD to the reservoir, $\Gamma/k_B T$, extracted from fits, across the full range of V_T . Values $\Gamma/k_B T \ll 1$ cannot be measured directly and are extrapolated (dashed line).

6.4. Results

$\Gamma \gg k_B T$, illustrating several qualitative features. The $k_B \ln(3)$ peak in $\Delta S(\epsilon)$ decreases with Γ until no excess entropy is visible at the charge degeneracy point for $\Gamma/k_B T \gtrsim 5$ (Fig. 6.5a). This suppression of the entropy associated with charge degeneracy originates from the broadening by Γ of the $N = 1$ level due to hybridization with the continuous density of states in the reservoir [11]. At the same time, the total entropy change $\Delta S_{0 \rightarrow 1}$ remains $\sim k_B \ln(2)$ over the entire range of Γ explored in this experiment, reflecting the entropy of the spin-1/2 electron trapped in the QD.

Figure 6.5c illustrates NRG predictions for $\Delta S(\epsilon_0)$ over the range of Γ accessible in our measurements. Matching the data, the peak in entropy due to charge degeneracy is suppressed for $\Gamma > k_B T$, while the net entropy change across the transition remains $k_B \ln(2)$. At the same time, a qualitative difference between data and NRG is the shift to the right seen in NRG curves for higher Γ (Fig. 6.5c), but not observed in the measurements (Fig. 6.5a). This relative shift of NRG with respect to data is not explained by an offset of $\Delta \epsilon_0$ with respect to ΔV_D , as the two are aligned by the occupation data (Fig. 6.5b).

Instead, the shift of NRG curves to the right (toward higher occupation) with increasing Γ is explained by the virtual exchange interactions underlying the Kondo effect, which form a quasi-bound singlet state between the localized spin and a cloud of delocalized spins in the reservoir at temperatures below T_K . This state has no magnetic moment [105] and, in the case of a single-electron QD, zero entropy. Thus, due to the Kondo effect, we expect the entropy to remain zero for all dot energies that obey $T < T_K(\epsilon_0)$.

In Section 3.2, I described a situation in which we would expect the entropy of the system to remain zero even with $N = 1$ (not only near charge degeneracy). The reason that $S = 0$ for $N = 1$ is not expected for these measurements (or NRG simulations) is that even the largest Γ explored here is not large enough to result in $T_K > T$ in the deep Kondo regime (far from charge transitions). However, scaling theory predicts that when the energy level of the QD is far below that of the Fermi level, the Kondo temperature

6.5. Discussion

T_K depends exponentially on the depth of the level [113], [168]:

$$T_K = \frac{\sqrt{\Gamma U}}{2} e^{\pi \epsilon_0 (\epsilon_0 + U) / \Gamma U} \quad (6.2)$$

Although it is not technically correct to apply this formula in the mixed valence regime ($\epsilon \sim 0$), qualitatively it implies that T_K will increase significantly toward the mixed valence regime [113]. Therefore, we expect the onset of $k_B \ln(2)$ entropy to shift to larger values of ϵ as Γ increases, as seen in the NRG results.

The reason that we do not measure in the deep Kondo regime is that for the present device geometry, ΔI_{CS} collapses with increasing Γ , limiting the strength of the coupling accessible in the measurement to $\Gamma/k_B T \lesssim 25$.

6.5 Discussion

It remains a puzzle why the strong suppression of entropy right at the charge transition, seen in NRG calculations for $\Gamma/k_B T \geq 5$, is not observed in the data. One possibility is that the charge measurement itself leads to the de-phasing of the Kondo singlet [133], [150], [151]. In fact, Ref. [133] reported a suppression of the Kondo conductance peak due to charge sensing. However, despite finding a $30\times$ stronger de-phasing than had been predicted theoretically at the time, the magnitude of the suppression they found, even with significantly higher charge sensor bias (1200 μV), was $\sim 10\%$ [133], and therefore unlikely to explain the discrepancy that we see. Nevertheless, we tested for charge sensor dephasing in our measurement by repeating the measurement with charge sensor biases from 300 μV down to 50 μV , but no dependence on the bias as seen in the data (Fig. 6.6).

We note that the entropy measurement presented here is the first that could be sensitive to the dephasing of the Kondo state itself, rather than the dephasing of transport through the Kondo resonance [151].

6.5. Discussion

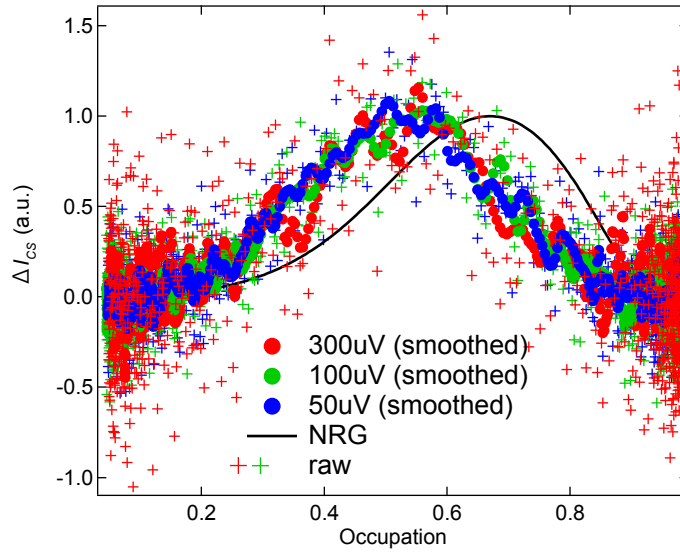


Figure 6.6: The lineshape of ΔI_{CS} , here plotted vs occupation instead of V_D , shows no dependence on V_{CS} within experimental noise, though of course the magnitude of I_{CS} and ΔI_{CS} scales linearly with V_{CS} . The case of $\Gamma/k_B T = 24$ is shown here. In particular, ΔI_{CS} remains peaked at $N \sim 0.5$, in contrast to the NRG calculation (solid line) in which the shifted peak reflects the screening of spin entropy in the mixed valence regime due to the formation of the Kondo singlet

Chapter 7

Preliminary entropy measurements in the Kondo regime

The measurements presented in this chapter extend upon those discussed in Chapter 6. Where the previous chapter was experimentally limited to investigation of the Kondo effect in the mixed-valence regime, here we discuss a new approach that should allow for entropy measurement of the Kondo effect into the more typical Kondo regime that many previous conductance measurements have focused on. The data presented here is preliminary, but indicative of a promising approach for further investigation.

7.1 Introduction

The discrepancy between measurement and NRG discussed in Chapter 6 calls for a more comprehensive investigation of the use of entropy measurements to probe the Kondo effect. Although the measurements of the previous chapter were expected to show significant indications of the Kondo effect, they were carried out with weaker coupling (smaller Γ/T ratio) than, to our knowledge, has been measured via conventional conductance measurements.²¹

This makes it difficult to argue that our measurements definitively indicate an inconsistency in the NRG simulations of entropy, especially given that NRG simulations of conductance are in good agreement with existing

²¹There are existing conductance measurements in the mixed-valence regime, such as Ref. [113], however, they were closer to the Kondo regime due to a larger Γ/T ratio.

7.2. Device Design

measurements that have been made closer to the Kondo regime. Ideally, we would like to make entropy measurements in a regime that has been extensively studied via conductance measurements.

The major problem with further exploration of the Kondo effect via the approach in Chapter 6, is the discrepancy between requiring a very strong coupling to increase the Kondo temperature of the system, while at the same time, requiring a relatively weak coupling so that we obtain a significant charge sensor signal. Therefore, we require a new approach that allows us to control parameters affecting these requirements independently. The key aspect to this new approach is to separate the coupling through which Kondo correlations form, from the coupling through which charge is added to the full system, such that they can be controlled independently. This chapter describes a device and measurement procedure that facilitates such control, and thus, allows entropy measurements to be made in a regime that can be more directly compared to existing conductance measurements.

7.2 Device Design

For the design of this new device, several requirements had to be satisfied simultaneously to enable a series of planned experiments, including the entropy measurements discussed in this chapter. In this section, the design considerations that are relevant to the measurements presented in this chapter will be described.

Figure 7.1 depicts the device. Where the charge sensed QD of the device measured in the previous chapter had a single coupling to the thermal reservoir, we now want an additional coupling to a separate reservoir so that we can separate where charge is added to the system from where the Kondo correlations occur. Instead of coupling the QD to a second lead (as is the case in typical conductance devices), we coupled the QD to a big dot (BD) with an area $\sim 4 \mu\text{m}^2$, as seen in Fig. 7.1d.

Because the BD is relatively large, its orbital level spacing $\Delta \ll k_B T$, and therefore, it effectively has a continuous (metal-like) density of states (like a regular lead). However, the finite size maintains a charging energy

7.2. Device Design

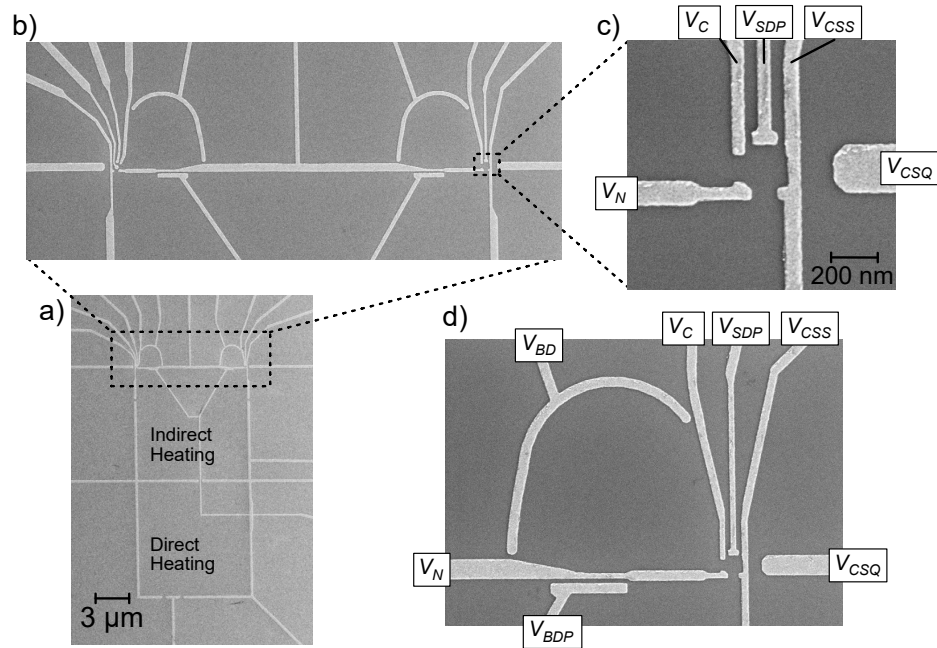


Figure 7.1: Scanning electron micrographs (SEMs) of the measured device. (a) The full device with the typical two-chamber heating reservoirs discussed in Chapter 4. (b) Two SD–BD devices that are close to identical in design. Measurements discussed in this chapter were taken using the right side QDs, also shown in panel d. (c) A close-up of the small dot only. Gates around the QDs are labelled, where V_C primarily controls the SD–BD coupling, V_{SDP} is the SD plunger, V_{CSS} and V_{CSQ} form the charge sensor QPC, V_N controls both SD–reservoir and SD–BD coupling, V_{BD} forms the big dot, and V_{BDP} acts as the BD plunger.

7.2. Device Design

$E_C > k_B T$ that results in the quantization of the occupation of the BD. The idea is that, when the BD is coupled to the SD and tuned to a fixed occupation ($\epsilon_{BD} \approx \epsilon_{SD}, E_F$), it will behave like a regular reservoir in terms of Kondo correlations, but without allowing charge transitions with the SD. Thus, charge transitions for the SD (and more generally, the full SD–BD system) are mediated only by the coupling of the SD to the thermal reservoir, a coupling that can be kept weak. Note that the addition of a second tunnel barrier to the small QD requires that the enclosed area be made smaller to allow reaching the single occupation regime (that, as previously discussed, is convenient for both experimental and theoretical considerations). The area was reduced from $\sim 40 \text{ fm}^2$ to $\sim 35 \text{ fm}^2$ as a result.

The V_C gate was designed to primarily control the SD–BD coupling, and the V_N gate was designed to control both the SD–BD and SD–reservoir couplings. While it would have been simpler to have a dedicated gate for controlling the SD–reservoir coupling, we faced practical constraints. The cryostat has a maximum wiring capacity of 24 lines, and there is also a risk of fabrication defects. Given these limitations, we opted to minimize the number of gates, accepting some additional complexity in the measurement process. It should be emphasized that we typically do not use V_{CSS} to control the SD–reservoir coupling due to its disproportionately large effect on both the QD energy and the charge sensor QPC.

For the purposes of the entropy measurements discussed in this chapter, the V_{BDP} gate acted as the fine-tune plunger gate for the BD.²² The V_N gate that separates the V_{BDP} gate from the BD area causes a screening effect that weakens the lever arm of V_{BDP} on the BD energy – a beneficial side effect, given that we require very fine control of the energy of the BD. Of course, the V_{BD} gate can also act as a plunger for the BD, but given its enormous size, it has an extremely strong lever arm that makes it suitable only for coarse tuning of the BD energy.

Consistent with the previous entropy measurement devices, we used the two-chamber heating reservoirs as previously discussed, although in this

²²Its primary purpose was for a different experiment where it would serve as a gate that can un-deplete a local region of 2DEG that is otherwise depleted by the V_N gate.

7.3. Methods

case, we sneaked the V_{BDP} gate out through the QPCs of the heater reservoirs. Because the V_{BDP} gate was used for fine-tuning control and its potential was kept close to zero, it had a negligible effect on the heater QPCs. As in previous cases, we had a charge sensor adjacent to the entropy sensing SD, this time with a wider V_{CSQ} gate that potentially increases the charge sensor sensitivity.²³

7.3 Methods

The device was cooled from room temperature to base temperature (cryostat ~ 8 mK, electron ~ 25 mK) with $+200$ mV applied to most gates, excluding: all heater gates, V_{BDP} , and V_{BD} .²⁴ This locks in an equivalent -200 mV bias under each gate that adds to any additional potential applied (discussed in Section 2.6). Compared to previous measurements where we typically measured at 100 mK (a temperature at which the 2DEG electrons and cryostat are in thermal equilibrium), here we typically measured at the lowest temperature possible to maximize the regime in which $T < T_K$. As discussed in Section 2.5, while the cryostat reaches a base temperature < 8 mK, the electrons reach thermal equilibrium at ~ 25 mK as a result of the weakening electron-phonon interaction ($\propto T^5$) [58] and presence of electrical noise that is not filtered out in the cryostat wiring.

As shown in Fig. 7.2a, we first tuned the device to a regime where both the SD-reservoir and SD-BD couplings were weak, the SD was minimally occupied ($0 \leq N \leq 1$), and the BD was occupied by many electrons. Similar to the double dot measurements of Chapter 5, the charge transitions of the big dot had a much smaller effect on the charge sensor due to the increased distance and screening between it and the charge sensor. Here, the transitions of the BD were much more closely spaced as a result of the

²³Confirming whether the wider QPC gate helps with sensitivity is difficult as the precise behaviour of the charge sensor QPC varies significantly between cooldowns, presumably, due to the precise location of frozen-in dopants.

²⁴If we were only carrying out the experiment described here, the V_{BD} would also have been cooled with positive bias applied. In this case, we just applied a more negative bias to that gate to ensure the 2DEG beneath it was depleted.

7.3. Methods

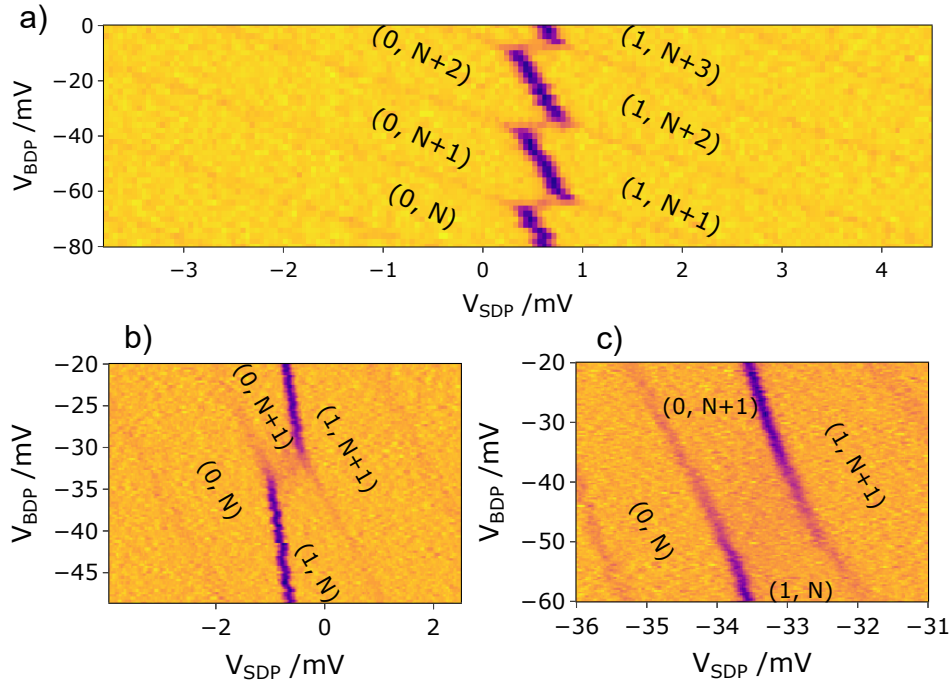


Figure 7.2: Charge stability diagrams with varying SD–BD coupling. The data represents charge sensor current differentiated in the horizontal axis. SD charge transitions occur at the more vertical features, and BD transitions at the faint more horizontal features. Occupations of the two QDs are shown as (N_{SD}, N_{BD}) . While the precise occupation of the SD is known, for the BD, only its relative occupation is known. (a) Weak coupling. (b and c) Increasingly strong coupling. Note that the SD–BD charge transitions broaden with increased coupling, while the SD–reservoir and BD–reservoir transitions remain thermally broadened due to the SD–reservoir coupling remaining weak.

7.3. Methods

much smaller charging energy that comes from the larger size of the dot. In contrast to the measurements discussed in Chapter 5, the regions of interest in these measurements are the charge transitions of the small dot *between* the transitions of the big dot – where the occupation of the big dot remains constant.

Because the big dot has a fixed occupation N_{BD} , the addition of an electron to the system is broadened only by the thermal distribution of electrons in the thermal reservoir and the strength of coupling between the small dot and reservoir; the strength of the coupling between the two dots does not affect the broadening of the charge transition of the full system. This allowed us to maintain the strong thermal dependence of the system that provides a strong charge sensor signal, even in the case that the SD and BD were strongly coupled to each other.

Figures 7.2**b,c** depict the charge stability diagrams of the double dot system with increasing coupling strength between the two dots (that is primarily controlled by V_C). As the coupling strength increases between the two dots, the region where charge exchanges between the two dots broadens, making the transition less visible in the charge stability diagrams. Note that the stronger coupling does not significantly broaden the charge transitions for either dot individually, as those transitions remain thermally broadened due to the weak coupling of the full system to the thermal reservoir via the SD–reservoir coupling. For very strong coupling between the two dots, the behaviour tends towards that of a single larger dot, as can be seen by the slope of the SD and BD charge transitions becoming more similar (Fig. 7.2c).

Crucially, there remains a strong localization of charge in the small dot, despite the very strong coupling between it and the BD. This can be seen by the fact that the differentiated charge sensor current signal remains strong when charge is added to the SD from the reservoir (in comparison to the BD–reservoir transitions). The strong localization of the charge in the small dot, along with the thermally broadened charge transitions, means that the charge sensor signal does not diminish for increased coupling. This holds even with much stronger SD–BD coupling than was achieved between the QD and reservoir in the mixed valence entropy measurements discussed in

7.3. Methods

Chapter 6.

However, the broadening of the SD–BD transition for increased coupling strength makes it difficult to distinguish the regions that correspond to charge transitions of the SD alone with N_{BD} fixed (in Fig. 7.2c, for example). This is a result of V_{SDP} similarly affecting the occupation of both the SD and BD in the strong coupling limit. In other words, the V_{SDP} gate couples to both the SD and BD energies. This poses a problem for the entropy measurement as it is crucial that the occupation only change in the small dot to be able to accurately convert the charge sensor signal ΔI_{CS} to dN/dT . Therefore, it is better to sweep over the SD transitions using a virtual gate that holds the BD energy (and therefore N_{BD}) constant. Such a virtual gate, SDP', was formed using the V_{SDP} and V_{BDP} gates. For a virtual gate that truly coupled *only* to the SD energy, we would have also needed to account for the effect V_{SDP} had on the SD–BD and SD–reservoir couplings. However, since it was only important that $\Gamma \lesssim k_B T$ for the SD–reservoir coupling (not a precise value of Γ), it was generally safe to ignore the effect V_{SDP} had on the SD–reservoir coupling. As for the SD–BD coupling, for these preliminary measurements, we were interested in the behaviour of qualitatively different coupling regimes: weak, medium, and strong. Therefore, as long as the SD–BD coupling did not change drastically during a sweep over the SD charge transition, it was an acceptable approximation to counteract the effect of V_{SDP} on the BD energy using V_{BDP} alone.

Figures 7.3a,b show a direct comparison between sweeping over the SD transition with and without the virtual gate. Both measurements were taken in the regime that the SD–BD coupling was weak, but in Fig. 7.3b, the use of the virtual SDP' gate results in BD transitions that lie parallel to the sweep axis. Because charge sensor data is differentiated in the x-direction for these charge stability plots, the BD transitions do not show up in the scans that utilize SDP', instead, dotted lines are added to mark where those transitions occur. For the data in Figs. 7.3c,d, the SD–BD coupling is made stronger by reducing the negative potential on V_C , roughly equivalent to data in Figs. 7.2b,c.

Entropy measurements were made over similar regions to those depicted

7.3. Methods

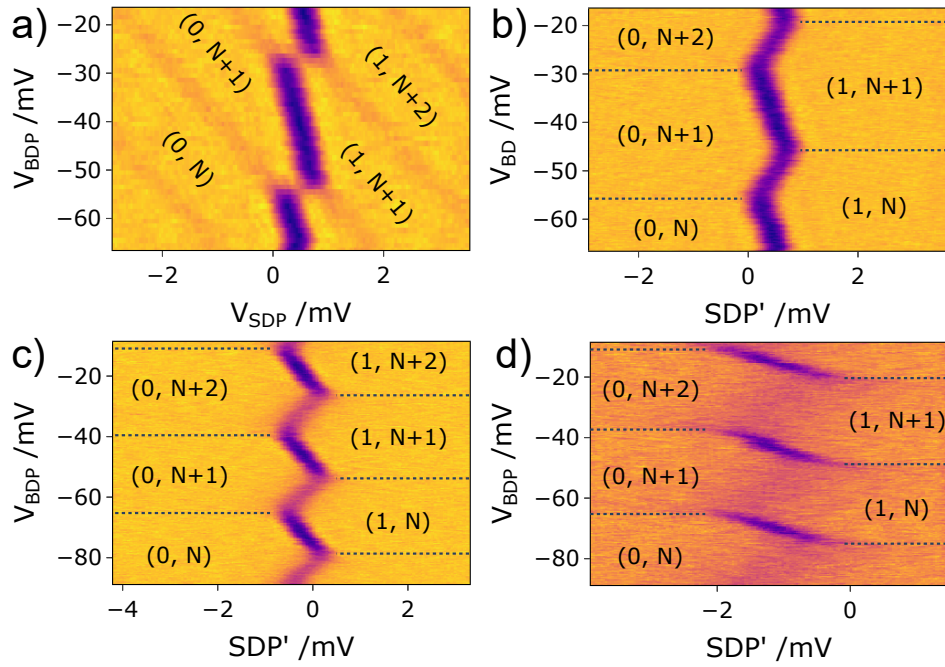


Figure 7.3: Differential charge sensor current charge stability plots with varying SD–BD coupling using the virtual SDP' gate for the x-axis, where the primary V_{SDP} values are shown in the axes. (a) Weak coupling data, taken without using a virtual gate, as a reference for the effect of virtual gating in all other panels. (b) Weak coupling (same as a except for the virtual gate). (c and d) Medium and strong coupling, respectively.

7.4. Results

in Fig. 7.3. Although we are primarily interested in the behaviour of the system between BD transitions, it was necessary to perform 2D measurements that span BD transitions because of slow drifts in the BD energy over time. In other words, the V_{BDP} potentials that correspond to places where the BD occupation is between transitions, vary over time, so we must measure over a range of V_{BDP} to reliably collect data in the regimes of interest. Entropy measurements were made with similar parameters to those described in Chapter 4, with the notable difference being that T was oscillated from the base electron temperature (25 mK) to ~ 35 mK rather than 100 to 130 mK.

7.4 Results

In the entropy measurements of the SD–BD system, we are primarily interested in the entropy change of the system at SD–reservoir transitions; when the BD’s occupation and entropy remain constant. This is in contrast to the measurements of Chapter 5 where the interesting behaviour occurred when the occupation of both QDs changed during the measurements. Specifically, we are hoping to observe the entropic effect of Kondo correlations forming in the system when the SD–BD coupling is made strong enough that $T < T_K$ in the Kondo regime. Note that, in the experiment described in Chapter 6, $T < T_K$ was only achieved in the mixed-valence regime, where T_K significantly increases close to the charge degeneracy point. Here, the ability to measure with much stronger SD–BD coupling means that we expect Kondo correlations to persist even as $N_{SD} \rightarrow 1$ (the Kondo regime).

Figure 7.4 depicts a summary of the entropy measurements over several BD transitions with weak and strong SD–BD coupling. For this preliminary data, the additional measurements necessary for conversion from ΔI_{CS} to dN/dT were inadequate; as a result, the entropy values are given in arbitrary units. As we do not have sufficient information to calculate the entropy values directly, we can instead compare the peak and final values for a crude estimation of the entropy behaviour of the system. The dashed black line represents the expected final entropy based on the observed peak, assuming

7.4. Results

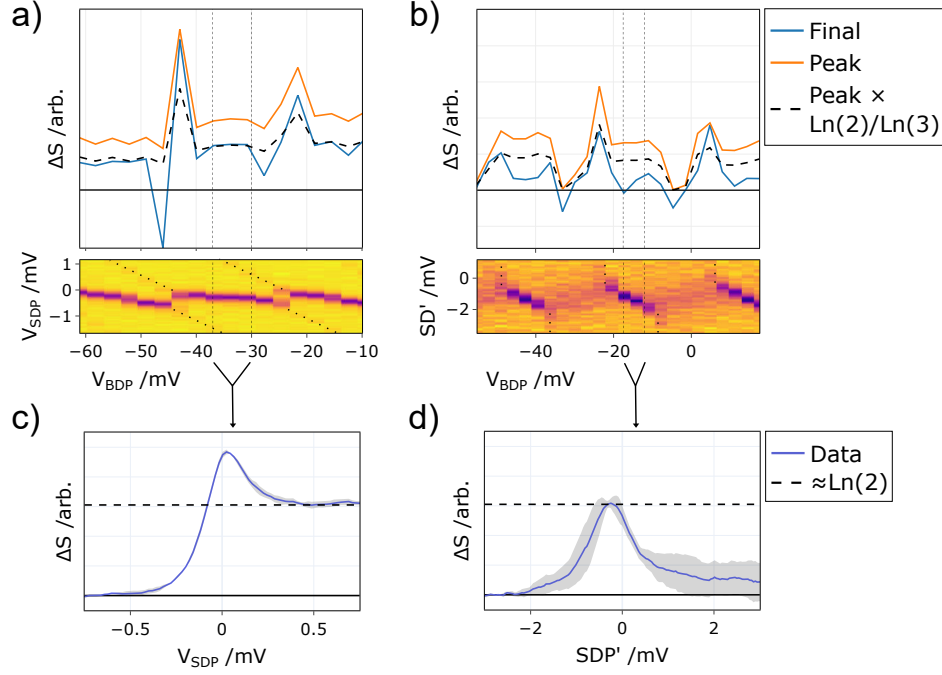


Figure 7.4: Summary of entropy measurements with weak (left) and strong (right) SD–BD coupling. (a and b) Peak and final entropy changes (in arbitrary units) over the SD transition, corresponding to vertical sweeps in the charge stability diagram below. Note that the axes of the charge stability diagrams are swapped in comparison to previous figures. (c and d) Full entropy measurements as a function of SD energy averaged over the regions indicated by vertical dashed lines in panel a and b. Arbitrary units are used for entropy change due to the lack of sufficient calibration measurements. The dashed lines in all but d indicate $\frac{\ln(2)}{\ln(3)} \cdot \Delta S_{\text{peak}}$. For d, the dashed line is the same as that in panel c (i.e. assuming the calibration factors are the same and the arbitrary values are comparable, however, this may not be the case).

7.4. Results

an $\frac{\ln(2)}{\ln(3)}$ ratio that we would expect for the addition of the first electron to a simple weakly coupled QD. Under each entropy summary, a charge stability diagram that corresponds to the location of the entropy measurements is included. Note that the axes on these charge stability diagrams are swapped in comparison to Figs. 7.2 and 7.3: the SD transition is the near-horizontal feature, and the BD transitions are marked with dotted lines.

To confirm that the system behaves as we expect without Kondo correlations, let us first look at the case where SD–BD coupling is weak in Figs. 7.4a,c.²⁵ With weak coupling, the presence of the big dot should have a negligible effect on the total entropy change of the system when the BD does not undergo a charge transition itself. To elaborate, we do not expect Kondo correlations to form between the SD and BD as $T_K \ll T$ for weak coupling, and for constant N_{BD} the entropy of the BD is assumed to remain constant. For $-40 \text{ mV} < V_{BDP} < -30 \text{ mV}$ in Fig. 7.4a, the entropy measurements correspond to change in SD occupation alone. The full entropy change data in this region is averaged to obtain the data in Fig. 7.4c. As expected, Fig. 7.4c closely resembles the weakly coupled entropy transition shape seen in previous chapters, with the final entropy change matching the expected value for a weakly coupled QD (assuming the peak corresponds to $k_B \ln(3)$). For $V_{BDP} < -50 \text{ mV}$ and $V_{BDP} > -15 \text{ mV}$ in Fig. 7.4a, where $N_{BD} = N - 1, N + 1$ respectively, we also see good agreement with expectation for the total entropy change. Around $V_{BDP} = -15$ and -25 mV we see a significant deviation in the measured entropy as a result of the additional contribution of the BD charge transitions (similar to Chapter 5).

Now, if we compare to the case of strong SD–BD coupling, shown in Figs. 7.4b,d, we see a crucial change in behaviour. For $-17.5 \text{ mV} < V_{BDP} < -12 \text{ mV}$ in Fig. 7.4b, the BD’s occupation is again fixed, however, the final entropy change is now significantly below that expected for a spinful electron in a QD. Indeed, Fig. 7.4d indicates that the entropy increases at the transi-

²⁵Note that the weakly coupled measurements were taken by sweeping V_{SDP} rather than the SDP’ virtual gate, as a result, the BD transitions show up as diagonal lines. In this preliminary experiment, the measurement taken in the weak coupling regime after setting up the SDP’ gate failed. The effect on the entropy measurements is negligible.

7.5. Discussion

tion (due to charge degeneracy), but returns close to zero as $N_{SD} \rightarrow 1$. If the calibration factors between the weakly and strongly coupled measurements do happen to be similar, then we can also compare to the dashed line that indicates $k_B \ln(2)$ from the weakly coupled measurement. This would indicate that the entropy at the charge degeneracy point is $k_B \ln(2)$, as would be expected. Similar behaviour is seen for $-45.7 \text{ mV} < V_{BDP} < -39.4 \text{ mV}$ and $V_{BDP} > 8.0 \text{ mV}$ where $N_{BD} = N - 1, N + 1$. This is a hopeful sign that we are observing a system in which the spin-entropy of the QD is suppressed in favour of a Kondo singlet state.

7.5 Discussion

The significant decrease in entropy of the $N_{SDP} = 1$ system with strong compared to weak coupling is indicative of the formation of a correlated state that suppresses the spin-entropy one would otherwise expect in the small dot. However, it is important to note that the measurements presented here are preliminary. They were obtained, in a rush, at the end of a long experiment that had a different focus. Consequently, the results presented here lack some of the additional measurements and calibrations that are required to make strong statements about the validity of the findings. The intention of this chapter is to showcase the promising steps that have been made so far, with the expectation that a future experiment will be carried out to more thoroughly investigate the behaviours of the system.

Several additional measurements could render these results more compelling. First, the interpretation of the entropy changes would be more reliable with the necessary calibration factors (ΔT , α , and I_{amp}) to scale from charge sensor signal to entropy change in units of k_B . For example, it would be interesting to confirm the accuracy of the presumed $k_B \ln(2)$ peak in Fig. 7.4d. The lack of calibration factors here was mostly due to time constraints.²⁶ Because some gate potentials change significantly between the weak and strong coupling limits, it is prudent to take calibration mea-

²⁶Also, remaining brain power was running short at the end of a long and intense experiment.

7.5. Discussion

measurements at each set of device settings. While measurements are shown at only a few device settings here, in reality, many more were taken, and there was not enough time to collect all of the necessary information for all of the combinations of device settings measured.

To make a more quantitative comparison to, for example, NRG calculations, it would also be helpful to determine the SD–BD coupling strength quantitatively. This may prove somewhat challenging as the charge transitions between the SD and BD become increasingly difficult to measure accurately as the coupling strength increases (similar to the issues discussed in Chapter 6).

To confirm that the effect seen is in fact due to Kondo correlations, it would be interesting to repeat similar measurements at varying system temperatures. Such measurements should be relatively easy to carry out but would require a lot more time. In the analysis of such measurements, one could look for the characteristic $\ln(T)$ dependence of the Kondo effect. An in-plane magnetic field could also be used to suppress the Kondo effect via the Zeeman splitting of spin-degeneracy in the SD. Although, as the Zeeman splitting would naturally suppress spin-degeneracy itself, it may be difficult to extract useful information from such a measurement.

Another important consideration in the small dot big dot device is the thermal equilibration of the BD electrons. Because the BD is not directly tunnel coupled to the thermal reservoir, the process through which it thermalizes with it is not clear. In the measurements presented here, the SD–reservoir coupling was made as strong as possible while maintaining $\Gamma \lesssim k_B T$, assuming that the BD thermalizes via second-order processes through the SD. Because the entropy measurements are taken over SD transitions (where $\epsilon_{SD} \approx E_F$), the rate of virtual processes is expected to be high. On the other hand, the thermalization of the BD may occur via local electron-phonon coupling; the electrons in the thermal reservoir dissipate heat to the phonon lattice, which, in turn, could transfer heat to the nearby BD electrons. Further investigation would be beneficial.

More generally, continued experiments with a small dot coupled to a big dot are particularly intriguing: there is the potential to extend such mea-

7.5. Discussion

surements to systems that exhibit more exotic ground states, such as those influenced by a multi-channel Kondo effect [163], [169], [170]. The multi-channel Kondo effect is fascinating because it can lead to non-Fermi liquid behaviour [169]. Note, however, that simply coupling a QD to multiple infinite reservoirs (leads) is not sufficient to form a multi-channel Kondo state because the leads can freely exchange electrons with each other. This results in a single correlated state forming between all leads and the impurity QD. Conversely, with finite reservoirs that have fixed charge, electrons cannot transfer between them, resulting in separate Kondo correlations that each compete to screen the impurity QD spin. In fact, the device described here could be tuned to exhibit a two-channel Kondo effect by strongly coupling the SD to both the reservoir and the big dot. But, this would introduce the same issues for the charge sensor signal strength discussed in Chapter 6. Therefore, experimentally, it would be much easier to couple the SD strongly to two separate big dots, allowing the coupling of the full system to the thermal reservoir to be kept weak.

Chapter 8

Conclusion

8.1 Summary

In conclusion, a novel procedure for both measuring and analyzing entropy in mesoscopic systems has been developed and demonstrated on a variety of systems of increasing complexity.

The entropy measurement conducted on a quantum dot (QD) weakly coupled to a reservoir, as discussed in Chapter 4, proved the effectiveness of the new approach. These results not only confirmed the utility of the method but also exhibited its capability to evaluate entropy changes continuously throughout the charge transition. This alone represents a marked improvement over the foundational approach of Ref. [8], which permitted extraction of only the total entropy change. This proof-of-concept measurement was then used as the starting point for the following experiments.

In Chapter 5, the capacity of the device introduced in Chapter 4 to function as an entropy sensor for a capacitively coupled system is substantiated. The experimental findings are presented as that of a double QD system, closely matching theory calculations. Importantly, these results can also be interpreted as measurements of the non-local entropy of the second QD, attained through its capacitive coupling to the ‘entropy sensor QD’. To clarify, since the entropy change of the first QD is known, its contribution to the total measured entropy change can be accounted for, yielding an isolated measurement of the entropy change of the second, capacitively coupled QD. This is analogous to the approaches proposed by Sela et al. [11] and Sankar et al. [154] to measure the entropy associated with, a Majorana zero mode and topological entanglement of chiral topological phases, respectively.

In Chapter 6, the universality of the newly developed measurement tech-

8.2. Extensions of discussed measurements

nique is further validated. By establishing a strong coupling between the entropy sensor QD and the thermal reservoir, a non-trivial system emerges due to the hybridization of discrete QD states with the continuous spectrum of the reservoir. A comparison with density-matrix numerical renormalization group (DM-NRG) simulations corroborated the experimental findings, showing good agreement up to intermediate coupling strengths. Interestingly, a significant deviation between experiment and simulation was observed for stronger coupling, particularly where Kondo correlations are anticipated in the mixed valence regime. This discrepancy has raised questions that are yet to be resolved.

In Chapter 7, further exploration of a system manifesting Kondo correlations is described. A newly configured device, which integrates features from previous experiments, enables the measurement of entropy in a more strongly coupled regime than was previously attainable. With the stronger coupling, it is expected that $T_{\text{sys}} < T_K$ can be realized in the Kondo regime; thus, Kondo correlations should persist throughout the charge transition of the system. Preliminary measurements appear to indicate the suppression of spin entropy, suggesting the observation of the formation of a Kondo singlet.

While the measurements delineated in this work do not directly unveil new insights into exotic states, they establish a foundational methodology that holds significant promise for future studies aimed at elucidating a wide range of exotic quantum phenomena.

8.2 Extensions of discussed measurements

The methodologies and findings presented thus far serve as fundamental building blocks for further exploration of mesoscopic entropy measurements. The following section discusses potential extensions to these initial measurements.

In Chapter 5, the measurements presented were confined to the weak coupling regime. Although there existed a relatively strong Coulomb interaction between the two QDs, each was weakly tunnel-coupled to the reservoir, and no direct tunnel coupling existed between the QDs themselves. During the

8.2. Extensions of discussed measurements

time these measurements were conducted, initial explorations were made into the system's behaviour beyond the weak coupling limit. However, the absence of direct tunnel coupling between the two QDs proved to be a significant limitation. Given the concerns about system thermalization, this was a worthwhile trade-off for the device and the measurements presented here. For a future measurement, a very similar device featuring direct tunnel coupling between the two QDs could offer an intriguing platform for studying quantum states that require strong coupling: for example, the simplest case being the formation of a singlet state between the two QDs. In fact, such a device has already been fabricated but has yet to be measured.

Additionally, the double dot experiment can be seen as a step toward entropy measurement in more complex multi-dot systems (where the QD entropy probe can be one of the QDs). Multi-dot systems can be used to simulate different regimes of the Hubbard model [171], such as the recent implementation of Nagaoka ferromagnetism [164]. Entropy measurements in such systems would be fascinating.

In Chapter 6, the QD was connected to the reservoir through only one tunnel barrier, thereby precluding the possibility of taking more conventional conductance measurements for additional comparison to NRG simulations. It would be advantageous to investigate a system where both conductance and entropy measurements could be conducted simultaneously. Such an experimental setup could potentially shed some light on the source of the previously observed discrepancy between entropy measurements and NRG simulations. Indeed, the device introduced in Chapter 7 was conceived with this dual-measurement approach in mind. The gate serving as the big dot plunger was specifically designed to allow the small QD to be toggled between conductance and entropy measurements with minimal adjustments to its parameters.

As discussed in Section 7.5, the device utilized there offers several avenues for additional measurements aimed at scrutinizing Kondo correlations in greater detail. In addition, the device could theoretically be adjusted to manifest a two-channel Kondo effect. However, as previously mentioned, pursuing such an experimental regime would likely be more productive

8.3. Looking Forward

through an extension of the current device design.

8.3 Looking Forward

While the previous section focused on specific extensions of the measurement techniques discussed in this thesis, it is worth emphasizing the broader spectrum of opportunities for advancing this field of work. The following paragraphs will delineate various strategies to refine these measurements further and extend their applicability to a wider array of intriguing quantum systems.

Adopting higher bandwidth measurements would yield immediate improvements in noise performance. The damaging effect of charge noise offsetting the QD energy levels, which motivated the fast alternation between temperatures discussed in Section 4.3, is more severe in these entropy measurements than in a typical mesoscopic investigation. The need to control μ and ϵ at a sub-peV level forces the measurement to be performed at as high a frequency as possible given the experimental setup, and fundamental speed limitations involving heat capacity of electrons are at least several orders of magnitude above what was achieved in the present experiments [71].

Two more opportunities for improvement stem from the need to remain in thermal equilibrium for Maxwell relations to be applicable. The very act of charge sensing injects a non-equilibrium component into the system dynamics, in principle violating the starting requirement for Maxwell relations. This can be minimized by, first, reducing stray couplings between the sensor circuit and the device under test and, second, by reducing the noise of the charge sensing measurement itself. At the same time, the theoretical question of how much charge sensing is actually expected to affect dN/dT for a given system remains an important open avenue for study.

On a more practical note, the requirement for operation in thermal equilibrium is hard to meet in complex circuits when following the electron heating approach outlined in this thesis. The advantage of heating only electrons is that the heat capacity is minuscule, and temperatures can change rapidly as a result. The disadvantage is that the electronic system is then out of

8.3. Looking Forward

thermal equilibrium with the phonon lattice, so parts of a multi-component mesoscopic circuit that couple differently to the heated electronic reservoir and the phonon lattice may end up at different, and poorly defined, effective temperatures.

In the measurements detailed in Chapters 4, 5, and 6, thermal equilibrium was not a pressing concern. The systems – single electrons in quantum dots – easily achieve thermal equilibrium with the reservoir, even with the weakest of couplings. This is because there are no internal degrees of freedom (within $k_B T$) for the first electron in a ~ 200 nm diameter QD. However, for the device discussed in Chapter 7, thermal equilibration of the full system requires more careful consideration due to the indirect coupling of the ‘big dot’ to the thermal reservoir. Future experiments may transition away from the electron heating approach described here, opting instead for a more elaborate thermal circuit that maintains both electrons and lattice phonons in thermal equilibrium during the heating step. This will require careful design to ensure that the thermal coupling between the chip and cryostat is strong enough to keep the chip close to the base cryostat temperature while the heating is off, but weak enough to keep the chip in internal thermal equilibrium during the heating process. Ironically, the heating techniques employed in seminal studies of 2DEG heat capacity [67]–[69], which were discussed in Section 3.1.2, may find renewed relevance in the context of our entropy measurement protocol. While these early experiments lacked the precision needed to quantify entropy changes in few-electron systems, their heating methodologies could be well-suited for integration into our more sophisticated measurement and analysis techniques.

Numerous avenues exist for employing the entropy measurement technique developed in this thesis, especially with an adapted heating procedure, as discussed. Any system for which the ground state is modified by the occupation of the charge-sensed QD is a candidate – whether the QD is an integral part of the measured quantum system, or whether the QD affects a nearby quantum system of interest purely through capacitive coupling. Moreover, the applicability of this technique extends beyond the confines of 2DEGs in GaAs/AlGaAs heterostructures. It could be applied to a wide

8.3. *Looking Forward*

range of mesoscopic devices, such as layered graphene structures [81], [84], [86], [172], either through analogous gating techniques if the system hosts a 2DEG, or via external circuitry placed in close spatial proximity, as demonstrated by Rozen et al. [84]. This versatility underscores the broader relevance of the work presented herein and sets the stage for further explorations in the rapidly evolving field of quantum entropy measurements.

Bibliography

- [1] R. Clausius, T. Hirst, and J. Tyndall, *The Mechanical Theory of Heat: With Its Applications to the Steam-engine and to the Physical Properties of Bodies*. John Van Voorst, 1867.
- [2] P. Atkins and J. d. Paula, *Physical Chemistry: Thermodynamics, Structure, and Change*. W. H. Freeman, 2014, ISBN: 9781429290197.
- [3] C. A. Egan and C. H. Lineweaver, “A larger estimate of the entropy of the universe,” *The Astrophysical Journal*, vol. 710, no. 2, pp. 1825–1834, 2010, ISSN: 0004-637X. DOI: 10.1088/0004-637x/710/2/1825. eprint: 0909.3983.
- [4] C. E. Shannon, “A mathematical theory of communication,” *The Bell System Technical Journal*, vol. 27, no. 3, pp. 379–423, 1948, ISSN: 0005-8580. DOI: 10.1002/j.1538-7305.1948.tb01338.x.
- [5] G. H. J. Johnstone, M. U. González-Rivas, K. M. Taddei, R. Surtarto, G. A. Sawatzky, R. J. Green, M. Oudah, and A. M. Hallas, “Entropy Engineering and Tunable Magnetic Order in the Spinel High-Entropy Oxide,” *Journal of the American Chemical Society*, vol. 144, no. 45, pp. 20590–20600, 2022, ISSN: 0002-7863. DOI: 10.1021/jacs.2c06768. eprint: 2211.15798.
- [6] G. W. Drake, “Entropy,” *Encyclopedia Britannica*, Aug. 2023, Accessed 11 September 2023.
- [7] J. W. Gibbs, *Elementary principles in statistical mechanics developed with especial reference to the rational foundation of thermodynamics*. New York, C. Scribner, 1902, 1902.

BIBLIOGRAPHY

- [8] N. Hartman, C. Olsen, S. Lüscher, M. Samani, S. Fallahi, G. C. Gardner, M. Manfra, and J. Folk, “Direct entropy measurement in a mesoscopic quantum system,” *Nature Physics*, vol. 14, no. 11, pp. 1083–1086, 2018, ISSN: 1745-2473. DOI: 10.1038/s41567-018-0250-5. eprint: 1905.12388.
- [9] R. P. Feynman, *There’s Plenty of Room at the Bottom*, 1959.
- [10] S. Smirnov, “Majorana tunneling entropy,” *Physical Review B*, vol. 92, no. 19, p. 195312, 2015, ISSN: 1098-0121. DOI: 10.1103/physrevb.92.195312. eprint: 1507.00278.
- [11] E. Sela, Y. Oreg, S. Plugge, N. Hartman, S. Lüscher, and J. Folk, “Detecting the universal fractional entropy of Majorana zero modes,” *Physical Review Letters*, 2019. DOI: 10.1103/physrevlett.123.147702. eprint: 1905.12237.
- [12] N. R. Cooper and A. Stern, “Observable Bulk Signatures of Non-Abelian Quantum Hall States,” *Physical Review Letters*, vol. 102, no. 17, p. 176807, 2009, ISSN: 0031-9007. DOI: 10.1103/physrevlett.102.176807. eprint: 0812.3387.
- [13] K. Yang and B. I. Halperin, “Thermopower as a possible probe of non-Abelian quasiparticle statistics in fractional quantum Hall liquids,” *Physical Review B*, vol. 79, no. 11, p. 115317, 2009, ISSN: 1098-0121. DOI: 10.1103/physrevb.79.115317. eprint: 0901.1429.
- [14] G. Ben-Shach, C. R. Laumann, I. Neder, A. Yacoby, and B. I. Halperin, “Detecting Non-Abelian Anyons by Charging Spectroscopy,” *Physical Review Letters*, vol. 110, no. 10, p. 106805, 2013, ISSN: 0031-9007. DOI: 10.1103/physrevlett.110.106805. eprint: 1212.1163.
- [15] R. Dingle, H. L. Störmer, A. C. Gossard, and W. Wiegmann, “Electron mobilities in modulation-doped semiconductor heterojunction superlattices,” *Applied Physics Letters*, vol. 33, no. 7, pp. 665–667, 1978, ISSN: 0003-6951. DOI: 10.1063/1.90457.

BIBLIOGRAPHY

- [16] J. R. Schrieffer, “Mobility in Inversion Layers: Theory and Experiment,” in *Semiconductor Surface Physics*, [H. Kingston”], Ed., University of Pennsylvania Press, 1957, pp. 55–69, ISBN: 9781512803051. DOI: 10.9783/9781512803051-005.
- [17] M. J. Manfra, “Molecular Beam Epitaxy of Ultra-High-Quality AlGaAs/GaAs Heterostructures: Enabling Physics in Low-Dimensional Electronic Systems,” *Annual Review of Condensed Matter Physics*, vol. 5, no. 1, pp. 347–373, 2014, ISSN: 1947-5454. DOI: 10.1146/annurev-conmatphys-031113-133905.
- [18] G. C. Gardner, S. Fallahi, J. D. Watson, and M. J. Manfra, “Modified MBE hardware and techniques and role of gallium purity for attainment of two dimensional electron gas mobility $> 35 \times 10^6 \text{cm}^2/\text{Vs}$ in AlGaAs/GaAs quantum wells grown by MBE,” *Journal of Crystal Growth*, vol. 441, pp. 71–77, 2016, ISSN: 0022-0248. DOI: 10.1016/j.jcrysgro.2016.02.010. eprint: 1601.05401.
- [19] S. Liang, J. Nakamura, G. C. Gardner, and M. J. Manfra, “Reduction of charge noise in shallow GaAs/AlGaAs heterostructures with insulated gates,” *Applied Physics Letters*, vol. 117, no. 13, p. 133504, 2020, ISSN: 0003-6951. DOI: 10.1063/5.0026259.
- [20] J. S. Blakemore, “Semiconducting and other major properties of gallium arsenide,” *Journal of Applied Physics*, vol. 53, no. 10, R123–R181, 1982, ISSN: 0021-8979. DOI: 10.1063/1.331665.
- [21] S. Adachi, *GaAs and Related Materials, Bulk Semiconducting and Superlattice Properties*. WORLD SCIENTIFIC, 1994, ISBN: 9789810219253. DOI: 10.1142/2508.
- [22] L. L. Chang, L. Esaki, W. E. Howard, and R. Ludeke, “The Growth of a GaAs–GaAlAs Superlattice,” *Journal of Vacuum Science and Technology*, vol. 10, no. 1, pp. 11–16, 1973, ISSN: 0022-5355. DOI: 10.1116/1.1317919.

BIBLIOGRAPHY

- [23] C. Buizert, F. H. L. Koppens, M. Pioro-Ladrière, H.-P. Tranitz, I. T. Vink, S. Tarucha, W. Wegscheider, and L. M. K. Vandersypen, “InSitu Reduction of Charge Noise in GaAs/Al_xGa_{1-x}As Schottky-Gated Devices,” *Physical Review Letters*, vol. 101, no. 22, p. 226 603, 2008, ISSN: 0031-9007. DOI: 10.1103/physrevlett.101.226603. eprint: 0808.0465.
- [24] J. Smith, C. Berven, M. Wybourne, and S. Goodnick, “Conductance instabilities in quantum point contacts,” *Surface Science*, vol. 361, pp. 656–659, 1996, ISSN: 0039-6028. DOI: 10.1016/0039-6028(96)00493-1.
- [25] E. Buks, M. Heiblum, Y. Levinson, and H. Shtrikman, “Scattering of a two-dimensional electron gas by a correlated system of ionized donors,” *Semiconductor Science and Technology*, vol. 9, no. 11, p. 2031, 1994, ISSN: 0268-1242. DOI: 10.1088/0268-1242/9/11/001.
- [26] V. Umansky and M. Heiblum, “Molecular Beam Epitaxy,” in *Molecular Beam Epitaxy*, [Henini], Ed., Oxford: Elsevier, 2013, pp. 121–137, ISBN: 9780123878397. DOI: 10.1016/b978-0-12-387839-7.00006-3.
- [27] H. Störmer, R. Dingle, A. Gossard, W. Wiegmann, and M. Sturge, “Two-dimensional electron gas at a semiconductor-semiconductor interface,” *Solid State Communications*, vol. 29, no. 10, pp. 705–709, 1979, ISSN: 0038-1098. DOI: 10.1016/0038-1098(79)91010-x.
- [28] T. Ando, A. B. Fowler, and F. Stern, “Electronic properties of two-dimensional systems,” *Reviews of Modern Physics*, vol. 54, no. 2, pp. 437–672, 1982, ISSN: 0034-6861. DOI: 10.1103/revmodphys.54.437.
- [29] C. Beenakker and H. v. Houten, “Quantum Transport in Semiconductor Nanostructures,” *Solid State Physics*, vol. 44, pp. 1–228, 1991, ISSN: 0081-1947. DOI: 10.1016/s0081-1947(08)60091-0. eprint: cond-mat/0412664.

BIBLIOGRAPHY

- [30] C. Bureau-Oxton, J. C. Lemyre, and M. Pioro-Ladrière, “Nanofabrication of Gate-defined GaAs/AlGaAs Lateral Quantum Dots,” *Journal of Visualized Experiments*, no. 81, e50581, 2013. DOI: 10.3791/50581.
- [31] D. Waddington, A. M. Burke, S. Fricke, H. H. Tan, C. Jagadish, A. R. Hamilton, K. Trunov, D. Reuter, A. D. Wieck, and A. P. Micolich, “Can insulating the gates lead us to stable modulation-doped hole quantum devices?” *2010 Conference on Optoelectronic and Microelectronic Materials and Devices*, vol. 1, pp. 199–200, 2010. DOI: 10.1109/commad.2010.5699738.
- [32] A. M. Burke, D. E. J. Waddington, D. J. Carrad, R. W. Lyttleton, H. H. Tan, P. J. Reece, O. Klochan, A. R. Hamilton, A. Rai, D. Reuter, A. D. Wieck, and A. P. Micolich, “Origin of gate hysteresis in p-type Si-doped AlGaAs/GaAs heterostructures,” *Physical Review B*, vol. 86, no. 16, p. 165 309, 2012, ISSN: 1098-0121. DOI: 10.1103/physrevb.86.165309. eprint: 1207.2851.
- [33] B. J. v. Wees, H. v. Houten, C. W. J. Beenakker, J. G. Williamson, L. P. Kouwenhoven, D. v. d. Marel, and C. T. Foxon, “Quantized conductance of point contacts in a two-dimensional electron gas,” *Physical Review Letters*, vol. 60, no. 9, pp. 848–850, 1988, ISSN: 0031-9007. DOI: 10.1103/physrevlett.60.848.
- [34] D. A. Wharam, T. J. Thornton, R. Newbury, M. Pepper, H. Ahmed, J. E. F. Frost, D. G. Hasko, D. C. Peacock, D. A. Ritchie, and G. A. C. Jones, “One-dimensional transport and the quantisation of the ballistic resistance,” *Journal of Physics C: Solid State Physics*, vol. 21, no. 8, p. L209, 1988, ISSN: 0022-3719. DOI: 10.1088/0022-3719/21/8/002.
- [35] K. F. Berggren, T. J. Thornton, D. J. Newson, and M. Pepper, “Magnetic Depopulation of 1D Subbands in a Narrow 2D Electron Gas in a GaAs:AlGaAs Heterojunction,” *Physical Review Letters*, vol. 57, no. 14, pp. 1769–1772, 1986, ISSN: 0031-9007. DOI: 10.1103/physrevlett.57.1769.

BIBLIOGRAPHY

- [36] K. F. Berggren and D. J. Newson, “Magnetic depopulation of electronic subbands in low-dimensional semiconductor systems and their influence on the electrical resistivity and Hall effect,” *Semiconductor Science and Technology*, vol. 1, no. 5, p. 327, 1986, ISSN: 0268-1242. DOI: 10.1088/0268-1242/1/5/008.
- [37] H. V. Houten, C. W. J. Beenakker, and A. A. M. Staring, “Single Charge Tunneling, Coulomb Blockade Phenomena In Nanostructures,” *NATO ASI Series*, pp. 167–216, 1992, ISSN: 0258-1221. DOI: 10.1007/978-1-4757-2166-9_5.
- [38] D. A. Wharam, M. Pepper, H. Ahmed, J. E. F. Frost, D. G. Hasko, D. C. Peacock, D. A. Ritchie, and G. A. C. Jones, “Addition of the one-dimensional quantised ballistic resistance,” *Journal of Physics C: Solid State Physics*, vol. 21, no. 24, p. L887, 1988, ISSN: 0022-3719. DOI: 10.1088/0022-3719/21/24/002.
- [39] C. W. J. Beenakker and H. v. Houten, “Magnetotransport and non-additivity of point-contact resistances in series,” *Physical Review B*, vol. 39, no. 14, pp. 10 445–10 448, 1989, ISSN: 1098-0121. DOI: 10.1103/physrevb.39.10445.
- [40] L. W. Molenkamp, H. v. Houten, C. W. J. Beenakker, R. Eppenga, and C. T. Foxon, “Quantum oscillations in the transverse voltage of a channel in the nonlinear transport regime,” *Physical Review Letters*, vol. 65, no. 8, pp. 1052–1055, 1990, ISSN: 0031-9007. DOI: 10.1103/physrevlett.65.1052.
- [41] L. P. Kouwenhoven, B. J. v. Wees, C. J. P. M. Harmans, J. G. Williamson, H. v. Houten, C. W. J. Beenakker, C. T. Foxon, and J. J. Harris, “Nonlinear conductance of quantum point contacts,” *Physical Review B*, vol. 39, no. 11, pp. 8040–8043, Apr. 1989, ISSN: 1098-0121. DOI: 10.1103/physrevb.39.8040.
- [42] B. J. v. Wees, L. P. Kouwenhoven, E. M. M. Willems, C. J. P. M. Harmans, J. E. Mooij, H. v. Houten, C. W. J. Beenakker, J. G. Williamson, and C. T. Foxon, “Quantum ballistic and adiabatic elec-

BIBLIOGRAPHY

- tron transport studied with quantum point contacts,” *Physical Review B*, vol. 43, no. 15, pp. 12 431–12 453, 1991, ISSN: 1098-0121. DOI: 10.1103/physrevb.43.12431.
- [43] L. P. Kouwenhoven, N. C. v. d. Vaart, A. T. Johnson, W. Kool, C. J. P. M. Harmans, J. G. Williamson, A. A. M. Staring, and C. T. Foxon, “Single electron charging effects in semiconductor quantum dots,” *Zeitschrift für Physik B Condensed Matter*, vol. 85, no. 3, pp. 367–373, 1991, ISSN: 0722-3277. DOI: 10.1007/bf01307632.
- [44] M. A. Eriksson, R. G. Beck, M. Topinka, J. A. Katine, R. M. Westervelt, K. L. Campman, and A. C. Gossard, “Cryogenic scanning probe characterization of semiconductor nanostructures,” *Applied Physics Letters*, vol. 69, no. 5, pp. 671–673, 1996, ISSN: 0003-6951. DOI: 10.1063/1.117801.
- [45] M. A. Topinka, B. J. LeRoy, S. E. J. Shaw, E. J. Heller, R. M. Westervelt, K. D. Maranowski, and A. C. Gossard, “Imaging Coherent Electron Flow from a Quantum Point Contact,” *Science*, vol. 289, no. 5488, pp. 2323–2326, 2000, ISSN: 0036-8075. DOI: 10.1126/science.289.5488.2323.
- [46] M. A. Topinka, B. J. LeRoy, R. M. Westervelt, S. E. J. Shaw, R. Fleischmann, E. J. Heller, K. D. Maranowski, and A. C. Gossard, “Coherent branched flow in a two-dimensional electron gas,” *Nature*, vol. 410, no. 6825, pp. 183–186, 2001, ISSN: 0028-0836. DOI: 10.1038/35065553. eprint: cond-mat/0010348.
- [47] M. Field, C. G. Smith, M. Pepper, D. A. Ritchie, J. E. F. Frost, G. A. C. Jones, and D. G. Hasko, “Measurements of Coulomb blockade with a noninvasive voltage probe,” *Physical Review Letters*, vol. 70, no. 9, pp. 1311–1314, 1993, ISSN: 0031-9007. DOI: 10.1103/physrevlett.70.1311.
- [48] D. Sprinzak, Y. Ji, M. Heiblum, D. Mahalu, and H. Shtrikman, “Charge Distribution in a Kondo-Correlated Quantum Dot,” *Physi-*

BIBLIOGRAPHY

- cal Review Letters*, vol. 88, no. 17, p. 176 805, 2002, ISSN: 0031-9007. DOI: 10.1103/physrevlett.88.176805. eprint: cond-mat/0109402.
- [49] R. M. Potok, J. A. Folk, C. M. Marcus, V. Umansky, M. Hanson, and A. C. Gossard, “Spin and Polarized Current from Coulomb Blockaded Quantum Dots,” *Phys. Rev. Lett.*, vol. 91, p. 016 802, 2003. DOI: 10.1103/physrevlett.91.016802. eprint: cond-mat/0303152.
- [50] L. P. Kouwenhoven, C. M. Marcus, P. L. McEuen, S. Tarucha, R. M. Westervelt, and N. S. Wingreen, “Quantum Dots,” in *Mesoscopic Electron Transport*, Dordrecht: Springer Netherlands, 1997, pp. 105–214, ISBN: 9789048149063. DOI: 10.1007/978-94-015-8839-3_4.
- [51] R. Hanson, L. P. Kouwenhoven, J. R. Petta, S. Tarucha, and L. M. K. Vandersypen, “Spins in few-electron quantum dots,” *Reviews of Modern Physics*, vol. 79, no. 4, pp. 1217–1265, 2007, ISSN: 0034-6861. DOI: 10.1103/revmodphys.79.1217. eprint: cond-mat/0610433.
- [52] D. Loss and D. P. DiVincenzo, “Quantum computation with quantum dots,” *Physical Review A*, vol. 57, no. 1, pp. 120–126, 1998, ISSN: 1050-2947. DOI: 10.1103/physreva.57.120. eprint: cond-mat/9701055.
- [53] J. R. Petta, A. C. Johnson, J. M. Taylor, E. A. Laird, A. Yacoby, M. D. Lukin, C. M. Marcus, M. P. Hanson, and A. C. Gossard, “Coherent Manipulation of Coupled Electron Spins in Semiconductor Quantum Dots,” *Science*, vol. 309, no. 5744, pp. 2180–2184, 2005, ISSN: 0036-8075. DOI: 10.1126/science.1116955.
- [54] J. M. Elzerman, R. Hanson, L. H. W. v. Beveren, B. Witkamp, L. M. K. Vandersypen, and L. P. Kouwenhoven, “Single-shot read-out of an individual electron spin in a quantum dot,” *Nature*, vol. 430, no. 6998, pp. 431–435, 2004, ISSN: 0028-0836. DOI: 10.1038/nature02693. eprint: cond-mat/0411232.
- [55] D. Kim, Z. Shi, C. B. Simmons, D. R. Ward, J. R. Prance, T. S. Koh, J. K. Gamble, D. E. Savage, M. G. Lagally, M. Friesen, S. N. Coppersmith, and M. A. Eriksson, “Quantum control and process tomography of a semiconductor quantum dot hybrid qubit,” *Nature*,

BIBLIOGRAPHY

- vol. 511, no. 7507, pp. 70–74, 2014, ISSN: 0028-0836. DOI: 10.1038/nature13407. eprint: 1401.4416.
- [56] F. H. L. Koppens, C. Buizert, K. J. Tielrooij, I. T. Vink, K. C. Nowack, T. Meunier, L. P. Kouwenhoven, and L. M. K. Vandersypen, “Driven coherent oscillations of a single electron spin in a quantum dot,” *Nature*, vol. 442, no. 7104, pp. 766–771, 2006, ISSN: 0028-0836. DOI: 10.1038/nature05065. eprint: cond-mat/0608459.
- [57] L. P. Kouwenhoven, J. M. Elzerman, R. Hanson, L. H. W. v. Beveren, and L. M. K. Vandersypen, “Control and measurement of electron spins in semiconductor quantum dots,” *physica status solidi (b)*, vol. 243, no. 14, pp. 3682–3691, 2006, ISSN: 0370-1972. DOI: 10.1002/pssb.200642228.
- [58] D. Maradan, L. Casparis, T.-M. Liu, D. E. F. Biesinger, C. P. Scheller, D. M. Zumbühl, J. D. Zimmerman, and A. C. Gossard, “GaAs Quantum Dot Thermometry Using Direct Transport and Charge Sensing,” *Journal of Low Temperature Physics*, vol. 175, no. 5-6, pp. 784–798, 2014, ISSN: 0022-2291. DOI: 10.1007/s10909-014-1169-6. eprint: 1401.2330.
- [59] T. Fujisawa, D. G. Austing, Y. Tokura, Y. Hirayama, and S. Tarucha, “Allowed and forbidden transitions in artificial hydrogen and helium atoms,” *Nature*, vol. 419, no. 6904, pp. 278–281, 2002, ISSN: 0028-0836. DOI: 10.1038/nature00976.
- [60] G. Viola, S. Das, E. Grosfeld, and A. Stern, “Thermoelectric Probe for Neutral Edge Modes in the Fractional Quantum Hall Regime,” *Physical Review Letters*, vol. 109, no. 14, p. 146 801, 2012, ISSN: 0031-9007. DOI: 10.1103/physrevlett.109.146801. eprint: 1203.3813.
- [61] G. Li, E. J. König, and J. I. Väyrynen, “Topological symplectic Kondo effect,” *Phys. Rev. B*, vol. 107, p. L201401, 2023. DOI: 10.1103/physrevb.107.1201401. eprint: 2210.16614.

BIBLIOGRAPHY

- [62] E. J. König and A. M. Tsvelik, “Exact solution of the topological symplectic Kondo problem,” *Annals of Physics*, p. 169 231, 2023, ISSN: 0003-4916. DOI: 10.1016/j.aop.2023.169231.
- [63] S. D. Sarma, M. Freedman, and C. Nayak, “Majorana zero modes and topological quantum computation,” *npj Quantum Information*, vol. 1, no. 1, p. 15 001, 2015. DOI: 10.1038/npjqi.2015.1. eprint: 1501.02813.
- [64] N. Baldelli, U. Bhattacharya, D. González-Cuadra, M. Lewenstein, and T. Graß, “Detecting Majorana Zero Modes via Strong Field Dynamics,” *ACS Omega*, vol. 7, no. 50, pp. 47 424–47 430, 2022, ISSN: 2470-1343. DOI: 10.1021/acsomega.2c07169. eprint: 2202.03547.
- [65] P. Yu, J. Chen, M. Gomanko, G. Badawy, E. P. A. M. Bakkers, K. Zuo, V. Mourik, and S. M. Frolov, “Non-Majorana states yield nearly quantized conductance in proximatized nanowires,” *Nature Physics*, vol. 17, no. 4, pp. 482–488, 2021, ISSN: 1745-2473. DOI: 10.1038/s41567-020-01107-w. eprint: 2004.08583.
- [66] S. M. Frolov, M. J. Manfra, and J. D. Sau, “Topological superconductivity in hybrid devices,” *Nature Physics*, vol. 16, no. 7, pp. 718–724, 2020, ISSN: 1745-2473. DOI: 10.1038/s41567-020-0925-6.
- [67] V. Bayot, E. Grivei, S. Melinte, M. B. Santos, and M. Shayegan, “Giant Low Temperature Heat Capacity of GaAs Quantum Wells near Landau Level Filling $\nu=1$,” *Physical Review Letters*, vol. 76, no. 24, pp. 4584–4587, 1996, ISSN: 0031-9007. DOI: 10.1103/physrevlett.76.4584. eprint: cond-mat/9603024.
- [68] E. Gornik, R. Lassnig, G. Strasser, H. L. Störmer, A. C. Gossard, and W. Wiegmann, “Specific Heat of Two-Dimensional Electrons in GaAs-GaAlAs Multilayers,” *Physical Review Letters*, vol. 54, no. 16, pp. 1820–1823, 1985, ISSN: 0031-9007. DOI: 10.1103/physrevlett.54.1820.

BIBLIOGRAPHY

- [69] J. K. Wang, J. H. Campbell, D. C. Tsui, and A. Y. Cho, “Heat capacity of the two-dimensional electron gas in GaAs/Al_xGa_{1-x}As multiple-quantum-well structures,” *Physical Review B*, vol. 38, no. 9, pp. 6174–6184, 1988, ISSN: 1098-0121. DOI: 10.1103/physrevb.38.6174.
- [70] F. Schulze-Wischeler, U. Zeitler, C. v. Zobeltitz, F. Hohls, D. Reuter, A. D. Wieck, H. Frahm, and R. J. Haug, “Measurement of the specific heat of a fractional quantum Hall system,” *Physical Review B*, vol. 76, no. 15, p. 153 311, 2007, ISSN: 1098-0121. DOI: 10.1103/physrevb.76.153311. eprint: cond-mat/0607167.
- [71] B. A. Schmidt, K. Bennaceur, S. Gaucher, G. Gervais, L. N. Pfeiffer, and K. W. West, “Specific heat and entropy of fractional quantum Hall states in the second Landau level,” *Physical Review B*, vol. 95, no. 20, p. 201 306, 2017, ISSN: 2469-9950. DOI: 10.1103/physrevb.95.201306. eprint: 1605.02344.
- [72] U. Zeitler, A. M. Devitt, J. E. Digby, C. J. Mellor, A. J. Kent, K. A. Benedict, and T. Cheng, “Ballistic Heating of a Two-Dimensional Electron System by Phonon Excitation of the Magnetoroton Minimum at $\nu=1/3$,” *Physical Review Letters*, vol. 82, no. 26, pp. 5333–5336, 1998, ISSN: 0031-9007. DOI: 10.1103/physrevlett.82.5333.
- [73] A. J. Kent, R. E. Strickland, K. R. Strickland, and M. Henini, “Phonoconductivity measurement of the phonon absorption by a two-dimensional hole gas in a GaAs heterojunction,” *Physical Review B*, vol. 54, no. 3, pp. 2019–2027, 1996, ISSN: 1098-0121. DOI: 10.1103/physrevb.54.2019.
- [74] F. Schulze-Wischeler, F. Hohls, U. Zeitler, D. Reuter, A. D. Wieck, and R. J. Haug, “Phonon Excitations of Composite-Fermion Landau Levels,” *Physical Review Letters*, vol. 93, no. 2, p. 026 801, 2004, ISSN: 0031-9007. DOI: 10.1103/physrevlett.93.026801.
- [75] S. Gustavsson, R. Leturcq, M. Studer, I. Shorubalko, T. Ihn, K. Ensslin, D. Driscoll, and A. Gossard, “Electron counting in quantum

BIBLIOGRAPHY

- dots,” *Surface Science Reports*, vol. 64, no. 6, pp. 191–232, 2009, ISSN: 0167-5729. DOI: 10.1016/j.surfrep.2009.02.001. eprint: 0905.4675.
- [76] K. MacLean, S. Amasha, I. P. Radu, D. M. Zumbühl, M. A. Kastner, M. P. Hanson, and A. C. Gossard, “Energy-Dependent Tunneling in a Quantum Dot,” *Physical Review Letters*, vol. 98, no. 3, p. 036 802, 2006, ISSN: 0031-9007. DOI: 10.1103/physrevlett.98.036802. eprint: cond-mat/0610679.
- [77] A. Hofmann, V. F. Maisi, C. Gold, T. Krähenmann, C. Rössler, J. Basset, P. Märki, C. Reichl, W. Wegscheider, K. Ensslin, and T. Ihn, “Measuring the degeneracy of discrete energy levels using a GaAs/AlGaAs quantum dot,” *Physical Review Letters*, 2016. DOI: 10.1103/physrevlett.117.206803. eprint: 1610.00928.
- [78] G. N. Lewis, “A New Principle of Equilibrium,” *Proceedings of the National Academy of Sciences*, vol. 11, no. 3, pp. 179–183, 1925, ISSN: 0027-8424. DOI: 10.1073/pnas.11.3.179.
- [79] D. T. Haar, “Foundations of Statistical Mechanics,” *Reviews of Modern Physics*, vol. 27, no. 3, pp. 289–338, 1955, ISSN: 0034-6861. DOI: 10.1103/revmodphys.27.289.
- [80] T. Choi, T. Ihn, S. Schön, and K. Ensslin, “Counting statistics in an InAs nanowire quantum dot with a vertically coupled charge detector,” *Applied Physics Letters*, vol. 100, no. 7, p. 072 110, 2012, ISSN: 0003-6951. DOI: 10.1063/1.3687198. eprint: 1202.4273.
- [81] R. Garreis, J. D. Gerber, V. Stará, C. Tong, C. Gold, M. Rösli, K. Watanabe, T. Taniguchi, K. Ensslin, T. Ihn, and A. Kurzmann, “Counting statistics of single electron transport in bilayer graphene quantum dots,” *Physical Review Research*, vol. 5, no. 1, p. 013 042, 2023. DOI: 10.1103/physrevresearch.5.013042. eprint: 2210.07759.

BIBLIOGRAPHY

- [82] R. Schleser, E. Ruh, T. Ihn, K. Ensslin, D. C. Driscoll, and A. C. Gossard, “Time-resolved detection of individual electrons in a quantum dot,” *Applied Physics Letters*, vol. 85, no. 11, pp. 2005–2007, 2004, ISSN: 0003-6951. DOI: 10.1063/1.1784875. eprint: cond-mat/0406568.
- [83] E. Pyurbeeva and J. A. Mol, “A Thermodynamic Approach to Measuring Entropy in a Few-Electron Nanodevice,” *Entropy*, vol. 23, no. 6, p. 640, 2021. DOI: 10.3390/e23060640. eprint: 2008.05747.
- [84] A. Rozen, J. M. Park, U. Zondiner, Y. Cao, D. Rodan-Legrain, T. Taniguchi, K. Watanabe, Y. Oreg, A. Stern, E. Berg, P. Jarillo-Herrero, and S. Ilani, “Entropic evidence for a Pomeranchuk effect in magic-angle graphene,” *Nature*, vol. 592, no. 7853, pp. 214–219, 2021, ISSN: 0028-0836. DOI: 10.1038/s41586-021-03319-3. eprint: 2009.01836.
- [85] I. Pomeranchuk, “On the theory of Liquid He₃,” *Zhur. Eksptl'. i Teoret. Fiz.*, vol. 20, 1950.
- [86] Y. Saito, F. Yang, J. Ge, X. Liu, T. Taniguchi, K. Watanabe, J. I. A. Li, E. Berg, and A. F. Young, “Isospin Pomeranchuk effect in twisted bilayer graphene,” *Nature*, vol. 592, no. 7853, pp. 220–224, 2021, ISSN: 0028-0836. DOI: 10.1038/s41586-021-03409-2.
- [87] F. Yang, A. A. Zibrov, R. Bai, T. Taniguchi, K. Watanabe, M. P. Zaletel, and A. F. Young, “Experimental Determination of the Energy per Particle in Partially Filled Landau Levels,” *Physical Review Letters*, vol. 126, no. 15, p. 156802, 2021, ISSN: 0031-9007. DOI: 10.1103/physrevlett.126.156802. eprint: 2008.05466.
- [88] V. Zlatić, R. Monnier, J. K. Freericks, and K. W. Becker, “Relationship between the thermopower and entropy of strongly correlated electron systems,” *Physical Review B*, vol. 76, no. 8, p. 085122, 2007, ISSN: 1098-0121. DOI: 10.1103/physrevb.76.085122.

BIBLIOGRAPHY

- [89] J. Mravlje and A. Georges, “Thermopower and Entropy: Lessons from Sr₂RuO₄,” *Physical Review Letters*, vol. 117, no. 3, p. 036 401, 2016, ISSN: 0031-9007. DOI: 10.1103/physrevlett.117.036401. eprint: 1504.03860.
- [90] Y. Kleeorin, H. Thierschmann, H. Buhmann, A. Georges, L. W. Molenkamp, and Y. Meir, “How to measure the entropy of a mesoscopic system via thermoelectric transport,” *Nature Communications*, vol. 10, no. 1, p. 5801, 2019. DOI: 10.1038/s41467-019-13630-3. eprint: 1904.08948.
- [91] A. Harzheim, J. K. Sowa, J. L. Swett, G. A. D. Briggs, J. A. Mol, and P. Gehring, “Role of metallic leads and electronic degeneracies in thermoelectric power generation in quantum dots,” *Physical Review Research*, vol. 2, no. 1, p. 013 140, 2020. DOI: 10.1103/physrevresearch.2.013140. eprint: 1906.05401.
- [92] P. Gehring, J. K. Sowa, C. Hsu, J. d. Bruijkere, M. v. d. Star, J. J. L. Roy, L. Bogani, E. M. Gauger, and H. S. J. v. d. Zant, “Complete mapping of the thermoelectric properties of a single molecule,” *Nature Nanotechnology*, vol. 16, no. 4, pp. 426–430, 2021, ISSN: 1748-3387. DOI: 10.1038/s41565-021-00859-7.
- [93] E. Pyurbeeva, C. Hsu, D. Vogel, C. Wegeberg, M. Mayor, H. v. d. Zant, J. A. Mol, and P. Gehring, “Controlling the Entropy of a Single-Molecule Junction,” *Nano Letters*, vol. 21, no. 22, pp. 9715–9719, 2021, ISSN: 1530-6984. DOI: 10.1021/acs.nanolett.1c03591. eprint: 2109.06741.
- [94] M. Lavagna and C. Pépin, “The Kondo Lattice Model,” *Acta Physica Polonica B*, 1998.
- [95] W. d. Haas, J. d. Boer, and G. v. d. Berg, “The electrical resistance of gold, copper and lead at low temperatures,” *Physica*, vol. 1, no. 7-12, pp. 1115–1124, 1934, ISSN: 0031-8914. DOI: 10.1016/s0031-8914(34)80310-2.

BIBLIOGRAPHY

- [96] A. Gerritsen and J. Linde, “The electrical resistance of silver-manganese alloys at low temperatures Part I. The resistance from 273°K to 1°K,” *Physica*, vol. 17, no. 6, pp. 573–583, 1951, ISSN: 0031-8914. DOI: 10.1016/0031-8914(51)90113-9.
- [97] A. N. Gerritsen and J. Linde, “The electrical resistance of silver-manganese alloys at low temperatures Part 2. The resistance in a magnetic field,” *Physica*, vol. 17, no. 6, pp. 584–595, 1951, ISSN: 0031-8914. DOI: 10.1016/0031-8914(51)90114-0.
- [98] A. Gerritsen and J. Linde, “The electrical resistances of alloys of a noble metal and a transition metal,” *Physica*, vol. 18, no. 11, pp. 877–890, 1952, ISSN: 0031-8914. DOI: 10.1016/s0031-8914(52)80222-8.
- [99] K. S. Kim and M. B. Maple, “Kondo Effect in La_{1-x}Ce_x Alloys under Pressure,” *Physical Review B*, vol. 2, no. 11, pp. 4696–4699, 1970, ISSN: 1098-0121. DOI: 10.1103/physrevb.2.4696.
- [100] T. Aoi and Y. Masuda, “Magnetic Impurity Effects in Kondo Superconductor, La₃Al(Ce),” *Journal of the Physical Society of Japan*, vol. 37, no. 3, pp. 673–680, 1974, ISSN: 0031-9015. DOI: 10.1143/jpsj.37.673.
- [101] S. Katano and N. Mōri, “Pressure Effect on the Resistance Minimum in Antiferromagnetic Cr–Fe and Cr–Co Alloys,” *Journal of the Physical Society of Japan*, vol. 49, no. 5, pp. 1812–1819, 1980, ISSN: 0031-9015. DOI: 10.1143/jpsj.49.1812.
- [102] J. Korryng and A. Gerritsen, “The cooperative electron phenomenon in dilute alloys,” *Physica*, vol. 19, no. 1-12, pp. 457–507, 1953, ISSN: 0031-8914. DOI: 10.1016/s0031-8914(53)80053-4.
- [103] R. W. Schmitt, “Possible Approach to the Low-Temperature Resistance Maximum in Dilute Alloys of Transition Metals in Noble Metals,” *Physical Review*, vol. 103, no. 1, pp. 83–87, 1956, ISSN: 0031-899X. DOI: 10.1103/physrev.103.83.

BIBLIOGRAPHY

- [104] A. Brailsford and A. Overhauser, “Theory of the resistance minimum in dilute paramagnetic alloys,” *Journal of Physics and Chemistry of Solids*, vol. 15, no. 1-2, pp. 140–145, 1960, ISSN: 0022-3697. DOI: 10.1016/0022-3697(60)90111-6.
- [105] J. Kondo, “Resistance Minimum in Dilute Magnetic Alloys,” *Progress of Theoretical Physics*, vol. 32, no. 1, pp. 37–49, 1964, ISSN: 0033-068X. DOI: 10.1143/ptp.32.37.
- [106] G. V. D. Berg, “Chapter IV Anomalies in Dilute Metallic Solutions of Transition Elements,” in *Progress in Low Temperature Physics*, ser. Progress in Low Temperature Physics, [Gorter”], Ed., vol. 4, Elsevier, 1964, pp. 194–264, ISBN: 9780444533104. DOI: 10.1016/s0079-6417(08)60152-3.
- [107] S. D. Franceschi and W. G. v. d. Wiel, “Kondo Effect in Quantum Dots,” in *Handbook of Nanophysics, Nanoparticles and Quantum Dots*, K. D. Sattler, Ed., CRC Press, Sep. 2019, pp. 627–645. DOI: 10.1201/9781420075458.
- [108] A. Hewson and J. Kondo, “Kondo effect,” *Scholarpedia*, vol. 4, no. 3, p. 7529, 2009. DOI: 10.4249/scholarpedia.7529.
- [109] M. Pustilnik and L. Glazman, “Kondo effect in quantum dots,” *Journal of Physics: Condensed Matter*, vol. 16, no. 16, R513, 2004, ISSN: 0953-8984. DOI: 10.1088/0953-8984/16/16/r01. eprint: cond-mat/0401517.
- [110] H. Thierschmann, “Heat Conversion in Quantum Dot Systems,” Ph.D. dissertation, Julius-Maximilians-Universität Würzburg, 2014.
- [111] W. G. v. d. Wiel, S. D. Franceschi, T. Fujisawa, J. M. Elzerman, S. Tarucha, and L. P. Kouwenhoven, “The Kondo Effect in the Unitary Limit,” *Science*, vol. 289, no. 5487, pp. 2105–2108, 2000, ISSN: 0036-8075. DOI: 10.1126/science.289.5487.2105. eprint: cond-mat/0009405.

BIBLIOGRAPHY

- [112] D. Goldhaber-Gordon, H. Shtrikman, D. Mahalu, D. Abusch-Magder, U. Meirav, and M. A. Kastner, “Kondo effect in a single-electron transistor,” *Nature*, vol. 391, no. 6663, pp. 156–159, 1998, ISSN: 0028-0836. DOI: 10.1038/34373.
- [113] D. Goldhaber-Gordon, J. Göres, M. A. Kastner, H. Shtrikman, D. Mahalu, and U. Meirav, “From the Kondo Regime to the Mixed-Valence Regime in a Single-Electron Transistor,” *Physical Review Letters*, vol. 81, no. 23, pp. 5225–5228, 1998, ISSN: 0031-9007. DOI: 10.1103/physrevlett.81.5225.
- [114] S. M. Cronenwett, T. H. Oosterkamp, and L. P. Kouwenhoven, “A Tunable Kondo Effect in Quantum Dots,” *Science*, vol. 281, no. 5376, pp. 540–544, 1998, ISSN: 0036-8075. DOI: 10.1126/science.281.5376.540. eprint: cond-mat/9804211.
- [115] J. Schmid, J. Weis, K. Eberl, and K. v. Klitzing, “A quantum dot in the limit of strong coupling to reservoirs,” *Physica B: Condensed Matter*, vol. 256, pp. 182–185, 1998, ISSN: 0921-4526. DOI: 10.1016/S0921-4526(98)00533-x.
- [116] S. Sasaki, S. D. Franceschi, J. M. Elzerman, W. G. v. d. Wiel, M. Eto, S. Tarucha, and L. P. Kouwenhoven, “Kondo effect in an integer-spin quantum dot,” *Nature*, vol. 405, no. 6788, pp. 764–767, 2000, ISSN: 0028-0836. DOI: 10.1038/35015509. eprint: cond-mat/0004414.
- [117] P. Jarillo-Herrero, J. Kong, H. S. v. d. Zant, C. Dekker, L. P. Kouwenhoven, and S. D. Franceschi, “Orbital Kondo effect in carbon nanotubes,” *Nature*, vol. 434, no. 7032, pp. 484–488, 2005, ISSN: 0028-0836. DOI: 10.1038/nature03422. eprint: cond-mat/0504059.
- [118] A. W. Rushforth, C. G. Smith, I. Farrer, D. A. Ritchie, G. A. C. Jones, D. Anderson, and M. Pepper, “Fano effect and Kondo effect in quantum dots formed in strongly coupled quantum wells,” *Phys. Rev. B*, vol. 73, p. 081305, 2006. DOI: 10.1103/physrevb.73.081305. eprint: cond-mat/0602242.

BIBLIOGRAPHY

- [119] A. V. Kretinin, H. Shtrikman, D. Goldhaber-Gordon, M. Hanl, A. Weichselbaum, J. v. Delft, T. Costi, and D. Mahalu, “Spin-12 Kondo effect in an InAs nanowire quantum dot: Unitary limit, conductance scaling, and Zeeman splitting,” *Physical Review B*, vol. 84, no. 24, p. 245316, 2011, ISSN: 1098-0121. DOI: 10.1103/physrevb.84.245316. eprint: 1108.1773.
- [120] B. Dutta, D. Majidi, A. G. Corral, P. A. Erdman, S. Florens, T. A. Costi, H. Courtois, and C. B. Winkelmann, “Direct Probe of the Seebeck Coefficient in a Kondo-Correlated Single-Quantum-Dot Transistor,” *Nano Letters*, vol. 19, no. 1, pp. 506–511, 2019, ISSN: 1530-6984. DOI: 10.1021/acs.nanolett.8b04398. eprint: 1811.04219.
- [121] A. Kurzmann, Y. Kleeorin, C. Tong, R. Garreis, A. Knothe, M. Eich, C. Mittag, C. Gold, F. K. d. Vries, K. Watanabe, T. Taniguchi, V. Fal’ko, Y. Meir, T. Ihn, and K. Ensslin, “Kondo effect and spin-orbit coupling in graphene quantum dots,” *Nature Communications*, vol. 12, no. 1, p. 6004, 2021. DOI: 10.1038/s41467-021-26149-3. eprint: 2103.04864.
- [122] L. I. Glazman and M. É. Raïkh, “Resonant Kondo transparency of a barrier with quasilocal impurity states,” *Journal of Experimental and Theoretical Physics Letters*, vol. 47, p. 452, Apr. 1988.
- [123] Y. Meir, N. S. Wingreen, and P. A. Lee, “Low-temperature transport through a quantum dot: The Anderson model out of equilibrium,” *Physical Review Letters*, vol. 70, no. 17, pp. 2601–2604, Apr. 1993, ISSN: 0031-9007. DOI: 10.1103/physrevlett.70.2601. eprint: cond-mat/9212007.
- [124] N. S. Wingreen and Y. Meir, “Anderson model out of equilibrium: Noncrossing-approximation approach to transport through a quantum dot,” *Physical Review B*, vol. 49, no. 16, pp. 11040–11052, 1994, ISSN: 1098-0121. DOI: 10.1103/physrevb.49.11040. eprint: cond-mat/9309043.

BIBLIOGRAPHY

- [125] A.-P. Jauho, N. S. Wingreen, and Y. Meir, “Time-dependent transport in interacting and noninteracting resonant-tunneling systems,” *Physical Review B*, vol. 50, no. 8, pp. 5528–5544, 1994, ISSN: 1098-0121. DOI: 10.1103/physrevb.50.5528. eprint: cond-mat/9404027.
- [126] A. Kaminski, Y. V. Nazarov, and L. I. Glazman, “Suppression of the Kondo Effect in a Quantum Dot by External Irradiation,” *Phys. Rev. Lett.*, vol. 83, pp. 384–387, 1999. DOI: 10.1103/physrevlett.83.384. eprint: cond-mat/9903436.
- [127] R. Leturcq, L. Schmid, K. Ensslin, Y. Meir, D. C. Driscoll, and A. C. Gossard, “Probing the Kondo Density of States in a Three-Terminal Quantum Ring,” *Physical Review Letters*, vol. 95, no. 12, p. 126 603, 2005, ISSN: 0031-9007. DOI: 10.1103/physrevlett.95.126603. eprint: cond-mat/0505111.
- [128] S. Hershfield, J. H. Davies, and J. W. Wilkins, “Probing the Kondo resonance by resonant tunneling through an Anderson impurity,” *Physical Review Letters*, vol. 67, no. 26, pp. 3720–3723, 1991, ISSN: 0031-9007. DOI: 10.1103/physrevlett.67.3720.
- [129] J. König, H. Schoeller, and G. Schön, “Zero-Bias Anomalies and Boson-Assisted Tunneling Through Quantum Dots,” *Physical Review Letters*, vol. 76, no. 10, pp. 1715–1718, 1996, ISSN: 0031-9007. DOI: 10.1103/physrevlett.76.1715. eprint: cond-mat/9506081.
- [130] S. D. Franceschi, R. Hanson, W. G. v. d. Wiel, J. M. Elzerman, J. J. Wijkema, T. Fujisawa, S. Tarucha, and L. P. Kouwenhoven, “Out-of-Equilibrium Kondo Effect in a Mesoscopic Device,” *Physical Review Letters*, vol. 89, no. 15, p. 156 801, 2002, ISSN: 0031-9007. DOI: 10.1103/physrevlett.89.156801.
- [131] S. Csonka, L. Hofstetter, F. Freitag, S. Oberholzer, C. Schönenberger, T. S. Jespersen, M. Aagesen, and J. Nygård, “Giant Fluctuations and Gate Control of the g-Factor in InAs Nanowire Quantum Dots,” *Nano Letters*, vol. 8, no. 11, pp. 3932–3935, 2008, ISSN: 1530-6984. DOI: 10.1021/nl802418w. eprint: 0808.1492.

BIBLIOGRAPHY

- [132] A. Kogan, S. Amasha, D. Goldhaber-Gordon, G. Granger, M. A. Kastner, and H. Shtrikman, “Measurements of Kondo and Spin Splitting in Single-Electron Transistors,” *Physical Review Letters*, vol. 93, no. 16, p. 166 602, 2004, ISSN: 0031-9007. DOI: 10.1103/physrevlett.93.166602. eprint: cond-mat/0312186.
- [133] M. Avinun-Kalish, M. Heiblum, A. Silva, D. Mahalu, and V. Umansky, “Controlled Dephasing of a Quantum Dot in the Kondo Regime,” *Physical Review Letters*, vol. 92, no. 15, p. 156 801, Apr. 2004, ISSN: 0031-9007. DOI: 10.1103/physrevlett.92.156801. eprint: cond-mat/0309230.
- [134] R. Scheibner, H. Buhmann, D. Reuter, M. N. Kiselev, and L. W. Molenkamp, “Thermopower of a Kondo Spin-Correlated Quantum Dot,” *Physical Review Letters*, vol. 95, no. 17, p. 176 602, 2005, ISSN: 0031-9007. DOI: 10.1103/physrevlett.95.176602. eprint: cond-mat/0410671.
- [135] M. R. Delbecq, V. Schmitt, F. D. Parmentier, N. Roch, J. J. Viennot, G. Fève, B. Huard, C. Mora, A. Cottet, and T. Kontos, “Coupling a Quantum Dot, Fermionic Leads, and a Microwave Cavity on a Chip,” *Physical Review Letters*, vol. 107, no. 25, p. 256 804, 2011, ISSN: 0031-9007. DOI: 10.1103/physrevlett.107.256804. eprint: 1108.4371.
- [136] S. J. Chorley, M. R. Galpin, F. W. Jayatilaka, C. G. Smith, D. E. Logan, and M. R. Buitelaar, “Tunable Kondo Physics in a Carbon Nanotube Double Quantum Dot,” *Physical Review Letters*, vol. 109, no. 15, p. 156 804, 2012, ISSN: 0031-9007. DOI: 10.1103/physrevlett.109.156804. eprint: 1209.3735.
- [137] M. Niklas, S. Smirnov, D. Mantelli, M. Margańska, N.-V. Nguyen, W. Wernsdorfer, J.-P. Cleuziou, and M. Grifoni, “Blocking transport resonances via Kondo many-body entanglement in quantum dots,” *Nature Communications*, vol. 7, no. 1, p. 12 442, 2016. DOI: 10.1038/ncomms12442. eprint: 1603.00380.

BIBLIOGRAPHY

- [138] A. Svilans, M. Josefsson, A. M. Burke, S. Fahlvik, C. Thelander, H. Linke, and M. Leijnse, “Thermoelectric characterization of the Kondo resonance in nanowire quantum dots,” *Physical Review Letters*, 2018. DOI: 10.1103/physrevlett.121.206801. eprint: 1807.07807.
- [139] I. V. Borzenets, J. Shim, J. C. H. Chen, A. Ludwig, A. D. Wieck, S. Tarucha, H.-S. Sim, and M. Yamamoto, “Observation of the Kondo screening cloud,” *Nature*, vol. 579, no. 7798, pp. 210–213, 2020, ISSN: 0028-0836. DOI: 10.1038/s41586-020-2058-6.
- [140] O. Legeza, C. P. Moca, A. I. Toth, I. Weymann, and G. Zarand, “Manual for the Flexible DM-NRG code,” *arXiv*, 2008. eprint: 0809.3143.
- [141] A. I. Tóth, C. P. Moca, Ö. Legeza, and G. Zaránd, “Density matrix numerical renormalization group for non-Abelian symmetries,” *Physical Review B*, vol. 78, no. 24, p. 245 109, 2008, ISSN: 1098-0121. DOI: 10.1103/physrevb.78.245109. eprint: 0802.4332.
- [142] P. W. Anderson, “Localized Magnetic States in Metals,” *Physical Review*, vol. 124, no. 1, pp. 41–53, 1961, ISSN: 0031-899X. DOI: 10.1103/physrev.124.41.
- [143] K. G. Wilson, “The renormalization group: Critical phenomena and the Kondo problem,” *Reviews of Modern Physics*, vol. 47, no. 4, pp. 773–840, 1975, ISSN: 0034-6861. DOI: 10.1103/revmodphys.47.773.
- [144] R. Bulla, T. A. Costi, and T. Pruschke, “Numerical renormalization group method for quantum impurity systems,” *Rev. Mod. Phys.*, vol. 80, no. 2, pp. 395–450, 2008, ISSN: 0034-6861. DOI: 10.1103/revmodphys.80.395. eprint: cond-mat/0701105.
- [145] M. Salmhofer, “Renormalization in condensed matter: Fermionic systems – from mathematics to materials,” *Nuclear Physics B*, vol. 941, pp. 868–899, 2019, ISSN: 0550-3213. DOI: 10.1016/j.nuclphysb.2018.07.004. eprint: 1807.01766.

BIBLIOGRAPHY

- [146] T. Child, O. Sheekey, S. Lüscher, S. Fallahi, G. C. Gardner, M. Manfra, and J. Folk, “A Robust Protocol for Entropy Measurement in Mesoscopic Circuits,” *Entropy*, vol. 24, no. 3, p. 417, 2022. DOI: 10.3390/e24030417. eprint: 2110.14172.
- [147] C. Barthel, M. Kjærgaard, J. Medford, M. Stopa, C. M. Marcus, M. P. Hanson, and A. C. Gossard, “Fast sensing of double-dot charge arrangement and spin state with a radio-frequency sensor quantum dot,” *Physical Review B*, vol. 81, no. 16, p. 161 308, 2010, ISSN: 1098-0121. DOI: 10.1103/physrevb.81.161308. eprint: 1001.3585.
- [148] J. M. Elzerman, R. Hanson, J. S. Greidanus, L. H. W. v. Beveren, S. D. Franceschi, L. M. K. Vandersypen, S. Tarucha, and L. P. Kouwenhoven, “Few-electron quantum dot circuit with integrated charge read out,” *Physical Review B*, vol. 67, no. 16, p. 161 308, 2003, ISSN: 1098-0121. DOI: 10.1103/physrevb.67.161308. eprint: cond-mat/0212489.
- [149] I. L. Aleiner, N. S. Wingreen, and Y. Meir, “Dephasing and the Orthogonality Catastrophe in Tunneling through a Quantum Dot: The “Which Path?” Interferometer,” *Physical Review Letters*, vol. 79, no. 19, pp. 3740–3743, 1997, ISSN: 0031-9007. DOI: 10.1103/physrevlett.79.3740. eprint: cond-mat/9702001.
- [150] A. Silva and S. Levit, “Peculiarities of the controlled dephasing of a quantum dot in the Kondo regime,” *Europhysics Letters*, vol. 62, no. 1, pp. 103–109, 2003, ISSN: 0295-5075. DOI: 10.1209/epl/i2003-00368-1.
- [151] K. Kang and G. L. Khym, “Entanglement, measurement, and conditional evolution of the Kondo singlet interacting with a mesoscopic detector,” *New Journal of Physics*, vol. 9, no. 5, p. 121, 2007, ISSN: 1367-2630. DOI: 10.1088/1367-2630/9/5/121. eprint: 0707.1171.
- [152] T. Child, O. Sheekey, S. Lüscher, S. Fallahi, G. C. Gardner, M. Manfra, A. Mitchell, E. Sela, Y. Kleorin, Y. Meir, and J. Folk, “Entropy Measurement of a Strongly Coupled Quantum Dot,” *Physical Re-*

BIBLIOGRAPHY

- view Letters*, vol. 129, no. 22, p. 227 702, 2022, ISSN: 0031-9007. DOI: 10.1103/physrevlett.129.227702. eprint: 2110.14158.
- [153] A. Mittal, R. Wheeler, M. Keller, D. Prober, and R. Sacks, “Electron-phonon scattering rates in GaAs/AlGaAs 2DEG samples below 0.5 K,” *Surface Science*, vol. 361, pp. 537–541, 1996, ISSN: 0039-6028. DOI: 10.1016/0039-6028(96)00464-5.
- [154] S. Sankar, E. Sela, and C. Han, “Measuring Topological Entanglement Entropy Using Maxwell Relations,” *Physical Review Letters*, vol. 131, no. 1, p. 016 601, 2023, ISSN: 0031-9007. DOI: 10.1103/physrevlett.131.016601. eprint: 2212.09856.
- [155] A. Hübner, J. Weis, and K. v. Klitzing, “Precise experimental characterization of a double quantum dot system with strong capacitive interdot coupling,” *Physica E: Low-dimensional Systems and Nanostructures*, vol. 40, no. 5, pp. 1573–1575, 2008, ISSN: 1386-9477. DOI: 10.1016/j.physe.2007.09.109.
- [156] A. Y. Kitaev, “Unpaired Majorana fermions in quantum wires,” *Physics-Uspekhi*, vol. 44, no. 10S, pp. 131–136, 2001, ISSN: 1063-7869. DOI: 10.1070/1063-7869/44/10s/s29. eprint: cond-mat/0010440.
- [157] Y. Oreg, G. Refael, and F. v. Oppen, “Helical Liquids and Majorana Bound States in Quantum Wires,” *Physical Review Letters*, vol. 105, no. 17, p. 177 002, 2010, ISSN: 0031-9007. DOI: 10.1103/physrevlett.105.177002. eprint: 1003.1145.
- [158] R. M. Lutchyn, J. D. Sau, and S. D. Sarma, “Majorana Fermions and a Topological Phase Transition in Semiconductor-Superconductor Heterostructures,” *Physical Review Letters*, vol. 105, no. 7, p. 077 001, 2010, ISSN: 0031-9007. DOI: 10.1103/physrevlett.105.077001. eprint: 1002.4033.
- [159] R. M. Lutchyn, E. P. A. M. Bakkers, L. P. Kouwenhoven, P. Krogstrup, C. M. Marcus, and Y. Oreg, “Majorana zero modes in superconductor–semiconductor heterostructures,” *Nature Reviews Materials*,

BIBLIOGRAPHY

- vol. 3, no. 5, pp. 52–68, 2018. DOI: 10.1038/s41578-018-0003-1. eprint: 1707.04899.
- [160] V. Mourik, K. Zuo, S. M. Frolov, S. R. Plissard, E. P. A. M. Bakkers, and L. P. Kouwenhoven, “Signatures of Majorana Fermions in Hybrid Superconductor-Semiconductor Nanowire Devices,” *Science*, vol. 336, no. 6084, pp. 1003–1007, 2012, ISSN: 0036-8075. DOI: 10.1126/science.1222360. eprint: 1204.2792.
- [161] A. Das, Y. Ronen, Y. Most, Y. Oreg, M. Heiblum, and H. Shtrikman, “Zero-bias peaks and splitting in an Al–InAs nanowire topological superconductor as a signature of Majorana fermions,” *Nature Physics*, vol. 8, no. 12, pp. 887–895, 2012, ISSN: 1745-2473. DOI: 10.1038/nphys2479. eprint: 1205.7073.
- [162] R. M. Potok, I. G. Rau, H. Shtrikman, Y. Oreg, and D. Goldhaber-Gordon, “Observation of the two-channel Kondo effect,” *Nature*, vol. 446, no. 7132, pp. 167–171, 2007, ISSN: 0028-0836. DOI: 10.1038/nature05556. eprint: cond-mat/0610721.
- [163] A. J. Keller, L. Peeters, C. P. Moca, I. Weymann, D. Mahalu, V. Umansky, G. Zaránd, and D. Goldhaber-Gordon, “Universal Fermi liquid crossover and quantum criticality in a mesoscopic system,” *Nature*, vol. 526, no. 7572, pp. 237–240, 2015, ISSN: 0028-0836. DOI: 10.1038/nature15261. eprint: 1504.07620.
- [164] J. P. Dehollain, U. Mukhopadhyay, V. P. Michal, Y. Wang, B. Wunsch, C. Reichl, W. Wegscheider, M. S. Rudner, E. Demler, and L. M. K. Vandersypen, “Nagaoka ferromagnetism observed in a quantum dot plaquette,” *Nature*, vol. 579, no. 7800, pp. 528–533, 2020, ISSN: 0028-0836. DOI: 10.1038/s41586-020-2051-0. eprint: 1904.05680.
- [165] A. Tsvelick and P. Wiegmann, “Exact results in the theory of magnetic alloys,” *Advances in Physics*, vol. 32, no. 4, pp. 453–713, 1983, ISSN: 0001-8732. DOI: 10.1080/00018738300101581.

BIBLIOGRAPHY

- [166] C. Mora, C. P. Moca, J. v. Delft, and G. Zaránd, “Fermi-liquid theory for the single-impurity Anderson model,” *Physical Review B*, vol. 92, no. 7, p. 075 120, 2015, ISSN: 1098-0121. DOI: 10.1103/physrevb.92.075120. eprint: 1409.3451.
- [167] M. J. D. Powell, “An efficient method for finding the minimum of a function of several variables without calculating derivatives,” *The Computer Journal*, vol. 7, no. 2, pp. 155–162, 1964, ISSN: 0010-4620. DOI: 10.1093/comjnl/7.2.155.
- [168] F. D. M. Haldane, “Scaling Theory of the Asymmetric Anderson Model,” *Physical Review Letters*, vol. 40, no. 6, pp. 416–419, 1978, ISSN: 0031-9007. DOI: 10.1103/physrevlett.40.416.
- [169] S. Kirchner, “Two-Channel Kondo Physics: From Engineered Structures to Quantum Materials Realizations,” *Advanced Quantum Technologies*, vol. 3, no. 5, p. 1 900 128, 2020, ISSN: 2511-9044. DOI: 10.1002/qute.201900128.
- [170] Z. Iftikhar, S. Jezouin, A. Anthore, U. Gennser, F. D. Parmentier, A. Cavanna, and F. Pierre, “Two-channel Kondo effect and renormalization flow with macroscopic quantum charge states,” *Nature*, vol. 526, no. 7572, pp. 233–236, 2015, ISSN: 0028-0836. DOI: 10.1038/nature15384. eprint: 1602.02056.
- [171] U. Mukhopadhyay, J. P. Dehollain, C. Reichl, W. Wegscheider, and L. M. K. Vandersypen, “A 2×2 quantum dot array with controllable inter-dot tunnel couplings,” *Applied Physics Letters*, vol. 112, no. 18, p. 183 505, 2018, ISSN: 0003-6951. DOI: 10.1063/1.5025928. eprint: 1802.05446.
- [172] B.-B. Chen, Y. D. Liao, Z. Chen, O. Vafek, J. Kang, W. Li, and Z. Y. Meng, “Realization of topological Mott insulator in a twisted bilayer graphene lattice model,” *Nature Communications*, vol. 12, no. 1, p. 5480, 2021. DOI: 10.1038/s41467-021-25438-1. eprint: 2011.07602.

- [173] G. Nicolí, P. Märki, B. A. Bräm, M. P. Rösli, S. Hennel, A. Hofmann, C. Reichl, W. Wegscheider, T. Ihn, and K. Ensslin, “Quantum dot thermometry at ultra-low temperature in a dilution refrigerator with a ^4He immersion cell,” *Review of Scientific Instruments*, vol. 90, no. 11, p. 113 901, Nov. 2019, ISSN: 0034-6748. DOI: 10.1063/1.5127830. eprint: https://pubs.aip.org/aip/rsi/article-pdf/doi/10.1063/1.5127830/15636798/113901_1_online.pdf.
- [174] Z. Iftikhar, A. Anthore, S. Jezouin, F. D. Parmentier, Y. Jin, A. Cavanna, A. Ouerghi, U. Gennser, and F. Pierre, “Primary thermometry triad at 6 mK in mesoscopic circuits,” *Nature Communications*, vol. 7, no. 1, p. 12 908, 2016. DOI: 10.1038/ncomms12908. eprint: 1610.03716.

Appendix A

NRG data and fitting

The following pages represent a python Jupyter notebook that demonstrates loading and working with the NRG calculation data provided by Yaakov Kleorin and Yigal Meir. For completeness, all functions necessary to run the notebook are included explicitly. In a normal use case, many of the functions defined in the notebook would be defined in separate files and only included where necessary. The notebook and data can be found at https://github.com/TimChild/thesis_nrg_appendix.

1 Introduction

This is intended to explain how the NRG data produced by Yaakov Kleeorin (and Yigal Meir) is used in fitting to experimental data

Note that many of the functions shown here are somewhat over-complicated for the minimal examples presented here, but I have included them in their entirety for completeness. The functions presented here are from a larger package of analysis functions that I developed over several years. It can be found at https://github.com/TimChild/dat_analysis.

2 Setting up Notebook

```
[2]: # Get all the external imports out of the way
# Python built ins
from dataclasses import dataclass
from functools import lru_cache
import datetime
import sys

# Third party imports
import matplotlib
import matplotlib.pyplot as plt
import matplotlib as mpl
import seaborn as sns
import numpy as np
import lmfit as lm
import scipy
import numpy as np
import scipy

print(f"python version: {sys.version}")
print(f"matplotlib version: {matplotlib.__version__}")
print(f"seaborn version: {sns.__version__}")
print(f"numpy version: {np.__version__}")
print(f"lmfit version: {lm.__version__}")
print(f"scipy version: {scipy.__version__}")
```

```
python version: 3.10.10 | packaged by Anaconda, Inc. | (main, Mar 21 2023,
18:39:17) [MSC v.1916 64 bit (AMD64)]
matplotlib version: 3.7.1
seaborn version: 0.12.2
numpy version: 1.24.2
lmfit version: 1.1.0
scipy version: 1.10.1
```

Appendix A. NRG data and fitting

```
[4]: %matplotlib inline
mpl.rcParams.update(
    {
        "figure.dpi": 110, # 27in 1440p = 110
    }
)
# FIG_SCALE -- Set to full width of page (~6in)
FS = 6

def decrease_fontsize(ax, decrease_fs):
    """
    Decrease the font sizes of various elements of a given ax by
    decrease_fs.

    Parameters:
    - ax: The axes for which font sizes should be decreased.
    - decrease_fs: The amount by which to decrease the font size.
    """
    # Decreasing font size for x and y tick labels
    current_xticks_fs = ax.xaxis.get_ticklabels()[0].get_fontsize()
    current_yticks_fs = ax.yaxis.get_ticklabels()[0].get_fontsize()
    ax.tick_params(axis="x", labelsz=current_xticks_fs - decrease_fs)
    ax.tick_params(axis="y", labelsz=current_yticks_fs - decrease_fs)

    # Decreasing font size for x and y axis labels
    ax.xaxis.label.set_fontsize(ax.xaxis.label.get_fontsize() -
    decrease_fs)
    ax.yaxis.label.set_fontsize(ax.yaxis.label.get_fontsize() -
    decrease_fs)

    # Decreasing font size for title
    ax.title.set_fontsize(ax.title.get_fontsize() - decrease_fs)

    # Decreasing font size of axes exponents
    ax.xaxis.get_offset_text().set_fontsize(
        ax.xaxis.get_offset_text().get_fontsize() - decrease_fs
    )
    ax.yaxis.get_offset_text().set_fontsize(
        ax.yaxis.get_offset_text().get_fontsize() - decrease_fs
    )

    # Decreasing font size for legend (if present)
    if ax.get_legend():
```

Appendix A. NRG data and fitting

```
for text in ax.get_legend().get_texts():
    text.set_fontsize(text.get_fontsize() - decrease_fs)
```

3 Loading NRG Calculation data

Now, we'll define a class for loading and holding NRG calculations.

```
[5]: @dataclass
class NRGData:
    ens: np.ndarray
    ts: np.ndarray
    conductance: np.ndarray
    dndt: np.ndarray
    entropy: np.ndarray
    occupation: np.ndarray
    int_dndt: np.ndarray
    gs: np.ndarray

    @classmethod
    @lru_cache
    def from_mat(cls):
        """Combines two new NRG datasets (the first has good thermally_
        broadened data, but isn't wide enough for
        gamma broadened data. The second is more gamma broadened data_
        only over a wider range but with the same density
        of points (i.e. a differently shaped array)

        This combines both and adds NaNs to the narrower data so that_
        they can still be treated as arrays.
        """

        def pad_to_shape(arr: np.ndarray, desired_x_shape: int):
            """Pads array with NaNs so that it has a given x dimension"""
            if arr.shape[-1] > desired_x_shape:
                raise RuntimeError(f"{arr.shape[-1]} > {desired_x_shape}")
            diff = desired_x_shape - arr.shape[-1]
            pads = [(0, 0)] * (arr.ndim - 1)
            pads.extend([(0, diff)]) # Pad all NaNs, at end of data
            return np.pad(arr, pad_width=pads, mode="constant",_
            constant_values=np.nan)

        NRG_DATAS = [
            "Mu_mat",
```

Appendix A. NRG data and fitting

```

        "Conductance_mat",
        "DNDT_mat",
        "Entropy_mat",
        "Occupation_mat",
        "intDNDT_mat",
    ]

    # Thermally broadened data (includes gamma broadened which isn't
    ←wide enough)
    path = "nrg_calculations/NRGresultsNew.mat"
    data = scipy.io.loadmat(path)
    rows_from_narrow = np.s_[
        0:10
    ] # 0 -> 9 are the thermal rows from first set of data
    dx_shape, dy_shape = data["Mu_mat"][:, rows_from_narrow].shape

    # Gamma broadened data (same as in above but much wider)
    path = "nrg_calculations/NRGresultsNewWide.mat"
    wide_data = scipy.io.loadmat(path)
    wx_shape, wy_shape = wide_data["Mu_mat"].shape

    common_x_shape = wx_shape # This has the larger shape

    new_data = {}
    for k in NRG_DATAS:
        if k in data and wide_data:
            d = data[k].T[rows_from_narrow]
            padded = pad_to_shape(d, common_x_shape)
            new_data[k] = np.concatenate([padded, wide_data[k].T],
    ←axis=0)
        else:
            # Just getting shape using an array I know will exist
            full_shape = (dy_shape + wy_shape, common_x_shape)
            new_data[k] = np.zeros(full_shape)
    new_data["Ts"] = np.array(
        [data["T"][0, 0] * dy_shape + [wide_data["T"][0, 0]] *
    ←wy_shape
    )
    new_data["Gammas"] = np.concatenate(
        [
            data.get("Gammas").flatten()[rows_from_narrow],
            wide_data.get("Gammas").flatten(),
        ]
    )

```

Appendix A. NRG data and fitting

```
return cls(  
    ens=new_data["Mu_mat"],  
    ts=new_data["Ts"],  
    conductance=new_data["Conductance_mat"],  
    dndt=new_data["DNDT_mat"],  
    entropy=new_data["Entropy_mat"],  
    occupation=new_data["Occupation_mat"],  
    int_dndt=new_data["intDNDT_mat"],  
    gs=new_data["Gammas"],  
)
```

3.1 Notes on NRG calculations

First let's look at the NRG data as provided by Yaakov.

A couple of notes about the NRG data. - All energies are defined in units of bandwidth (where bandwidth $\equiv E_F = 8.5$ meV for a 2DEG with electron density $2.42 \times 10^{15} \text{ m}^{-2}$ (10^{11} cm^{-2})). - For $T \gg T_K$ it is only the ratio Γ/T that is important, but for low T (or high Γ) the ratio T/T_K becomes important, and T_K is not a simple function of Γ .

The data is in two files, `NRGResultsNew.mat` and `NRGResultsNewWide.mat`. The narrow data is best for thermally broadened data, but is not wide enough for gamma broadened data, so the gamma broadened data is contained in the wider calculations

In order to make it easier to use, I combine both datasets into one taking the best of both, and making sure they have the same data shape. The mismatch between the size of the narrow arrays and wide arrays is filled with `np.nan` in the narrow arrays. I use a class for this so that it is easier to see what data is available

```
[6]: data = NRGData.from_mat()  
     print(data.dndt.shape)
```

```
(40, 2001)
```

`data` now refers to an object which holds all the data in the `.mat` files. Including `[ens, ts, conductance, dndt, entropy, occupation, int_dndt, gs]`.

```
[7]: attrs = ["ens", "ts", "conductance", "dndt", "occupation", "gs"]  
     for attr in attrs:  
         arr = getattr(data, attr)  
         print(f"{attr}.shape = {arr.shape}")
```

```
ens.shape = (40, 2001)  
ts.shape = (40,)  
conductance.shape = (40, 2001)  
dndt.shape = (40, 2001)
```

Appendix A. NRG data and fitting

```
occupation.shape = (40, 2001)
gs.shape = (40,)
```

3.2 Plotting NRG data as is

The arrays `ts` and `gs` correspond to the whole 1D arrays of data, and so only have the `y` shape

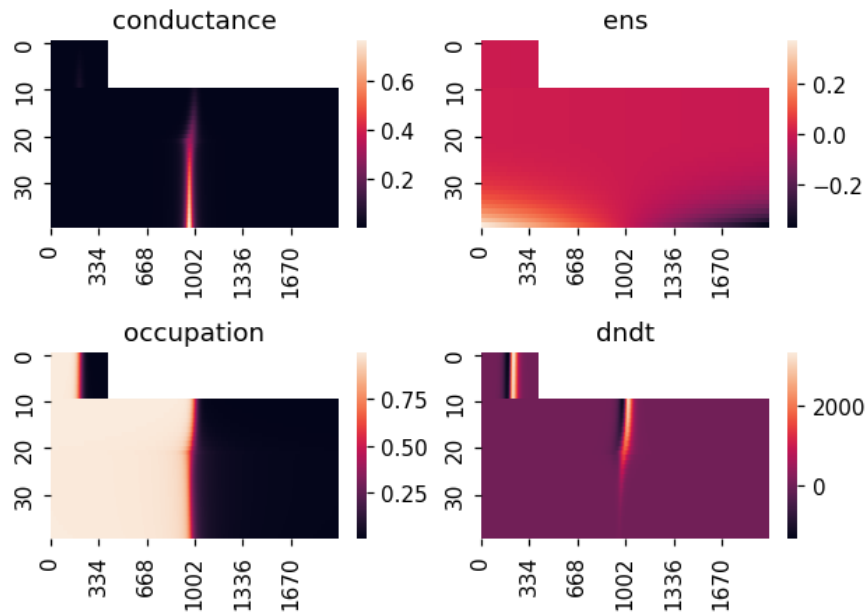
Now let's look at the data

```
[8]: attrs_2d = list(set(attrs) - {"ts", "gs"})

fig, axs = plt.subplots(2, 2, figsize=(FS, FS * 0.7))
axs = axs.flatten()

for attr, ax in zip(attrs_2d, axs):
    ax: plt.Axes
    sns.heatmap(ax=ax, data=getattr(data, attr))
    ax.set_title(f"{attr}")
    ax.set_xticks(ax.get_xticks()[::2])
    ax.set_yticks(ax.get_yticks()[::2])

fig.tight_layout()
```



Appendix A. NRG data and fitting

The mismatch in data shape can be seen here, where the rows 0-9 are from the narrow dataset and are filled with `np.nan` to match the data shape of the wider data

Note that for the new NRG data, entropy and `int_dndt` have **NOT** been calculated directly as this is a very expensive operation. However, the `dndt` data is sufficient to obtain the entropy changes given that entropy ends at $\ln(2)$ on the occupied side over the full calculated range.

The `ens` array is the x-axis (effectively sweep gate) data for all of the other datasets

For example, if we use the `ens` to plot some narrow and wide data we get:

```
[9]: rows = [8, 9, 10, 11] # rows around the change from narrow to wide
      datasets

fig, axs = plt.subplots(2, 2, figsize=(FS, FS * 0.7))
axs = axs.flatten()

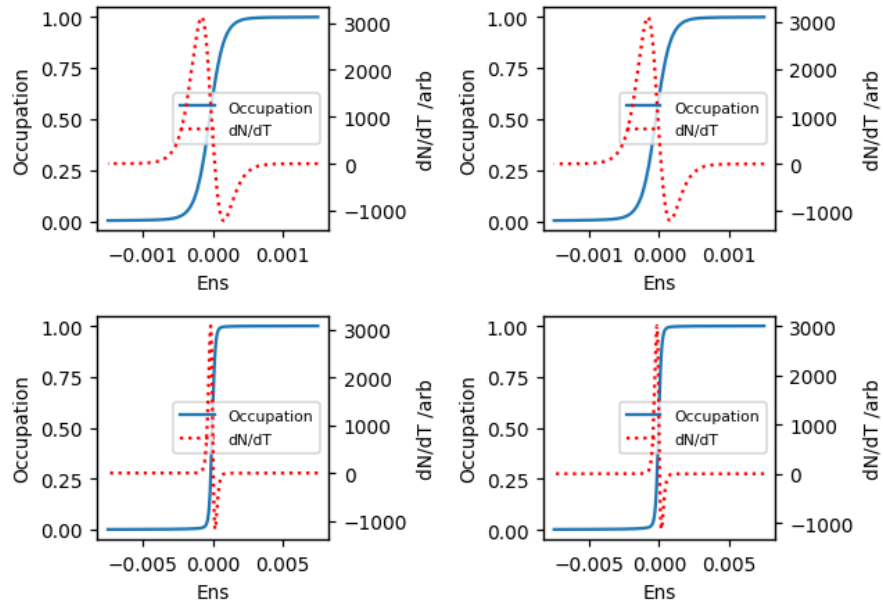
for r, ax in zip(rows, axs):
    x = data.ens[r]
    occ_data = data.occupation[r]
    dndt_data = data.dndt[r]

    ax.plot(x, occ_data, label="Occupation")
    ax.set_xlabel("Ens")
    ax.set_ylabel("Occupation")
    ax.plot([], [], "r:", label="dN/dT")
    ax.legend(loc="center right", fontsize=8)
    decrease_fontsize(ax, 1)

    ax2 = ax.twinx()
    ax2.plot(x, dndt_data, "r:")
    ax2.set_ylabel("dN/dT /arb")
    ax2.tick_params(axis="both")
    decrease_fontsize(ax2, 1)

fig.tight_layout()
```

Appendix A. NRG data and fitting



Note that the dndt data is scaled such that integrating (taking into account the ens spacing) results in close to, but not exactly the expected $\ln(2)$ total entropy change (see below).

```
[10]: rows = [8, 11, 23, 39]

fig, axs = plt.subplots(2, 2, figsize=(FS, FS * 0.7))
fig.suptitle(f"Demonstrating dN/dT scaling s.t. integrated results in max_{\Delta} \int_{-\Delta}^{\Delta} dN/dT = 1")
axs = axs.flatten()

for r, ax in zip(rows, axs):
    x = data.ens[r]
    occ_data = data.occupation[r]
    dndt_data = data.dndt[r]
    int_data = np.nancumsum(dndt_data) * np.nanmean(np.diff(x))
    int_data = int_data - np.nanmin(int_data)

    ax.plot(x, occ_data, label="Occupation")
    ax.set_xlabel("Ens")
    ax.set_ylabel("Occupation")
    ax.plot([], [], "r:", label="Integrated dN/dT")
```

Appendix A. NRG data and fitting

```

ticks = ax.get_xticks()
ax.set_xticks(ticks[1 if len(ticks) % 4 - 1 else 0 :: 2])
ax.legend(loc="lower right", fontsize=9)
decrease_fontsize(ax, 1)

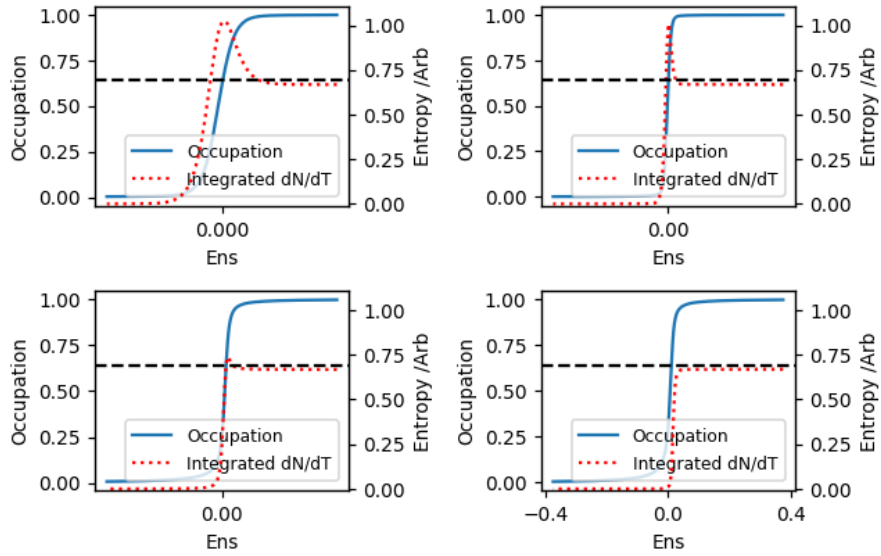
ax2 = ax.twinx()
ax2.plot(x, int_data, "r:")
ax2.set_ylabel("Entropy /Arb")
ax2.set_ylim(-0.01, np.log(3) + 0.01)
decrease_fontsize(ax2, 1)

ax2.axhline(np.log(2), color="k", linestyle="--")

fig.tight_layout()

```

Demonstrating dN/dT scaling s.t. integrated results in $\max == 1$



Note that the integrated entropy always ends close to but not quite $\ln(2)$. I believe this is just an artifact from calculation, they *should* all integrate to $\ln(2)$.

3.3 Plotting combined NRG datasets

We can plot the data using the ens and T/G ratios to see what the full space of calculated data really looks like

```
[11]: X = data.ens # same shape as data2d
      Y = data.ts / data.gs # Only 1D

      X1, X2 = X[0:10], X[10:] # Narrow, Wide
      X1 = X1[:, :401]

      # Note: we want a meshgrid denoting corner points of pixels instead of
      # centers
      XXs = []
      for X in X1, X2:
          x_stepsizes = np.array([np.mean(np.diff(_x)) for _x in X])
          # All step sizes should be the same (i.e. mean(diff) == diff[0])

          X = X + (x_stepsizes / 2)[:, None] # Shift coords half a step to
          # right
          XX = np.append(
              (X[:, 0] - x_stepsizes)[:, None], X, axis=1
          ) # Add a row of left side values starting half a step left
          XX = np.append(
              XX[0][None, :], XX, axis=0
          ) # Add an additional row to match with Y+1 shape, not ideal but ok
          # enough...
          # Not ideal because I should be extrapolating what the stepsize
          # would be
          XXs.append(XX)

      Y = np.concatenate(
          ([Y[0] - (Y[1] - Y[0]) / 2], (Y[0:-1] + Y[1:]) / 2, [Y[-1] + (Y[-1] -
          # Y[-2]) / 2])
      )
      # start-half first step, midpoints, end+half last step
      # Y spacing is not equal, so mostly we want the midpoints between values
      YYs = []
      for XX in XXs:
          YY = np.repeat(
              Y[:, None], XX.shape[-1], axis=1
          ) # Convert to same x-axis shape as XXs
          YYs.append(YY)
      YYs = [
```

Appendix A. NRG data and fitting

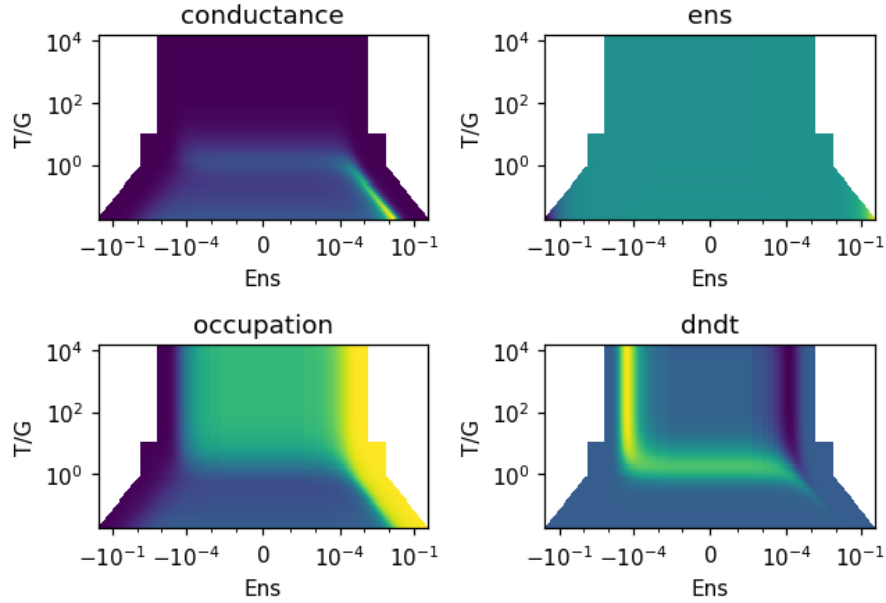
```
    YYs[0][:11],
    YYs[1][10:],
] # Convert to same y-axis shape as XXs (note both use same middle_
↳ coord (YYs[10]))

fig, axs = plt.subplots(2, 2, figsize=(FS, FS * 0.7))
axs = axs.flatten()

for attr, ax in zip(attrs_2d, axs):
    data_ = getattr(data, attr)
    Zs = data_[0:10, :401], data_[10:] # Only use Z part of data which_
↳ matches XX

    for XX, YY, Z in zip(XXs, YYs, Zs):
        ax.pcolormesh(XX, YY, Z, vmin=np.nanmin(data_), vmax=np.
↳ nanmax(data_))
        ax.set_title(f"{attr}")
        ax.set_xlabel("Ens")
        ax.set_ylabel("T/G")
        ax.set_yscale("log")
        ax.set_xscale("symlog", lincthresh=0.000001)
        xticks = ax.get_xticks()
        ax.set_xticks(xticks[1::3])
fig.tight_layout()
```

Appendix A. NRG data and fitting



The graphs above are plotting with a **log** y-scale and **symlog** (symmetric log) x-scale

The key graphs here are the **dndt** and **occupation**, as these are the data we compare to. **ens** highlights the symlog x-scale since the colorscale is just that of the x-values

4 Fitting to NRG

4.1 Parameters for Fitting

- **mid**: Position of $N=0.5$ occupation (only roughly $N=0.5$ for NRG - to get a more accurate center look at $N=0.5$ of occupation data)
- **theta**: Thermal broadening
- **g**: Gamma broadening

Specific to dndt

- **amp**: Scaling of dndt calculations

Specific to i_sense

- **amp**: Charge step size
- **const**: Average Charge Sensor current

Appendix A. NRG data and fitting

- **lin**: Cross capacitance of gate on Charge Sensor
- **occ_lin**: Change in **lin** as a fn of occupation (This is not often used)

4.2 Making NRG functions that behave like analytical functions

In order to use this data for fitting routines, we require a function which can take **any** value of all fitting parameters (Gamma, Theta, En etc), so we need to interpolate between the nearest rows of data. And we might want to do this for any of the NRG datasets. From top down:

- One can get such a function from `NRG_func_generator(which='i_sense')` for a function for the specified data (e.g. `[i_sense, occupation, dndt]`)
 - i.e. This returns a function which takes all the usual fitting parameters - (`x`, `mid`, `g`, `theta`, `amp`, `lin`, `const`, `occ_lin`)
- It does so by wrapping `nrg_func(...)`; a function which takes all the regular parameters + which data is being requested
- That requests an interpolator from `_get_interpolator(...)` and then performs the interpolation with the values passed to return a value/array of answers
- `_get_interpolator(...)` takes the `theta/g` ratio, and name of data to figure out exactly which rows of data from which dataset needs to be interpolated.
 - To avoid having to rebuild the same interpolator over and over, this then calls a **cached** function `_cached_interpolator` which actually generates the interpolator. Note: `_get_interpolator(...)` cannot be cached as the call to it could have **any** value of `theta/g` even if they end up returning the same interpolator
- The `_cached_interpolator(...)` is called with an index and data name, so this has well-defined call arguments which can be cached so future calls for the same interpolator don't have to be calculated again.
 - It takes the two consecutive rows of data that will be interpolated between
 - Does a 1D interpolation of the wider of the two rows of data to match the `ens` axis of the narrower data (wider/narrower in `ens`)
 - Then creates a 2D interpolator between the two rows of data
 - Converts the 2D interpolator into a function which takes the usual arguments (minus `[g, theta]`) and additionally:
 - * Adds an option for `i_sense` data by taking into account `[mid, amp, lin, const, occ_lin]`
 - * Scales `dndt` data with `amp` to help with arbitrary scaling of `dndt` calculations
 - Returns the function which takes the usual arguments

```
[12]: from typing import Union, Callable, Tuple
      from scipy.interpolate import interp1d, RectBivariateSpline
      from dat_analysis.core_util import get_data_index

      def NRG_func_generator(which="i_sense") -> Callable[... , Union[float, np.
        ndarray]]:
```

Appendix A. NRG data and fitting

```
"""
    Wraps the nrg_func in a way that can be used by lmfit. If not using
    lmfit, then just call nrg_func directly

    Args:
        which (): Which data to make a function for (i.e. 'i_sense',
        'occupation', 'dndt', etc)

    Returns:
        nrg_func for named data
    """
from functools import wraps

@wraps(nrg_func)
def wrapper(*args, **kwargs):
    return nrg_func(*args, **kwargs, data_name=which)

return wrapper

def nrg_func(
    x,
    mid,
    g,
    theta,
    amp: float = 1,
    lin: float = 0,
    const: float = 0,
    occ_lin: float = 0,
    data_name="i_sense",
) -> Union[float, np.ndarray]:
    """
        Returns data interpolated from NRG results. I.e. acts like an
        analytical function for fitting etc.

        Note: Does not require amp, lin, const, occ_lin for anything other
        than 'i_sense' fitting (which just adds terms to
        occupation)
        Args:
            data_name (): Which NRG data to return (i.e. occupation, dndt,
            i_sense)

        Returns:
```

Appendix A. NRG data and fitting

```
    """
    interper = _get_interpolator(t_over_gamma=theta / g,
data_name=data_name)
    return interper(x, mid, g, theta, amp=amp, lin=lin, const=const,
occ_lin=occ_lin)

def get_nrg_data(data_name: str):
    """Returns just the named data array from NRG data"""
    nrg = NRGData.from_mat()
    if data_name == "i_sense":
        z = 1 - nrg.occupation
    elif data_name == "ts":
        z = nrg.ts
    elif data_name == "gs":
        z = nrg.gs
    elif data_name == "occupation":
        z = nrg.occupation
    elif data_name == "dndt":
        z = nrg.dndt
    elif data_name == "conductance":
        z = nrg.conductance
    elif data_name == "ens":
        z = nrg.ens
    else:
        raise NotImplementedError(f"{data_name} not implemented")
    return z

def scale_x(x, mid, g, theta, inverse=False):
    """
    To rescale sweepgate data to match the ens of NRG (with varying
theta).

    Note: The -g*(...) - theta*(...) is just to make the center roughly
near OCC = 0.5 (which is helpful for fitting
only around the transition)

    x_scaled ~ (x - mid) * nrg_theta / theta

    Args:
        inverse (): set True to reverse the scaling

    Returns:
```

Appendix A. NRG data and fitting

```
"""
if not inverse:
    x_shifted = (
        x - mid - g * (-2.2) - theta * (-1.5)
    ) # Just choosing values which make 0.5 occ be near 0
    x_scaled = x_shifted * 0.0001 / theta # 0.0001 == nrg_T
    return x_scaled
else:
    x_scaled = x / 0.0001 * theta # 0.0001 == nrg_T
    x_shifted = x_scaled + mid + g * (-2.2) + theta * (-1.5)
    return x_shifted

def _get_interpolator(t_over_gamma: float, data_name: str = "i_sense") -> Callable:
    """
    Generates a function which acts like a 2D interpolator between the
    closest t_over_gamma values of NRG data.

    Returns:
        Effective interpolator function which takes same args as nrg_func
        i.e. (x, mid, g, theta, amp=1, lin=0, const=0, occ_lin=0) where
        the optionals are only used for i_sense
    """
    ts, gs = [get_nrg_data(name) for name in ["ts", "gs"]]
    tgs = ts / gs
    # index = np.abs(tgs - t_over_gamma).argmin()
    index = get_data_index(tgs, t_over_gamma)
    index = (
        index if tgs[index] > t_over_gamma else index - 1
    ) # want the true value to be between interpolated rows
    if index < 0: # Asking for data outside of calculation range
        index = 0
    elif (
        index > len(tgs) - 2
    ): # -2 because cached interpolator is going to look at next row as well
        index = len(tgs) - 2
    return _cached_interpolator(lower_index=index, data_name=data_name)

@lru_cache(
    maxsize=100

```

Appendix A. NRG data and fitting

```
) # Shouldn't ever be more than XX rows of NRG data (XX == size of data
↳ in .mat files)
def _cached_interpolator(lower_index: int, data_name: str) -> Callable:
    """
    Actually generates the scipy 2D interpolator for NRG data.
    This can be used for any future requests of this interpolator
    so this should be cached.

    Args:
        lower_index (): The lower index of NRG data to use for
↳ interpolation (will always interpolate between this and
        lower_index + 1)
        data_name (): Which NRG data to make an interpolator for

    Returns:
        2D interpolator function which takes x as an energy and y as a
↳ gamma/theta ratio.
    """

    def strip_x_nans(x: np.array, z: np.array) -> Tuple[np.ndarray, np.
↳ ndarray]:
        """Strip off NaNs that are in x array (and corresponding data)"""
        return x[np.where(~np.isnan(x))], z[np.where(~np.isnan(x))]

    ts, gs, ens, data = [
        get_nrg_data(name)[lower_index : lower_index + 2]
        for name in ["ts", "gs", "ens", data_name]
    ]
    tgs = ts / gs

    narrower_ens, narrower_data = ens[0], data[0] # Just the
    wider_ens, wider_data = ens[1], data[1]

    narrower_ens, narrower_data = strip_x_nans(narrower_ens,
↳ narrower_data)
    wider_ens, wider_data = strip_x_nans(wider_ens, wider_data)

    single_interper = interp1d(
        x=wider_ens, y=wider_data, bounds_error=False,
↳ fill_value="extrapolate"
    ) # values are saturated near edge of NRG data,
    # so effectively constants for extrapolation

    interpolated_wider_data = single_interper(
```

Appendix A. NRG data and fitting

```
x=narrower_ens
) # i.e. mapping wider data to narrower ens

# Note: Just returns edge value if outside interp range
# flips are because x and y must be strictly increasing
interper = RectBivariateSpline(
    x=np.flip(narrower_ens),
    y=np.flip(np.log10(tgs)),
    z=np.flip(np.array([narrower_data, interpolated_wider_data]).T,
axis=(0, 1)),
    kx=1,
    ky=1,
)
# Note: the interpolator does not use the parts of the wider data
that extend beyond the narrower data

interp_func = _interper_to_nrg_func(interper, data_name)
return interp_func

def _interper_to_nrg_func(interper, data_name: str):
    """Makes a function which takes normal fitting arguments and returns
    that function"""

    def func(x, mid, g, theta, amp=1, lin=0, const=0, occ_lin=0):
        x_scaled = scale_x(x, mid, g, theta)
        interped = interper(x_scaled, np.log10(theta / g)).flatten()
        if data_name == "i_sense":
            interped = (
                amp * (1 + occ_lin * (x - mid)) * interped
                + lin * (x - mid)
                + const
                - amp / 2
            )
            # Note: (occ_lin*x)*Occupation is a linear term which
            changes with occupation,
            # not a linear term which changes with x
        elif data_name == "dndt":
            interped *= amp
        elif data_name == "conductance":
            interped = amp * interped + const
        return interped

    return func
```

Appendix A. NRG data and fitting

And a function for getting the x value that corresponds to a given occupation N .

```
[13]: def get_x_at_occupation(N, mid=0, theta=None, g=None) -> float:
      """
      Get x value at occupation N
      (Note that the NRG data has its own energy scale where 0 is only
      close to N=0.5)

      Args:
          mid (): Middle of transition based on fitting (this value will
          not be exactly N=0.5)
          theta (): Theta (thermal broadening)
          g (): Gamma (tunnel broadening)
      """
      # Make a high density x-array that will include N=0.5
      x = np.linspace(mid - 1000, mid + 1000, 100000)
      occ = nrg_func(x=x, mid=mid, g=g, theta=theta, data_name="occupation")
      # Get index where occ closest to N
      idx = np.abs(occ - N).argmin()
      # Return the x of that index
      return x[idx]
```

4.3 Demonstration of NRG functions

A couple of demonstrations of the use of these functions to generate data, although usually they will only be used for fitting

```
[14]: theta = 1
      gamma = 0.1
      amp = 1
      mid = 0
      const = 5
      lin = 0.005
      occ_lin = 0

      x = np.linspace(-20, 20, 100)

      data_names = ["dndt", "occupation", "i_sense"]

      fig, axs = plt.subplots(1, 3, figsize=(FS, FS * 0.4))
      axs = axs.flatten()

      for name, ax in zip(data_names, axs):
          func = NRG_func_generator(which=name)
```

Appendix A. NRG data and fitting

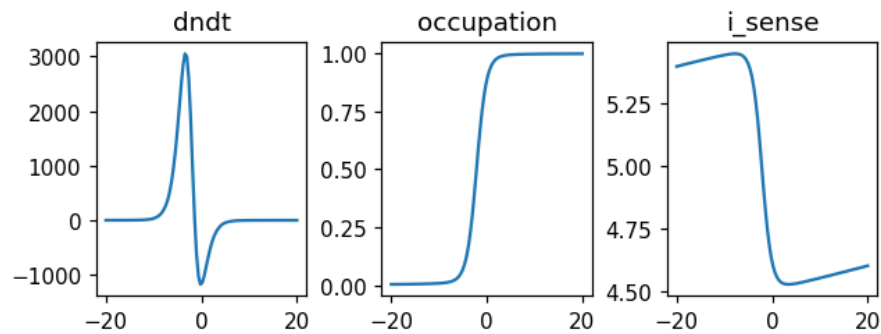
```

data = func(
    x=x,
    mid=mid,
    amp=amp,
    const=const,
    lin=lin,
    occ_lin=occ_lin,
    g=gamma,
    theta=theta,
)
# Note that only x, mid, gamma, theta are used for all three datas,
# they are ignored for the wrong data types
ax.plot(x, data)
ax.set_title(f"{name}")

fig.tight_layout()
print(
    f"Notice that the true x value of N=0.5 is actually
    x={get_x_at_occupation(N=0.5, mid=mid, theta=theta, g=gamma):.4f}, not
    0"
)

```

Notice that the true x value of $N=0.5$ is actually $x=-2.1500$, not 0



Although the center of transition ($N = 0.5$) is close to but not quite $x = 0$. The NRG data as provided has an absolute zero given by the ens, however, this does not align with $N = 0.5$ (which makes sense since entropy should shift the occupation with temperature etc). For comparison to experimental data, it is helpful to have the center of transition be close to $x = 0$ for ease of fitting (it is difficult to estimate a center value otherwise). This is achieved

Appendix A. NRG data and fitting

by shifting the x-axis of NRG data **AFTER** interpolation with the line:

$$x_{\text{shifted}} = x - x_0 - \Gamma \times (-2.2) - \Theta \times (-1.5)$$

where the factors -2.2 and -1.5 were found through trial and error to result in the $N = 0.5$ being close to $x = 0$

And then scaling to account for thermal broadening (which is OK to do because the calculations are dependent on Γ/T ratio only) using:

$$x_{\text{scaled}} = x_{\text{shifted}} \times \frac{0.0001}{\Theta}$$

where 0.0001 is the Theta value used in the NRG calculations

We can also plot 2D data using the generated function

```
[15]: def xy_to_meshgrid(x, y):
    """returns a meshgrid that makes sense for pcolorgrid
    given z data that should be centered at (x,y) pairs"""
    nx = len(x)
    ny = len(y)

    dx = (x[-1] - x[0]) / float(nx - 1)
    dy = (y[-1] - y[0]) / float(ny - 1)

    # shift x and y back by half a step
    x = x - dx / 2.0
    y = y - dy / 2.0

    xn = x[-1] + dx
    yn = y[-1] + dy

    return np.meshgrid(np.append(x, xn), np.append(y, yn))

x = np.linspace(-20, 20, 100)
g_over_t = np.linspace(0.1, 10, 100)
theta = 1

gamma = g_over_t * theta

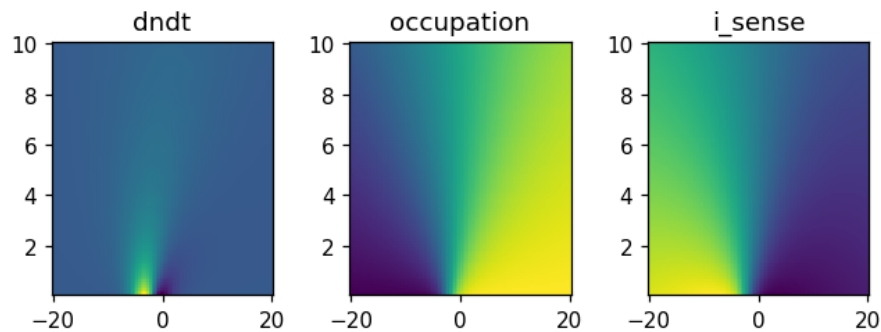
fig, axs = plt.subplots(1, 3, figsize=(FS, FS * 0.4))
axs = axs.flatten()

for name, ax in zip(data_names, axs):
    func = NRG_func_generator(which=name)
```

Appendix A. NRG data and fitting

```
data = np.array(
    [
        func(
            x=x,
            mid=mid,
            amp=amp,
            const=const,
            lin=lin,
            occ_lin=occ_lin,
            g=g,
            theta=theta,
        )
        for g in gamma
    ]
)
xx, yy = xy_to_meshgrid(x, g_over_t)
ax.pcolormesh(xx, yy, data)
ax.set_title(f"{name}")

fig.tight_layout()
```



4.4 Fitting with NRG functions

For fitting to data, I use the `lmfit` package.

As an example, I will generate some fake `i_sense` data using the function demonstrated above

```
[16]: theta = 1
      gamma = 0.005 # Very weakly coupled to start with
```

Appendix A. NRG data and fitting

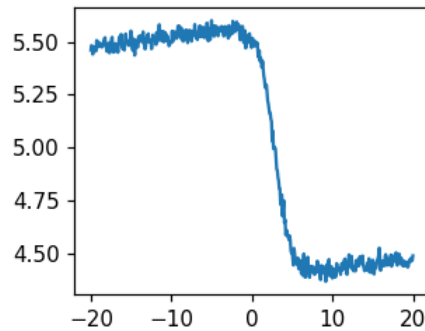
```
amp = 1.2
mid = 5
const = 5
lin = 0.005
occ_lin = 0

noise_fraction = 0.02

x = np.linspace(-20, 20, 500)

i_sense_func = NRG_func_generator(which="i_sense")
fake_data = i_sense_func(
    x=x, mid=mid, const=const, amp=amp, lin=lin, g=gamma, theta=theta,
    occ_lin=occ_lin
)
fake_data += np.random.normal(0, amp * noise_fraction, x.shape[0])

fig, ax = plt.subplots(figsize=(FS * 0.5, FS * 0.4))
ax.plot(x, fake_data)
fig.tight_layout()
```



Using the data above to demonstrate fitting to NRG

We'll need to make some initial guesses for fitting parameters. Typically, a function like the one below does a good enough job for starting parameters.

```
[17]: def guess_isense_params(
    x, data, g: float, g_vary: bool, theta: float, theta_vary: bool
) -> lm.Parameters:
    params = lm.Parameters()
```

Appendix A. NRG data and fitting

```
params.add_many(  
    #           name, value, vary, min, max  
    # Guess middle of dataset  
    lm.Parameter("mid", np.nanmean(x), True, -100, 100),  
    # Guess similar to amplitude of total data  
    lm.Parameter("amp", np.nanmax(data) - np.nanmin(data), True, 0),  
    # Generally requires quite strict limits  
    lm.Parameter("lin", 0, True, 0, 0.1),  
    # Roughly in middle of data  
    lm.Parameter("const", np.nanmean(data), True),  
    # Usually 5 works quite well, could do something more fancy if  
    ↪needed  
    lm.Parameter("theta", theta, theta_vary, 0, 20),  
    # Holding fixed near zero because fitting weakly coupled data  
    lm.Parameter("g", g, g_vary, theta / 1000, theta * 50),  
    # Usually not needed  
    lm.Parameter("occ_lin", 0, False),  
)  
return params
```

4.4.1 Fitting weakly coupled data

For fitting weakly coupled data (like the data above), the `g` value should be set small and forced not to vary, and `theta` should be allowed to vary.

```
[18]: params = guess_isense_params(x, data, g=0.001, g_vary=False, theta=5, ↪  
    ↪theta_vary=True)
```

Note that the parameter `g` cannot be set exactly to zero and is **NOT** allowed to vary here (since we are trying to fit weakly coupled data). In fact, even with `g` set 5x lower than the generated data, we should get a good fit since we are in the weakly coupled regime. Also not allowing `occ_lin` to vary just because that is generally not needed

```
[19]: func = NRG_func_generator(which="i_sense")  
  
model = lm.model.Model(func)  
fit = model.fit(fake_data, x=x, params=params, method="powell", ↪  
    ↪nan_policy="omit")
```

Note: The fitting method has been specified as `powell` rather than the default `leastsq`.

I experimented with many other fitting modes and found `powell` to be most reliable. I believe this is because of the discontinuous gradient of the interpolated data (i.e. corners at each calculated value)

Appendix A. NRG data and fitting

```
[20]: print("Comparison of Expected vs Fit values\nName\t\tExpected\t\tFit")
for expected, name in zip(
    [mid, amp, const, lin, theta, gamma, occ_lin],
    ["mid", "amp", "const", "lin", "theta", "g", "occ_lin"],
):
    par = fit.params.get(name)
    print(f"{name:10}\t\t{expected:.1f}\t\t{par.value:.2f}\u00b1{par.
stderr:.2f}")
```

Comparison of Expected vs Fit values

Name	Expected	Fit
mid	5.0	4.99±0.04
amp	1.2	1.20±0.01
const	5.0	5.00±0.00
lin	0.0	0.00±0.00
theta	1.0	1.00±0.02
g	0.0	0.01±0.00
occ_lin	0.0	0.00±0.00

Or we can look at the full fit report

```
[21]: print(fit.fit_report())
```

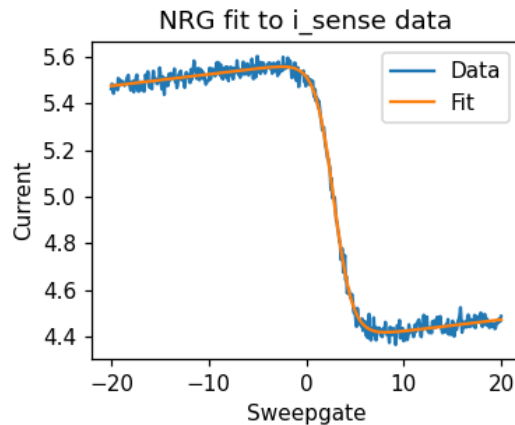
```
[[Model]]
  Model(nrg_func)
[[Fit Statistics]]
  # fitting method   = Powell
  # function evals   = 812
  # data points      = 500
  # variables        = 5
  chi-square         = 0.27294246
  reduced chi-square = 5.5140e-04
  Akaike info crit   = -3746.55119
  Bayesian info crit = -3725.47815
  R-squared           = 0.99792494
[[Variables]]
  mid:      4.98810340 +/- 0.04252290 (0.85%) (init = -9.094947e-16)
  amp:      1.19941503 +/- 0.00703026 (0.59%) (init = 0.9196366)
  lin:      0.00498214 +/- 2.6391e-04 (5.30%) (init = 0)
  const:    4.99934266 +/- 0.00152794 (0.03%) (init = 4.930602)
  theta:    0.99835231 +/- 0.01923735 (1.93%) (init = 5)
  g:        0.005 (fixed)
  occ_lin:  0 (fixed)
[[Correlations]] (unreported correlations are < 0.100)
  C(mid, theta) = 0.940
  C(amp, lin)   = 0.938
```

Appendix A. NRG data and fitting

```
C(amp, theta) = 0.697
C(lin, const) = 0.674
C(mid, amp) = 0.640
C(lin, theta) = 0.629
C(amp, const) = 0.603
C(mid, lin) = 0.564
C(const, theta) = 0.472
C(mid, const) = 0.345
```

And now lets plot the fit on the data

```
[22]: fig, ax = plt.subplots(figsize=(FS * 0.6, FS * 0.5))
ax.plot(x, fake_data, label="Data")
ax.plot(x, fit.eval(x=x), label="Fit")
ax.set_title(f"NRG fit to i_sense data")
ax.set_xlabel("Sweepgate")
ax.set_ylabel("Current")
ax.legend()
fig.tight_layout()
```



Because both g and θ are so strongly correlated, for fitting strongly coupled data ($g > \theta$), it is necessary to hold θ fixed at the expected value.

4.4.2 Fitting strongly coupled data

For strongly coupled data, `theta` should be set to its expected value and set to NOT vary, while `g` can be set to vary (within limits of $0.001 < T < 50T$).

Appendix A. NRG data and fitting

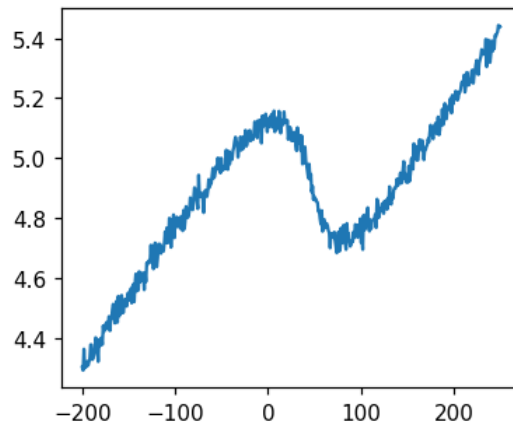
```
[23]: theta = 1
gamma = 15 # Made Gamma >> T
amp = 1.2
mid = 50
const = 5
lin = 0.005
occ_lin = 0

noise_fraction = 0.02

x = np.linspace(-200, 250, 500) # Much wider x-axis

i_sense_func = NRG_func_generator(which="i_sense")
fake_data = i_sense_func(
    x=x, mid=mid, const=const, amp=amp, lin=lin, g=gamma, theta=theta,
    occ_lin=occ_lin
)
fake_data += np.random.normal(0, amp * noise_fraction, x.shape[0])

fig, ax = plt.subplots(figsize=(FS * 0.6, FS * 0.5))
ax.plot(x, fake_data)
fig.tight_layout()
```



Where the max/min points of the data are not near the transition sometimes causes issues with guessing `amp` as the `max - min`, but probably it is OK with this.

This time, we will allow `g` to vary while fitting, but hold `theta` fixed at the expected value.

Appendix A. NRG data and fitting

And we'll use the same model for the fitting

```
[24]: # Generate new params
params = guess_isense_params(x, data, g=5, g_vary=True, theta=theta,
                             theta_vary=False)

# Using same model as previously
fit = model.fit(fake_data, x=x, params=params, method="powell",
               nan_policy="omit")

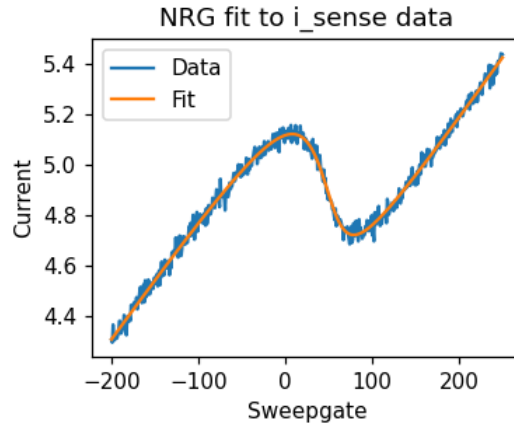
[25]: print("Comparison of Expected vs Fit values\nName\t\tExpected\t\tFit")
for expected, name in zip(
    [mid, amp, const, lin, theta, gamma, occ_lin],
    ["mid", "amp", "const", "lin", "theta", "g", "occ_lin"],
):
    par = fit.params.get(name)
    print(f"{name:10}\t\t\t{expected:5.1f}\t\t\t{par.value:.2f}\u00b1{par.
          stderr:.2f}")

fig, ax = plt.subplots(figsize=(FS * 0.6, FS * 0.5))
ax.plot(x, fake_data, label="Data")
ax.plot(x, fit.eval(x=x), label="Fit")
ax.set_title(f"NRG fit to i_sense data")
ax.set_xlabel("Sweepgate")
ax.set_ylabel("Current")
ax.legend()
fig.tight_layout()
```

Comparison of Expected vs Fit values

Name	Expected	Fit
mid	50.0	49.76±0.31
amp	1.2	1.16±0.02
const	5.0	5.00±0.00
lin	0.0	0.00±0.00
theta	1.0	1.00±0.00
g	15.0	14.13±0.36
occ_lin	0.0	0.00±0.00

Appendix A. NRG data and fitting



As expected, a good fit to `fake_data`

Now let's fit the data. We'll change the initial params first so that we aren't cheating too much

Again we see a good fit. Note that there are several fitting parameters shown above that are not used and are just held fixed.

5 Plotting vs Occupation

Instead of plotting an energy/sweepgate values on the x-axis, let's plot against occupation instead. This will be useful for comparing measurements at varying G/T ratios

This is achieved by using the same parameters (specifically the `g`, `theta`, and `mid`) values to generate the expected Occupation data. We'll just skip to using the useful functions to do this.

```
[26]: mid = 30
      amp = 1
      theta = 20
      g = 0.001
      lin = 0.001
      const = 5
      occ_lin = 0

      x = np.linspace(-300, 300, 1000)
      occ_x = nrg_func(x, mid, g, theta, data_name="occupation")
```

Appendix A. NRG data and fitting

```

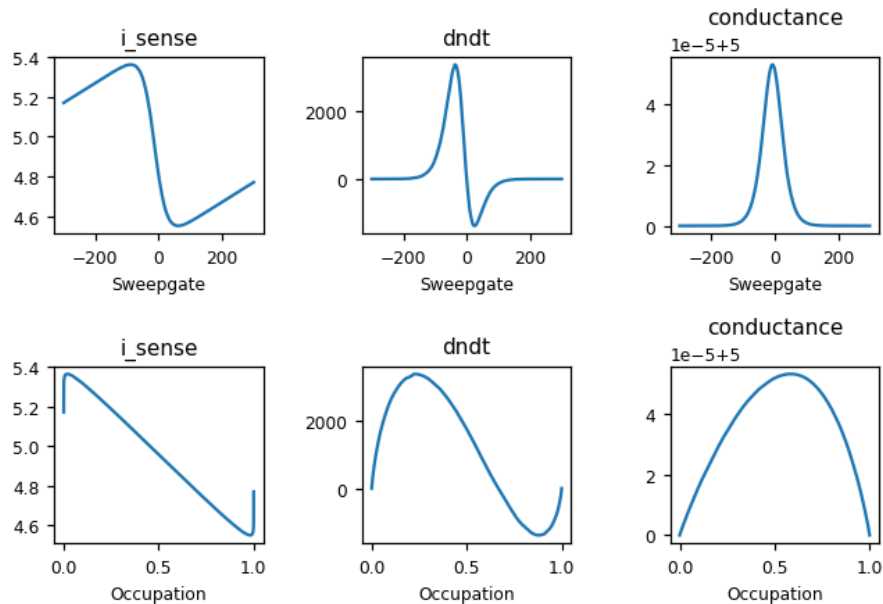
data_names = ["i_sense", "dndt", "conductance"]
fig, axs = plt.subplots(2, 3, figsize=(FS, FS * 0.7))

for name, ax in zip(data_names, axs[0, :]):
    # data = nrg_helper.data_from_params(x=x, which_data=name,
    ↪which_x="sweepgate")
    data = nrg_func(x, mid, g, theta, lin=lin, const=const,
    ↪data_name=name)
    ax.plot(x, data)
    ax.set_title(name)
    ax.set_xlabel("Sweepgate")
    decrease_fontsize(ax, 2)

for name, ax in zip(data_names, axs[1, :]):
    data = nrg_func(x, mid, g, theta, lin=lin, const=const,
    ↪data_name=name)
    ax.plot(occ_x, data)
    ax.set_title(name)
    ax.set_xlabel("Occupation")
    decrease_fontsize(ax, 2)

fig.tight_layout()

```



Appendix A. NRG data and fitting

As expected, the `i_sense` data is linear when plotted against Occupation (excluding the edges). The non-zero linear term results in vertical lines at either end (i.e. changing current with no change of occupation).

Plotting dN/dT this way makes it much easier to compare dN/dT for varying Γ/T . Same goes for conductance data

e.g.

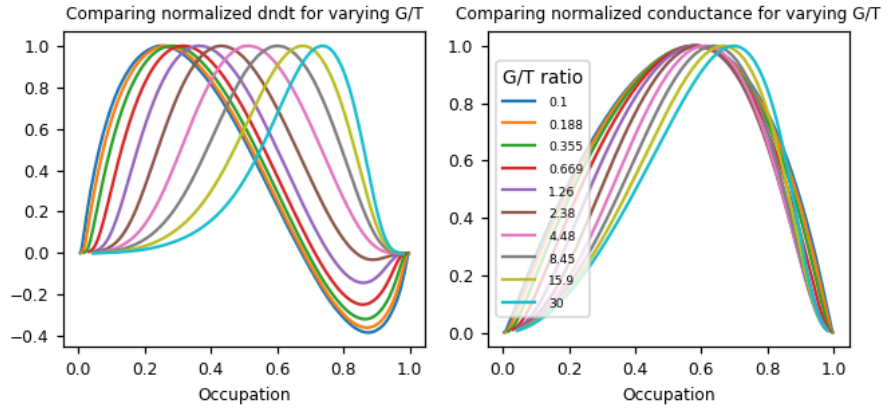
```
[27]: g_over_ts = np.logspace(np.log10(0.1), np.log10(30), 10)
mid = 0
theta = 10
# g -- defined in loop based on G/T ratios
# print("Ratios to plot: ", [f"{gt:.3g}" for gt in g_over_ts])

fig, axs = plt.subplots(1, 2, figsize=(FS, FS * 0.5))
axs = axs.flatten()
for data_name, ax in zip(["dndt", "conductance"], axs):
    for gt in g_over_ts:
        g = gt * theta
        x = np.linspace(
            -max([theta, gt * theta]) * 15, max([theta, gt * theta]) * 15, 300
        ) # Wider x needed for wider data
        occ_x = nrg_func(x, mid, g, theta, data_name="occupation")
        data = nrg_func(x, mid, g, theta, data_name=data_name)
        data = data / np.nanmax(data)
        ax.plot(occ_x, data, label=f"{gt:.3g}")
        # ax.plot(x, data, label=f"{gt:.3g}")

    if data_name == "conductance":
        leg = ax.legend(title="G/T ratio", loc="center left", fontsize=8)
        leg.get_title().set_fontsize(9)
    ax.set_title(f"Comparing normalized {data_name} for varying G/T",
        fontsize=10)
    ax.set_xlabel("Occupation")
    decrease_fontsize(ax, 2)
    # ax.set_ylabel("Normalized Delta Current")

fig.tight_layout()
```

Appendix A. NRG data and fitting



Appendix B

Measurement setup

The cryostats used for all measurements presented in this thesis were dilution refrigerators of the “dry” type that utilize a closed loop pulse tube for the cooling of the 4 K (and higher T) plates (see Fig. B.1). This is in contrast to “wet” fridges that use liquid He and require regular top ups. Specifically, two Bluefors models were used: a BF-LD400 and BF-XLD400. The dry fridges enable long duration (many months of) measurements with relatively little maintenance; however, the pulse tube introduces mechanical vibrations into the system that can affect both base temperature and electrical measurement noise. The cryostats themselves are capable of cooling the mixing chamber plate down to $T_F \sim 7$ mK (and we assume that our heterostructure chips reach similarly low phonon temperatures). However, it is the temperature of the electrons in the 2DEG that is important for the measurements presented within this thesis, and they do not reach such low temperatures due to the presence of electrical noise that propagates down the measurement lines. In practice, we were able to achieve electron temperatures around $T_e \sim 25$ mK in our systems, although that was not our primary concern.

There are two main approaches to reducing the electrical noise that reaches the 2DEG: prevention and filtering. For prevention, it is necessary to understand where the noise come from in the first place. Although the precise sources of electrical noise are difficult to pin down, our experience seems to suggest that in addition to 60 Hz (and harmonics) noise that can typically be eliminated by identifying and removing any ground loops, a significant source (especially in our dry fridges) is triboelectric in nature. Over a wide range of relatively low frequencies ($\lesssim 5$ kHz), electrical noise increases with decreasing temperature of the system – an effect that we think is related to the difference in thermal expansion coefficients of the

Appendix B. Measurement setup

metals and insulators used in the wiring that increase the amount that the wires rub against the insulators when moved by vibrations. Unfortunately, because this only becomes apparent at very low temperatures, it is difficult to optimize the cryostat wiring because the behavior at room temperature does not correlate well with the behaviour at the low temperatures where the characteristics are most important. In the end, we found that although we could achieve better room temperature performance from the top of the fridge to the Still plate with our own wiring, the twisted pair phosphor-bronze wiring provided by Bluefors performed similarly or slightly better at very low temperature, and was less prone to thermal cycling issues. From there, we found that polyimide flat printed circuit (FPC) flexible cables performed well at low temperatures, and provide a convenient means of interfacing with PCBs or other FPCs via ZIF connectors that can be obtained without magnetic impurities (important for high and/or sweeping magnetic field measurements).

In terms of filtering, we primarily relied upon a 3-stage RC filter placed on the mixing chamber. Typically, the cutoff frequency (-3 dB) was around 50 kHz, however, in the most recent iterations, we switched to single stage RC filters with cutoff frequencies around 10 kHz or lower. Generally speaking, the low-pass filter should be designed to have as low a cutoff frequency as permitted by the measurements (either in terms of frequency or inline resistance). At the expense of re-usability, the RC filter can be designed with the specific device to be measured in mind, using higher Rs and Cs (and thus lower cutoff frequencies) for gates that will be held at constant potentials during individual measurements. The placement of the RC filter is also very important: it should be as close as possible to the device (ideally, toward the end of the cold finger) and should be clamped securely to ensure it is well thermalized with the mixing chamber. In fact, in Fig. 1.1a one can see that the heterostructure chip is glued (using PMMA) directly to a silicon wafer that is itself stuck to the coldfinger using silver paste. The silicon wafer has thin meandering nano-fabricated lines that act as a distributed RC filter immediately before the device – in addition to the RC filter that lies on the mixing chamber plate. After the RC filtering, it is important

Appendix B. Measurement setup

to keep any remaining wiring up to and including the device shielded by a conductor (typically copper) that is well thermalized with the MC plate to avoid microwave radiation from the relatively warm (~ 1 K) still shield entering the lines.

Because any optimization of cryostat wiring requires thermal cycling, and given that the thermal cycling process takes several days at best, it is a very time consuming process to carry out systematic tests. Instead, we attempted to find a middle ground – doing our best to improve noise and thermal characteristics of the systems between regular measurement cooldowns – without dedicating the enormous amount of time that would have been required to investigate each problem systematically. As a result, I have many thoughts and superstitions about what factors are important in determining optimal measurement conditions, but few concrete facts. For a more systematic analysis of cryostat wiring, I recommend Ref. [173], from which we utilize many of the same components. Ref. [174] also demonstrates exceptional cryostat wiring, where an electron temperature of only 6 mK was achieved.

Appendix B. Measurement setup



Figure B.1: Photo of the BF-XLD system showing the lower temperature plates and coldfinger. The gold plated copper plate that is in line with the bottom of the top outer vacuum can (OVC) is the 4 K plate. Below that, there is the Still plate, 0.1 K (not usually referenced), and finally, the mixing chamber (MC) plate. The 50 K plate is hidden from view by the top OVC. The coldfinger is the copper piece extending below the MC plate, designed such that a mounted sample is positioned in the center of the magnet (not shown) when the system is in operation.